ISAS - INTERNATIONAL SCHOOL FOR ADVANCED STUDIES

Quantum Theory of Non-Homogeneous Phases of Helium

Thesis submitted for the degree of Doctor Philosophiae

Condensed Matter Sector

Candidate:

Francesco Pederiva

Supervisors:

Prof. Stefano Fantoni
Prof. Luciano Reatto

October 1994

TRIESTE

SISSA - SCUOLA INTERNAZIONALE SUPERIORE DI STUDI AVANZATI
TRIESTE
Strada Costiera 11

Table of Contents

1 Introduction

The physics of Helium at low temperatures is one of the most interesting topics in condensed matter physics.[1] The rich phenomenology that has been experimentally evidenced in fifty years of investigations allows for touching with hand the peculiar features that characterize the systems in which quantum effects are prevalent on the classical physics[2]. The presence of two distinct isotopes, ^{4}He and ^{3}He with different statistical properties (the first is a spin 0 boson while the second is a spin 1/2 fermion) makes of Helium a relevant topic in the field of quantum many body physics.

From the theoretical point of view an ensemble of N He atoms is realistically described by a non relativistic hamiltonian of N elementary particles interacting via a two–body potential:

$$\hat{H} = \sum_{i=1}^{N} \frac{\hbar^2}{2m} \nabla_i^2 + \sum_{i=1}^{N} \sum_{i<j} v(r_{ij}). \tag{1.1}$$

The interatomic effective interaction v, is known with a remarkable precision, and is usually fitted by the so called *Aziz potential*[3]. Employing this potential and using the most sophisticated techniques of microscopic investigation it has been possible to reproduce most the experimental results in ^{4}He[4].

In ^{3}He the available many–body theories do not still allow to check the reliability of the model hamiltonian (1.1) with the same accuracy as in ^{4}He.

In the last few years much experimental effort has been devoted to the study of coexisting phases, interfaces[5, 6, 7, 8], mixtures[9], free surfaces[10], thin films[11, 12, 13]. Few microscopic calculations have been performed for inhomogeneous systems such as films[14, 15], droplets[16, 17], and liquid–vapor interface[18, 19, 20], mostly in the framework of variational theories. The most sophisticated simulation techniques, such as the Green Function Monte Carlo (GFMC) and the Diffusion Monte Carlo (DMC), that provided very good results in the study of the bulk[21], have been used to simulate helium droplets[22] with some success. Path Integral Monte Carlo (PIMC) technique has recently been used to describe a thin film of ^{4}He on a graphite substrate[23]. However, the major limitation of these methods is that they are very demanding strictly from a computational point of view, and the size of the systems that can realistically be simulated is rather small. On the other hand the Variational Monte Carlo (VMC)approach, allows for dealing with a much larger number of particles, necessary to obtain a reasonable representation of two coexisting phases and of the relative interface.

A remarkable improvement in the description of ^{4}He near the solid–fluid phase transition has been achieved by the introduction of the Shadow Wave Function (SWF)[24, 25]. Shadow Wave Function that is written in form of a convolution of function correlating the atoms and a set of auxiliary variables (the "shadows"), is employed as a trial wave function in the VMC and recently also in HyperNetted Chain (HNC)[26] calculations. One major property of SWF is the capability of describing a crystalline system without breaking explicitely the translational invariance of the wave function. In this thesis we extend the SWF formalism, introducing a new form of the wave function, the Local Density Shadow Wave Function (LD–SWF)[27, 28], that allows for the description of phase–coexistence and other inhomogeneous situations. By this wave function we performed the first simulation of spontaneous crystallization from a superdense liquid in a quantum system, confirming

the effective capability of LD–SWF to provide a solid phase as variational ground state whenever the density is increased enough[29].

We focused in this work on the solid–liquid coexistence and interface in ^{4}He, obtaining the first microscopic estimates of interesting quantities, such as the width of the solid–liquid interface and the interfacial energy. Such calculations, existing for classical systems[30, 31], were completely missing for quantum systems.

The importance of studying solid–liquid coexistence in ^{4}He is given by the fact that it represents a nearly ideal system in the study of surface properties, due in particular to the high purity that can be easily reached in the samples. This allows, for instance, the study of crystal growth in an intrinsic regime. Recent experimental works of the group of S. Balibar[8] and of O. A. Andreeva[6] on the roughening properties of the crystal surface of ^{4}He renewed the interest on this topic. Such experiments are based on the measure of the anisotropy of the surface stiffness, quantity connected to the roughening temperature, with respect to the orientation of the crystalline planes, in order to understand if for some orientation the solid surface is rough at any temperature. Connected to that is the study of stepped surfaces and of crystallization waves. Other important experiments are devoted to the study of thin films of ^{4}He deposited on different substrates[13, 12]. It is known that the first layers of helium are crystallized, and successively one starts to observes fluid layers. This situation may be described in a simulation with a large number of atoms by means of LD–SWF.

Another important extension of SWF, introduced in this thesis, has been done to describe ^{3}He[32]. The phenomenology in ^{3}He is reacher than in ^{4}He, due to the presence of spin (polarized states, spin ordering, magnetic properties). Preliminary results obtained extending SWF to ^{3}He are very encouraging. The upper bound for the energy per particle in the liquid phase at equilibrium density, shows that the quality of the results is similar

to that in ^{4}He. Moreover we obtained a stable crystal with the correct structure when increasing the density. This indicates the possibility to simulate also in ^{3}He the solid liquid coexistence, and eventually other inhomogeneous phases.

The plan of the work is the following. We start with describing briefly the state of the art in conventional variational theories. We introduce then the Shadow Wave Function (SWF) in its original formulation, and its extension to Local Density Shadow Wave Function (LD–SWF), developed in order to describe inhomogeneous systems such as liquid–solid coexistence. We will then present results on the spontaneous crystallization of a superdense liquid sample using such formalism, on the study of the solid–liquid coexistence and interface in ^{4}He Finally preliminary results on the extension of SWF to ^{3}He .

Note on units.

In this thesis we use conventional units used in low–temperature physics. In particular all energies are given in Kelvin (K), and lengths are given in units of $\sigma = 2.556\mathring{A}$.

2 Variational theory of solid and liquid ^{4}He

Variational methods[2, 21] represent one of the most successful approaches to the microscopic study of many body systems. It is based on the property of the ground state Ψ of a given system to minimize the functional $E_0 = \langle\Psi|\hat{H}\Psi|\rangle/\langle\Psi|\Psi\rangle$. For any other "trial" wave function Ψ_T the following inequality holds:

$$E_T = \frac{\langle\Psi_T|\hat{H}|\Psi_T\rangle}{\langle\Psi_T|\Psi_T\rangle} \geq E_0. \tag{2.1}$$

In this context it is assumed that within a given class of wave functions dependent on a set of parameters the best approximation to the ground state of the system is obtained minimizing the expectation value of the hamiltonian with respect to the parameters.

2.1 Trial wave functions

The major task in the variational computations is to find trial wave functions able to reproduce as closely as possible the exact ground state energy of the system considered. A trial wave function that provides energy upper bound close to E_0 may describe other important physical properties of the system very badly. It is therefore important that the

overlap between Ψ_T and Ψ_0 is as large as possible. This implies that the choice of the wave function must be done trying to include in it as much physics as possible. The usual way of building up a variational wave function for a quantum system of N strongly interacting objects is to write it in the form of a product:

$$\Psi_T(\mathbf{r}_1 \cdots \mathbf{r}_N) = F(\mathbf{r}_1 \cdots \mathbf{r}_N)\varphi(\mathbf{r}_1 \cdots \mathbf{r}_N), \tag{2.2}$$

where $\{\mathbf{r}_1 \cdots \mathbf{r}_N\}$ are the coordinates of the particles. $\varphi(\mathbf{r}_1 \cdots \mathbf{r}_N)$ is a mean field solution embodying the phase and symmetry properties of the system, and $F(\mathbf{r}_1 \cdots \mathbf{r}_N)$ expresses the *dynamical correlations* induced amongst the particles in the system by the interaction.

Let us focus the attention on liquid and solid ^{4}He. The mean field factor $\varphi(\mathbf{r}_1 \cdots \mathbf{r}_N)$ is of the form:

$$\varphi(\mathbf{r}_1 \cdots \mathbf{r}_N) = \mathcal{S} \prod_i \varphi_i(\mathbf{r}_i), \tag{2.3}$$

where $\mathcal{S}$ is the symmetrization operator. The correlation factor can be expanded in the so called Feenberg form[2]:

$$F(\mathbf{r}_1 \cdots \mathbf{r}_N) = \exp\left[-\frac{1}{2}\sum_{i<j} u(r_{ij}) - \frac{1}{2}\sum_{i<j<k} u^{(3)}(\mathbf{r}_i, \mathbf{r}_j, \mathbf{r}_k) + \ldots\right], \tag{2.4}$$

Actual calculations do not consider explicit correlations involving more than three particles. The functions u,$u^{(3)}$,$\cdots$ are called *two–, three–,... body pseudopotentials*, and $\exp\left[-\frac{1}{2}\sum_{i<j} u(r_{ij})i\right]$, $\exp\left[-\frac{1}{2}\sum_{i<j<k} u^{(3)}(\mathbf{r}_i, \mathbf{r}_j, \mathbf{r}_k)i\right]$,..., two–, three–,... body correlation factors.

The main role of F is to correct the independent particle wave function φ at short interparticle distances, where the strong repulsion of interactions of the Lennard–Jones type prevent the ^{4}He atoms to come too close. In fact, perturbative corrections to the mean field hamiltonian associated with φ, are very large if not divergent, due to the repulsive core of the interaction. However, F has an important role also at large interparticle distances,

due to long range correlations present in the quantum system, which are intimately related to phonon collective excitations.[33] In the following sections we will introduce briefly the main trial wave functions of the Feenberg form that have been used in the studies of ^{4}He.

2.2 Mean field factor

In the Bose case the mean field solution is the fully degenerate independent particle wave function, namely $\varphi_i(r) = \varphi(r)$ for $i = 1 \ldots N$ and $|\varphi(r)|^2$ is proportional to the one body density of the system. Therefore $\varphi(r)$ is a constant in the homogeneous liquid, and a single particle function satisfying proper boundary conditions for a liquid with a free surface[18] or a droplet[16]. In order to have a localization of the particles on the sites of some given lattice it is in general necessary to modulate the wave function with a one body term consisting on gaussians centered on the appropriate positions. Such factor is known as *Nosanow factor*[34]:

$$\varphi_N = S \prod_{i=1}^{N} e^{-C(\mathbf{r}_i - \mathbf{s}_i)^2}, \tag{2.5}$$

where C is considered as a variational parameter. The Nosanow factor breaks explicitly the translational symmetry of the wave function. The symmetrization is expected to have little effect because the exchange probability in the solid is depressed by the strong localization, and in most of the calculations it has been neglected.

2.3 Jastrow wave function

The simplest form of trial wave function can be obtained truncating F at the two–body level:

$$\Psi_J(\mathbf{r}_1 \cdots \mathbf{r}_N) = \prod_{i<j} f(r_{ij}) \varphi(\mathbf{r}_1 \cdots \mathbf{r}_N), \tag{2.6}$$

where:

$$f(r_{ij}) = e^{-\frac{1}{2}u(r_{ij})} \tag{2.7}$$

is called Jastrow correlation factor[35]. The first application in a variational calculation is due to McMillani[36], that used a short ranged inverse power pseudopotential

$$u(r) = \left(\frac{b}{r}\right)^5, \tag{2.8}$$

resulting from the exact short range behaviour of the solution of the Schrödinger equation with a Lennard–Jones potential. The use of a short ranged wave function is not correct in principle, because it has been proved that the pseudopotential, should behave at large distances as $1/r^2$[33]. However the long range behaviour of $f(r)$ at large distances has little effect on the energy estimate, and therefore is often neglected in calculations. The variational energy obtained with such wave function is still quite high ($E_0 = -5.72K$ when $b = 1.2\sigma, \sigma = 2.556$Å). Nevertheless it represents an useful starting point for further developments of more sophisticated wave functions.

2.4 Jastrow + Triplet wave function

A better trial wave function that includes explicit three body correlation (triplet correlation)[37] was introduced both in VMC[38] and HyperNetted Chain (HNC)[39, 40] studies, to simulate Feynman–Cohen backflow[41]. It is obtained multiplying the Jastrow form by a triplet

term:

$$\Psi_{JT} = e^{-T_3} = \prod_{i<j<k} e^{-\frac{1}{2}\sum_P \xi(r_{ij})\xi(r_{ik})\mathbf{r}_{ij}\cdot\mathbf{r}_{ik}}\Psi_J, \tag{2.9}$$

where P are cyclic permutations over the three indexes. The three–body pseudopotential in eq. (2.9) can be rewritten as:

$$\frac{1}{2}\sum_P \xi(r_{ij})\xi(r_{ik})\mathbf{r}_{ij}\cdot\mathbf{r}_{ik} = \frac{1}{4}\sum_{i=1}^{N}\mathbf{G}(i)\cdot\mathbf{G}(i) - \frac{1}{2}\sum_{i<j}\xi(r_{ij})^2 r_{ij}^2, \tag{2.10}$$

where

$$\mathbf{G}(i) = \sum_{\substack{j=1\\ j\neq i}}^{N} r_{ij}\xi(r_{ij}). \tag{2.11}$$

This expression is more convenient in Monte Carlo computation because involves only updating the pair form $\mathbf{G}(i)$. A possible parametrization of the functions $\xi(r)$ is that employed in ref. [42]:

$$\xi(r_{ij}) = \sqrt{\lambda}e^{\left(\frac{r-R_0}{\omega}\right)^2}\left(\frac{r-r_c}{r_c}\right)^2. \tag{2.12}$$

The parameter r_c is a cutoff distance introduced not to have discontinuities in the logarithmic derivative of the wave function at the border of the simulation box. The other parameters are the strength λ, the position and the width of the gaussian. The triplet correlation provides a localization of the particles at a distance R_0 depending on the angles between the directions joining the three particles. The results obtained with the introduction of a three body correlations give a substantial improvement with respect to the Jastrow form. In particular at $\rho\sigma^3 = 0.365$, the equilibrium density in ^{4}He, the upper bound for the energy per particle is $E_0 = -6.674 \pm 0.007\ K$. Also in the solid phase, simulated multiplying the trial wave function by the Nosanow factor, the triplet gives a better energy, that is $E_0 = -3.786 \pm 0.014\ K$ at density $\rho\sigma^3 = 0.550$, to be compared with $E_0 = -3.322 \pm 0.019\ K$ given by the Jastrow+Nosanow wave function at the same density.

$\rho\sigma^3$	EMC	Vitiello–Schmidt	DMC
0.327	-6.8543 ± 0.0022	-6.804 ± 0.015	-7.0117 ± 0.0018
0.365	-6.9014 ± 0.0037	-6.862 ± 0.016	-7.1432 ± 0.0038
0.401	-6.6427 ± 0.0029	-6.524 ± 0.020	-7.0166 ± 0.0054
0.438	-5.9911 ± 0.0076	-5.837 ± 0.023	-6.5105 ± 0.0060

Table 2.1: Energy per particle (in Kelvin) for optimized variational wave functions in ^{4}He compared with DMC results for four densities in the liquid branch of the equation of state. (From ref. [47]).

2.5 Wave Function Optimization

The optimization of variational wave functions is a long standing problem, and many attempts have been done both in HyperNetted Chain (HNC, FHNC)[43, 44, 45] theories and more recently within the Variational Monte Carlo[46] method. This studies, before limited to the Jastrow term, have recently been extended to the whole wave function by Moroni, Fantoni and Senatore[47]. They use the so called Euler Monte Carlo procedure, that is based on the minimization of a linear combination of the energy expectation value and the variance, using the reweighting method. The variational energies obtained with these optimized wave functions in ^{4}He are only 3% different from the experimental results at the equilibrium density (see table 2.1).

3 The Shadow Wave Function

The variational theory, discussed in the previous chapter, proved to be quite successful in describing several aspects of the ground state of Bose and Fermi many–body systems. However there are a certain number of questions concerning the liquid–solid phase transition, the description of the phase coexistence and in general the description of inhomogeneous systems, that cannot be faced with, in a satisfactory manner, by using the conventional variational techniques. We saw that the solid phase can be reasonably worked out only assigning *a priori* equilibrium positions for the atoms. Similarly, the description of clusters or free surfaces can only be obtained introducing suitable one body terms between the correlations.

Simulations of classical ensembles have shown that the symmetry breaking occurring at some freezing density is present even for interactions that are translationally invariant [48, 49, 50]. We would like to have a formalism in which this spontaneous symmetry breaking appear also for quantum systems.

The Shadow Wave Function (SWF)[24, 25] , originally proposed by Vitiello, Runge and Kalos in 1988, meets all these requirements: it is fully translational invariant, and nonetheless provides a stable solid phase without any external given equilibrium sites. Its use revealed to be successful in describing a wide category of phenomena in ^{4}He, amongst

which, the elementary excitation spectrum[51] and the simulation of a vortex line [52]. In this chapter we describe the general features of SWF and some of the results obtained by its application in studying homogeneous phases of ^{4}He.

3.1 Original formulation of the SWF formalism.

The Shadow Wave Function for a systems of N bosons has the form:

$$\Psi(R) = \int K(R,S)\psi_s(S)dS, \tag{3.1}$$

where $R \equiv \{\mathbf{r}_1, \ldots, \mathbf{r}_N\}$ and $S \equiv \{\mathbf{s}_1, \ldots, \mathbf{s}_N\}$. The auxiliary variables S are called "shadows". The kernel K is factorized in a Jastrow term involving only the real degrees of freedom and a coupling term:

$$K(R,S) = \psi_r(R) \prod_k \theta(\mathbf{r}_k - \mathbf{s}_k). \tag{3.2}$$

The analytic expression of $\psi_r(R)$ and $\psi_s(S)$ are of the Jastrow form

$$K(R,S) = e^{-\frac{1}{2}\sum_{i<j} u_{pp}(r_{ij}) - C\sum_i |\mathbf{r}_i - \mathbf{s}_i|^2}, \tag{3.3}$$

$$\psi_s(S) = e^{-\frac{1}{2}\sum_{i<j} u_{ss}(s_{ij})}. \tag{3.4}$$

We will refer to u_{pp} and u_{ss} as particle–particle and shadow–shadow "pseudopotentials". Correspondingly $e^{-\frac{1}{2}u_{pp}}$ and $e^{-u_{ss}}$ are the particle–particle and shadow–shadow correlation functions, which tend to 1 for large interparticle distances. The coupling term between particles and shadows is short–ranged and vanishes for large separation of the particle–shadow distances $(\mathbf{r}_i - \mathbf{s}_i)$. It is taken of the gaussian form which resembles the Nosanow factor employed in the variational calculations for quantum solids:

$$\theta(\mathbf{r} - \mathbf{s}) = e^{-C(\mathbf{r}-\mathbf{s})^2}, \tag{3.5}$$

where C is a variational parameter.

The McMillan form:

$$u_{pp} = \left(\frac{b_p}{r}\right)^5, \tag{3.6}$$

with b_p as variational parameter, provides a reasonable representation for the particle–particle pseudopotential u_{pp}. This can be optimized with the procedure mentioned in the previous chapter, as done by Vitiello and Schmidt, and more recently by Moroni et al. Similarly, u_{ss} can be taken of the McMillan form,:

$$u_{ss} = \left(\frac{b_s}{s}\right)^{m_s}. \tag{3.7}$$

with both b_s and m_s as variational parameters. We will label this form of the SWF as $M(R) + M^{m_s}(S)$, where M stands for McMillan. The optimized form of the particle–particle pseudopotential will be indicated with $O(R)$. At present a derivation of the shadow–shadow correlations by Euler equation is still absent, and the optimization is still based on the search of better analytic forms of the pseudopotential u_{ss}.

With SWF many–body correlations at any order are introduced in the system[25, 26]. This is illustrated in figure 3.1-b, where it is made evident that each particle is correlated through the shadow–shadow correlations to all the other particles. Analytically this might be seen through a cluster expansion of the shadow integral, in which two, three, four... body terms explicitly appear.

3.2 Justifications for SWF form

Two kinds of heuristic justifications for the choice of the integral form for a variational wave function have been given in the literature. The first one is based on an imaginary time propagation of the trial wave function, similarly to what is done in GFMC calculations[24].

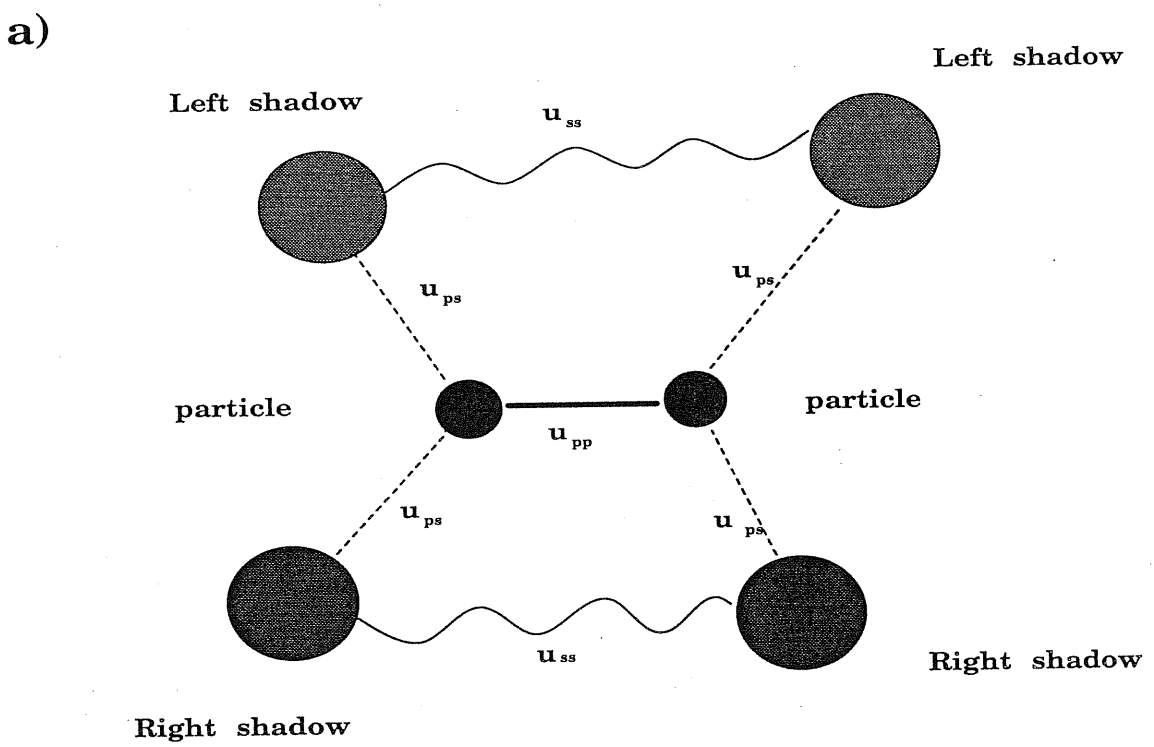

Figure 3.1: a) Cluster diagram illustrating interactions between particles and shadows [26]. Black circles represent atoms, while gray circles represent shadows. Full line: p–p interaction; wavy line: s–s interaction; dashed line: p–s interaction.

b) With SWF one has explicit two body correlation amongst atoms (first term) but also indirect correlations at higher order (second term illustrates an indirect three–body correlation).

The second one is based on a Lie–Trotter expansion of the density matrix that leads to a path–integral representation[53].

3.2.1 GFMC-like scheme

Let us consider some trial many body wave function $\Psi_0(R,t)$, where R is the set of the N particles coordinates. We can propagate it in imaginary time τ according to Schrödinger's equation.

$$\frac{\partial}{\partial\tau}\Psi_0(R,\tau) = \hat{H}\Psi_0(R,\tau). \tag{3.8}$$

The solution of this equation at a certain time τ can be written in terms of the eigenstates φ_l of $\hat{H}$ and of the trial wave function at some initial time τ_0:

$$\Psi_0(R,\tau) = \sum_l e^{-\frac{1}{\hbar}(E_l-E_0)(\tau-\tau_0)}|\varphi_l(R)\rangle\langle\varphi_l(R)|\Phi_0(R,\tau_0)\rangle. \tag{3.9}$$

If we let $\tau \to \infty$, and we assume that $\Phi_0(R,\tau_0)$ is not orthogonal to the ground state the sum reduces exactly to the ground state of the hamiltonian $\hat{H}$. In conclusion imaginary time propagation filters out from a given trial wave function the ground state component. We can propagate Ψ_0 inverting the operator $\hat{H}$. The formal inverse of the hamiltonian is the Green function, and the wave function at time $\Delta\tau$ can be written as:

$$\Psi_0(R,\Delta\tau) = \int G(R,S,\Delta\tau)\Psi_0(S,0)dS. \tag{3.10}$$

One can take for $G(R,S,\tau,\tau_0)$ the so called "short time approximation":

$$G(R,S,\Delta\tau) = \langle R|e^{-\Delta\tau\hat{H}}|S\rangle = \langle R|e^{-\Delta\tau[T+V(S)]}|S\rangle. \tag{3.11}$$

Let us assume now that the Fourier transform of the Jastrow functions $\varphi(R) = \prod_{i<j} f(r_{ij})$ are eigenstates with eigenvalue $-\frac{\hbar}{2m}\sum_i k_i^2$. It is possible to expand the Fourier transform

of $G(R, S\Delta\tau)$ (neglecting the potential energy) on this approximate basis set. One gets:

$$G(R,S) = \varphi(R) \prod_{i=1}^{N} e^{-C|\mathbf{r}_i - \mathbf{s}_i|^2} \varphi(S) \tag{3.12}$$

The imaginary time interval $\Delta\tau$ has been reinterpreted here as a variational parameter. If we pose:

$$\psi_p(R) = \varphi(R) \qquad \psi_s(S) = \varphi(S)\Psi_0(S), \tag{3.13}$$

using the McMillan form for both φ's and Ψ_0 leads to the SWF of eqs. (3.1)–(3.7) This scheme suggests that SWF overlaps the real ground state better than the starting trial function, indicating also a possible scheme of systematic improvement based on the search of a more realistic kernel in eq. (3.10).

3.2.2 Path Integral scheme

A more suggestive interpretation of the SWF expression can be given in terms of a path integral decomposition of the density matrix of the N He atoms. The density matrix at temperature $T = (K_B\beta)^{-1}$ is defined as:

$$\langle R|e^{-\beta\hat{H}}|R'\rangle. \tag{3.14}$$

Let us expand the diagonal elements inserting a certain number $\nu - 1$ of projectors in coordinates space and summing over all the possible permutations:

$$\langle R|e^{-\beta\hat{H}}|R\rangle = \sum_P \int dR^1 \cdots dR^{\nu-1} \langle R|e^{-\frac{\beta\hat{H}}{\nu}}|R^1\rangle \cdots \langle R^{\nu-1}|e^{-\frac{\beta\hat{H}}{\nu}}|R\rangle.$$

The result is a mapping of the original quantum systems onto ν replicas each at an higher effective temperature $\beta' = \beta/\nu$. If ν is large enough we can use for each subsystem the

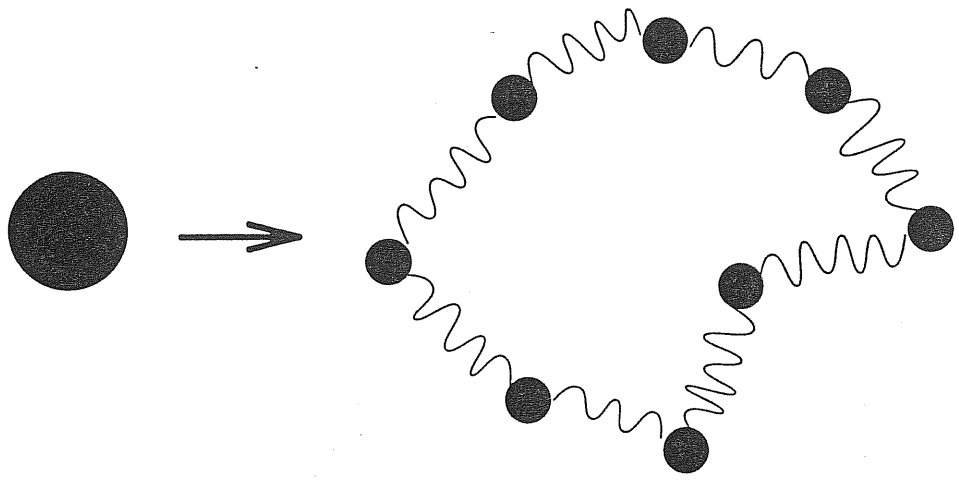

Figure 3.2: In the PIMC scheme each particle is mapped on a polymer connected via harmonic potentials.

quasi classical approximation for the partition function:

$$\langle R^{\alpha}|e^{-\frac{\beta\hat{H}}{\nu}}|R^{\alpha+1}\rangle \simeq$$
$$e^{-\beta V(R^{\alpha})/2\nu}\prod_{i=1}^{N} e^{-K_{\nu T}|\mathbf{r}_i^{\alpha}-\mathbf{r}_i^{\alpha+1}|^2} e^{-\beta V(R^{\alpha+1})/2\nu}, \tag{3.15}$$

with $K_{\nu T} = \frac{mK_B\nu T}{\hbar^2}$. Here V($R$) is the potential energy appearing in the hamiltonian, and m is the mass of the atoms. The quantum problem has been translated into a classical one. The position of one particle is associated with $\nu - 1$ positions. The elements of this set of coordinates corresponding to a given particle are connected to each other via an harmonic potential, giving rise to a sort of flexible polymer (see fig. 3.2). The original quantum problem is recovered tracing the positions of all the monomers but one. Moreover the Bose statistics requires that the particles are indistinguishable. This allows in principle for a crossing of the monomers belonging to different particles, and is mathematically realized summing over all the possible permutations of the particle index in each set of coordinates.

We must now add a further consideration. We are mainly concerned in condensed phases of helium. In liquid phase the structure is such that each atom is surrounded by a cage of neighbours and the shape of the polymers associated to each particle must be rather compact. In the solid phase particles reside on precise positions, and neither wide motion nor wide delocalization are allowed. In such conditions it is reasonable to think that the motion of the polymeric structure can be decomposed in the motion of the center of mass of the structure and the motion of the particles confined through an harmonic potential around the center of mass. In this picture the shadow becomes a representation of the correlation hole carried around by the helium atom. We expect from this scheme that shadows are more rigid and localized than the real degrees of freedom, as it is in fact observed.

3.2.3 Physical interpretation

The SWF is a powerful ansatz to satisfy the minimal requirements to describe, both the homogeneous and inhomogeneous phases which is crucial to study the liquid–solid coexistence and interface:.

–translational invariance

–full permutation symmetry (proper for the Bose systems)

We mentioned above that shadow degrees of freedom are more rigid, and represent the motion of the centers of mass of the particles. Their behaviour is very much like that of classical particles interacting via a potential that is the correlation pseudopotential between the shadows. If we consider for instance the simple case described above, we can think to the shadows, in a very rough approximation, as if they were a classical ensemble of soft spheres, that is objects interacting via an inverse power potential $\epsilon(b/r)^n$. Real particles are centered in the shadow positions and are delocalized within a distance

inversely proportional to the parameter C. It is known from classical simulations that soft-spheres ensembles crystallize spontaneously above a given density that is a given fraction of the close packing density depending on the exponent n. The shadow degrees of freedom behave exactly in the same way. Once the density reaches a large enough value, the stable phase is that of an fcc crystal. Such mechanism would work also for trial wave functions of Jastrow or Jastrow+Triplet form. The point is that in this case, crystallization can be achieved only enlarging the repulsive core. The localization imposed to the particles increases the kinetic energy, in such a way that the resulting upper bound for the energy per particle results too high. With SWF crystallization is obtained only through the auxiliary degrees of freedom, and the kinetic energy of atoms is adjusted by the delocalization of the atoms around the shadows.

As we will see in the following of this chapter, the values of the parameters optimizing the energy are density dependent. that obviously poses serious problems in treating liquid–solid coexistence. Such difficulties are overcome by the LD–SWF as discussed in chapter 4.

3.3 Improved shadow–shadow pseudopotentials

In absence of Euler equations for u_{ss} and $\theta(\mathbf{r}-\mathbf{s})$, one can use the path integral scheme to have information on their analytical structure. The particle–particle correlation should mimic the effect of the strongly repulsive core of the potential that is effective in the monomer–monomer interaction[53]. The correlation between the centers of mass of the polymers is instead strictly connected to the interatomic potential $V(r)$, because the whole strength of the interaction has to be recovered averaging over the ν monomers. This suggests the presence of an attraction which can be simulated by a shifted and rescaled

form of the Aziz potential ($A(S)$), that is:

$$u_{ss}(s) = \alpha V(\delta s) \tag{3.16}$$

The parameter α can be interpreted as an effective temperature, and δ as the displacement of the minimum of the interaction due to the spreading of the chains. This form of the wave function has been widely explored by McFarland et.al.[54]. The energy upper bounds results to be significantly lowered with respect to the $M(R) + M^{m_s}(S)$ case, and also the correlation functions are much closer to the GFMC results. A similar effect can be reached substituting the rescaled and shifted Aziz with a combination of renormalized Aziz and McMillan pseudopotential ($MA(S)$)[55]:

$$u_{ss}(s) = \epsilon V(s) + \left(\frac{b_s}{s}\right)^{m_s} \tag{3.17}$$

This last form accounts in a slightly different way for the interaction between the centers of mass, because here the Aziz potential appears as it is except for the rescaling due to the effective temperature, and the McMillan part reflects the correlation between the particles, dressing the free particle density matrix. We have explored this alternative parametrization that looks much simpler in view of dealing with inhomogeneous systems. The results that can be obtained are comparable to the rescaled Aziz form.

Another relevant improvement is obtained optimizing the particle–particle correlation in the same way done for the Jastrow + Triplet wave function[56].

As mentioned a full optimization based on Euler equations is still lacking. Some preliminary studies were performed with reweighting techniques on the local energy and on its variance. They indicate that a minimization of this kind is possible only for the parameters b_p and C. Several problems arise in optimizing u_{ss}. The reweighting is not efficient for u_{ss}, because it does not enter explicitly in the local energy expression. Moreover we could not find clear minima in the variance.

It would be interesting in this context to study $\frac{\partial \langle H \rangle}{\partial u_i}$ in HNC. This scheme, which has been recently applied to SWF[26], may provide useful informations about the long range properties of the correlation functions.

3.4 Results for Liquid Phase

We summarize here the results obtained with SWF in the fluid phase of ^{4}He ($0.327 \leq \rho\sigma^3 \leq 0.438$)[24, 56], compared with results of other variational wave functions and with DMC[47] results.

Variational energy and equation of state

In table 3.1 we report the energy per particle at the experimental equilibrium density for Jastrow, Jastrow + Triplet, Shadow, Diffusion Monte Carlo (DMC) and experiment[57]. The gain in energy for the McMillan shadow–shadow correlation is not so high, even if large improvement is obtained with respect to the pure Jastrow case. Adding the attractive part the energy upperbound lowers consistently, and a further optimization u_{pp} gives a result that is only $0.1K$ higher than the Jastrow + Triplet result and $0.3K$ above the DMC and experimental value.

In fig. 3.3 we report the fluid branch of the SWF equation of state for $M(R)+M^{m_s}(S)$, $M(R)+A(S)$ and $O(R)+A(S)$ compared with DMC results. The calculated equilibrium density coincides in all cases and is very close to the experimental value. In table 3.3 we list the results for the energy per particle at four densities in the liquid. The freezing density is underestimated in the $M(R)+M^9(S)$. In fact the value obtained from the Maxwell construction is $\rho\sigma^3 = 0.420$, to be compared with the value 0.438 of both DMC and $O(R)+A(S)$. Nevertheless all the most important features in the equation of state are

Ψ_T	$E \pm \Delta E$
Jastrow	-5.717 ± 0.021
Jastrow+Triplet	-6.674 ± 0.007
fully optimized	-6.9014 ± 0.0037
$M(R) + M^5(S)$	-6.241 ± 0.035
$M(R) + A(S)$	-6.55 ± 0.01
$O(R) + A(S)$	-6.789 ± 0.023
DMC	-7.1432 ± 0.0038
Experiment	-7.14 ± 0.01

Table 3.1: Energy per particle at equilibrium density $\rho\sigma^3 = 0.365$ for some variational wave functions, DMC and experiment. (From refs. [56] and [47])

maintained, making reasonable the use of $M(R) + M^9(S)$ in describing the liquid phase.

Pair correlation functions

Another important comparison can be done looking at the pair correlation function[2], defined as:

$$g(r) = \frac{1}{N\rho} \sum_{i \neq j} \langle \delta(|\mathbf{r}_i - \mathbf{r}_j - \mathbf{r}|) \rangle .$$

In fig. 3.4 we report the results from $M(R) + M^9(S)$ shadow wave function and $M(R) + A(S)$ shadow wave function calculations, compared with DMC results. It can be immediately noticed that in the $M(R) + M^9(S)$ the peak of the nearest neighbours is lower of about 6% and shifted in of a 3% with respect to the DMC $g(r)$. The $M + A(S)$ form leads to a $g(r)$ that is only 1% lower than DMC, but still shifted of the same amount of the previous case. The shift is completely removed when an optimized pseudopotential for the

$\rho\sigma^3$		E_0
0.327		
	$M(R)+A(S)$	-6.561 ± 0.032
	$O(R)+A(S)$	-6.695 ± 0.027
	DMC	-7.0117 ± 0.0018
0.365		
	$M(R)+A(S)$	-6.599 ± 0.034
	$O(R)+A(S)$	-6.789 ± 0.023
	$M(R)+M^9(S)$	-6.165 ± 0.019
	DMC	-7.1432 ± 0.0038
0.401		
	$M(R)+A(S)$	-6.398 ± 0.019
	$O(R)+A(S)$	-6.615 ± 0.029
	DMC	-7.0166 ± 0.0054
0.438		
	$M(R)+A(S)$	-5.871 ± 0.016
	$O(R)+A(S)$	-6.286 ± 0.022
	$M(R)+M^5(S)$	-5.342 ± 0.012
	DMC	-6.5105 ± 0.0060

Table 3.2: Energy per particle at different densities in the fluid branch of the equation of state (from ref. [56] and ref. [47])

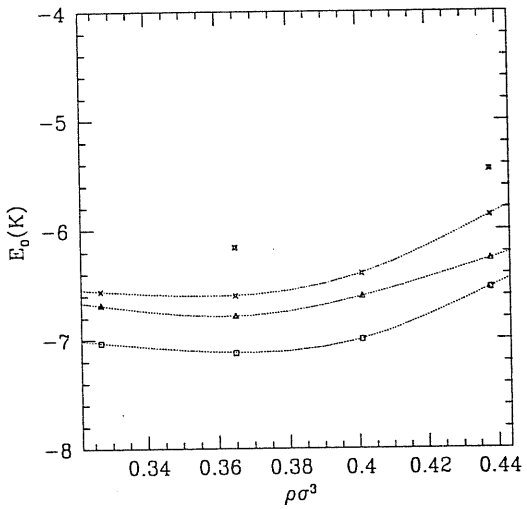

Figure 3.3: Equation of state in the fluid branch. Triangles: $O(R)+A(S)$; crosses: $M(R)+A(S)$; stars: $M(R)+M^n(S)$; open squares: GFMC.

particle–particle correlation is used, namely for the $O(R)+A(S)$ model. In this case $g(r)$ is practically indistinguishable from that of DMC, and for such readon is not reported in fig. 3.4.

There are other pair correlation functions which may be defined when using SWF. They have no direct physical meaning, but are useful to understand the behaviour of the auxiliary degrees of freedom in the system. The shadow–shadow correlation function $g_{ss}(r)$, shown in figure 3.5, is defined as:

$$g_{ss}(r) = \frac{1}{N\rho}\sum_{i\neq j}\langle\delta(|\mathbf{s}_i - \mathbf{s}_j - \mathbf{r}|\rangle.$$

According to the path integral scheme, the shadows result more localized than the particles, and the nearest neighbours peak is higher than in $g(r)$. Also the peaks corresponding

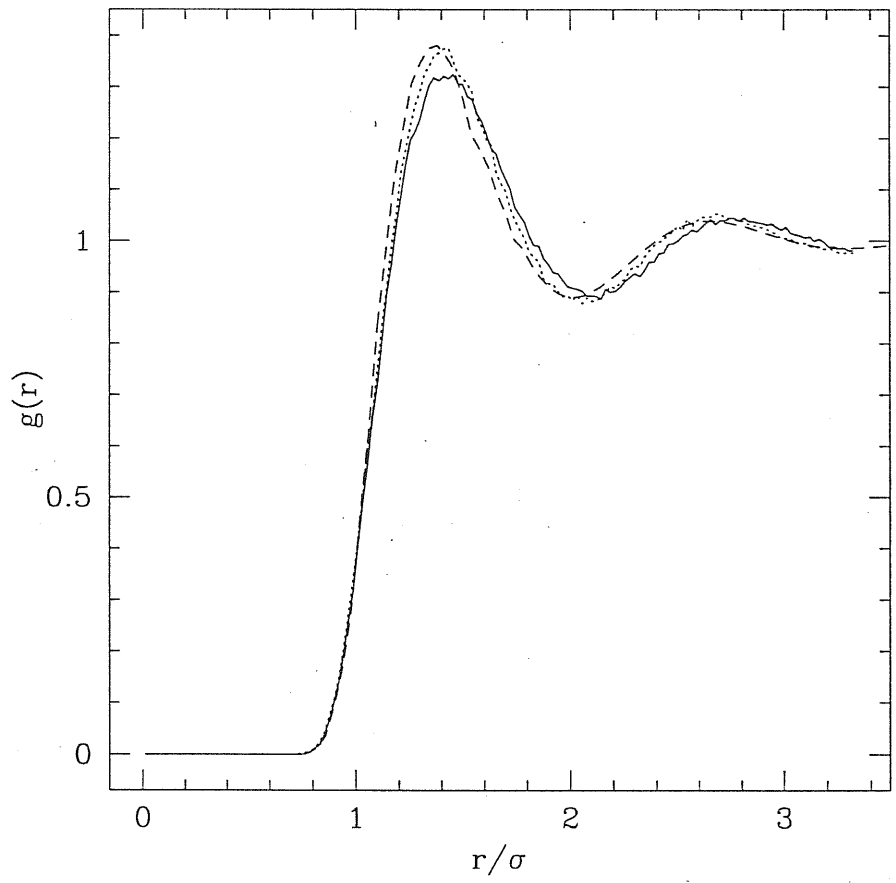

Figure 3.4: Pair correlation functions for particles. Solid line: $M(R) + M^9(S)$;dotted line: $M(R) + A(S)$; dashed line: DMC

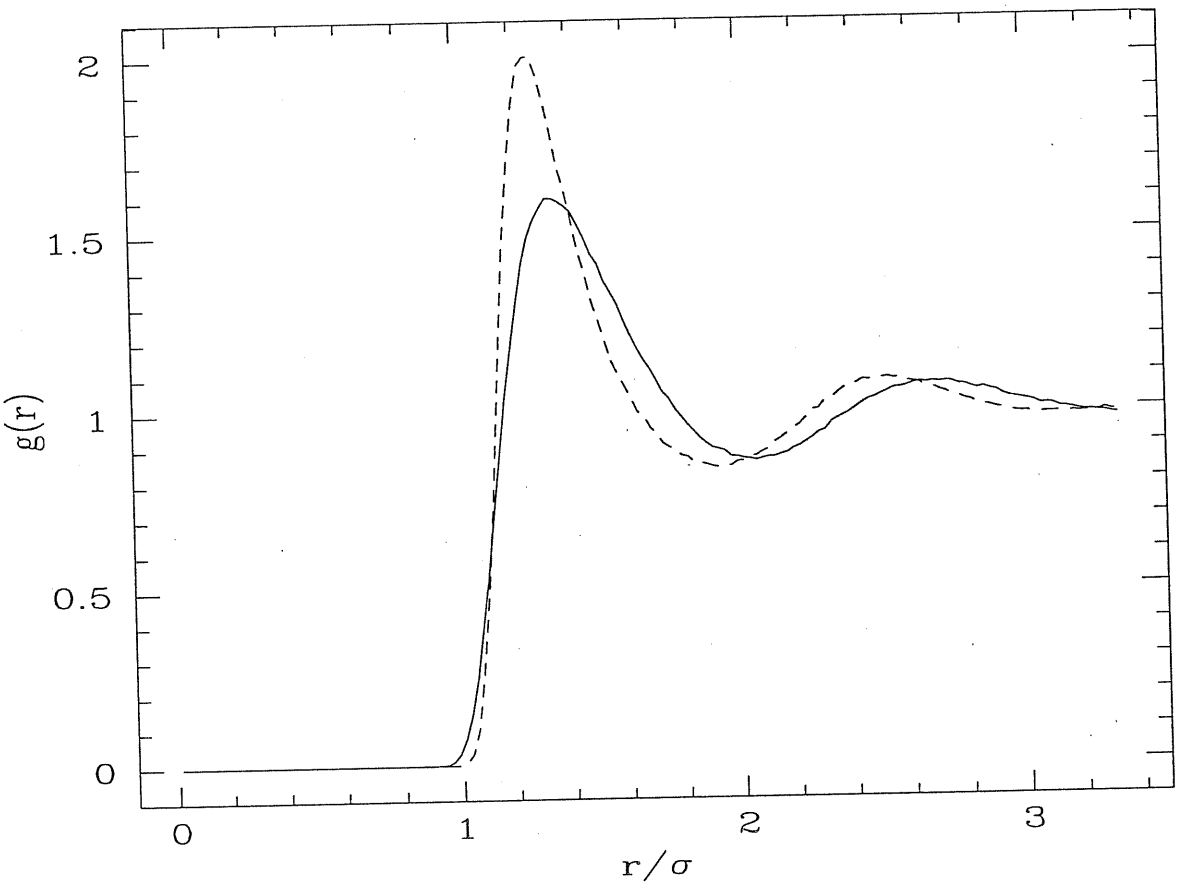

Figure 3.5: Pair correlation function for shadows at equilibrium density $\rho\sigma^3 = 0.365$. Solid line: $M(R) + M^9(S)$; dashed line: $M(R) + A(S)$.

to the successive shells appear more pronounced.

Particle–shadow correlations:

$$g_{p_i s_i}(r) = \frac{1}{\rho} \sum_i \langle \delta(|\mathbf{r}_i - \tilde{\mathbf{s}_i} - \mathbf{r}|) \rangle.$$

give important information on the relative distribution of particles and shadows with the same index. Shadow left–shadow right correlation function measures the relative distribution of shadows of different kind (see appendix A):

$$g_{s^L s^R}(r) = \frac{1}{N\rho} \sum_{i,j} \langle \delta(|\mathbf{s}_i^L - \mathbf{s}_j^R - \mathbf{r}|) \rangle.$$

Both of them are plotted in fig. 3.6. $g_{p_i s_i}(r)$ (on the left) reflects the gaussian shadow–particle correlation in eq. (3.3), while $g_{s^L s^R}(r)$ (on the right) shows a peak at $r = 0$ due to the presence of the couple of shadows near a given particle, and subsequently shows a structure similar to that of $g(r)$ or $g_{ss}(r)$.

Condensate fraction

Another interesting quantity is the one body density matrix, given by:

$$n(r) = \frac{\int dR \Psi(\mathbf{r}_1, \cdots, \mathbf{r}_i', \cdots, \mathbf{r}_N) \Psi(\mathbf{r}_1, \cdots, \mathbf{r}_i, \cdots, \mathbf{r}_N)}{\int dR |\Psi(R)|^2}. \tag{3.18}$$

In term of n(r) the condensate fraction is given by[58]:

$$n_0 = \lim_{r \to \infty} n(r). \tag{3.19}$$

The actual way of computing this quantity is somewhat difficult. Nevertheless it has been possible to estimate n_0, that results to be of the 4.5% in the case of the McMillan shadow–shadow correlation[24], and of the 7.1% in the case of the rescaled Aziz without particle–particle optimization[54]. This has to be compared with the 9.35% of the GFMC[59], and 8.1% of DMC [47].

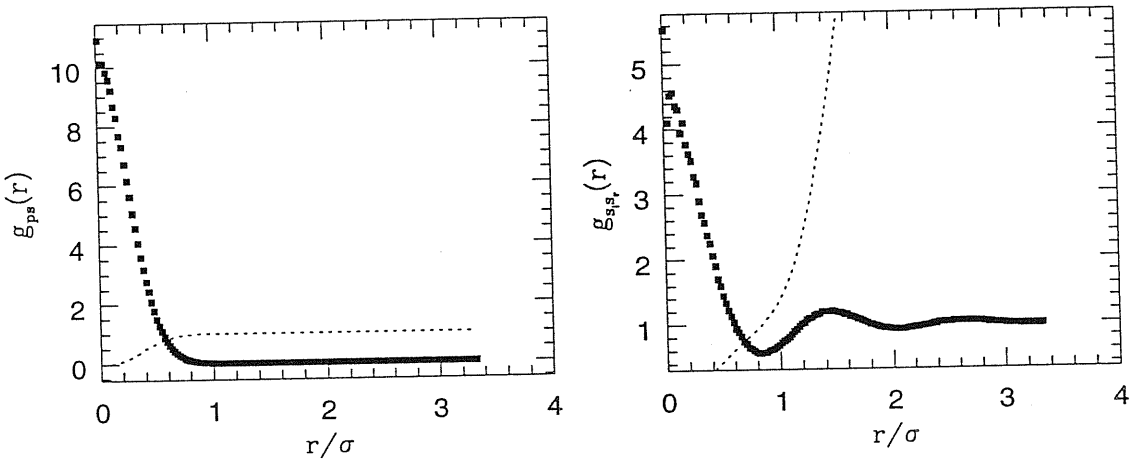

Figure 3.6: Particle–shadow and shadow left–shadow right correlation functions

3.5 Results for the solid phase

As discussed above, the most important feature of the shadow wave function is the capability of describing the solid phase without imposing any constraint on the equilibrium positions of the atoms. This feature has been shown by numerical simulations carried out in the range of density $0.491 \leq \rho\sigma^3 \leq 0.589$, in simulation boxes compatible with a fcc lattice.[1]

As for the liquid phase we report the main results compared with GFMC.

[1]The experimentally found structure for solid ^{4}He is hexagonal close packed (hcp), which differs from fcc for the different stacking order of the hexagonal planes (that have (111) indexes in fcc and (100) indexes in hcp). The difference in energy among these structures is not very high, and computationally fcc is simpler to deal with.

$\rho\sigma^3$		E_0
0.491		
	$M(R)+A(S)$	-5.052 ± 0.014
	$O(R)+A(S)$	-5.414 ± 0.019
	$M(R)+M^5(S)$	-4.968 ± 0.018
	GFMC	5.61 ± 0.03
0.550		
	$M(R)+A(S)$	-3.639 ± 0.012
	$O(R)+A(S)$	-3.765 ± 0.012
	$M(R)+M^{12}(S)$	-3.557 ± 0.010
	GFMC	4.197 ± 0.03
0.589		
	$M(R)+A(S)$	-1.947 ± 0.012
	$O(R)+A(S)$	-2.132 ± 0.012
	GFMC	-2.70 ± 0.06

Table 3.3: Energy per particle at different densities in the solid branch of the equation of state (from ref [56])

Variational energies

In table 3.3 the results in the solid phase are reported for three different densities above the melting point.

As in the liquid case, the use of the rescaled Aziz pseudopotential for u_{ss} improves considerably the results. However the $M(R)+M^{m_s}(S)$ model reproduces the slope of the equation of state, and also the melting density as described by the Maxwell construction.

An important feature that can be observed analyzing the optimal values of the variational parameters in the solid phase, is that the repulsive core of the shadow–shadow correlation must be considerably enlarged with respect to the liquid phase. This is due to the fact that the crystal is stable only if the radius of the correlation hole is larger than a given critical value, as will be discussed in detail in the next chapter.

Pair correlation functions

The analysis of the pair correlation functions in the solid phase shows a quite different behaviour of the particles and of the shadows. The peak corresponding to the nearest neighbours is about 50% lower than the peak of the shadows, the latter being comparable with the peak obtained in simulation of classical systems. The shadows show also in the subsequent cells the whole structure of a fcc lattice. On the contrary the structure in $g(r)$ is smoothed out, and only a shell structure similar to that of the liquid phase can be resolved, although the peaks are more pronounced. The effective localization of the atoms around the lattice sites can be checked using the Lindemann ratios or measuring a crystalline order parameter (that will be defined in a later chapter). As in the case of the liquid phase, the use of rescaled Aziz potential for u_{ss} provides results which are in better agreement with the GFMC than the $M(R) + M^{m_s}(S)$ case.

4 Local Density SWF

As discussed in the previous chapter, SWF have the merit of providing for a realistic description of both the solid and the liquid phase of ^{4}He, within the same functional form. The description of the solid liquid coexistence, and consequently of the interface, requires however a further step, that is the possibility of describing efficiently both the solid and the liquid without changing the values of the variational parameters. In this chapter we will describe an extension of the SWF which is suitable for inhomogeneous systems denoted as Local Density Shadow Wave Function (LD–SWF)[28].

4.1 General form of LD–SWF

Our purpose is to write down a variational wave function that can describe simultaneously the liquid and the solid phase. If we look at the results obtained in ^{4}He using the SWF, we can see that the values of the optimized variational parameters are indeed density dependent.

The relative variations differ for different parameters. For instance, in the case of $M(R) + M^{m_s}(S)$, the variation of b_p,in eq. (3.3) over all the interesting range of densities is of the order 1%. The other parameters C and b_s, instead, show a much wider dependence, on ρ .

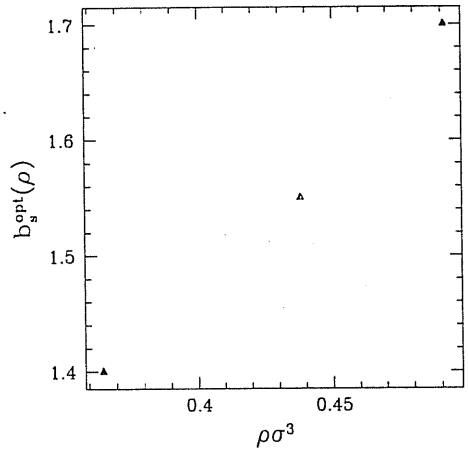

Figure 4.1: Optimized value of b_s in SWF for different values of the density.

The parameter C mainly controls the delocalization of particles around their centers of mass, and it results to be larger in the solid, where the average displacement is smaller. The role of b_s is to control the "width" of the correlation hole, and therefore it is crucial in determining the phase of the system, as it will be better explained in chapter 6.

In fig. 4.1 we show the values of b_s for $m_s = 5$ at different values of the density. From the figure one can see that b_s is roughly linear on ρ argued. One expects that the parametrization

$$b_s = b_0 + b_1\rho \tag{4.1}$$

reproduces the gross features of the optimized results. In general one could think to express every parameter as a function of ρ

$$\{\alpha\} \longrightarrow \{\alpha(\rho)\}.$$

In describing an inhomogeneous system, however, it is necessary to introduce a mechanism

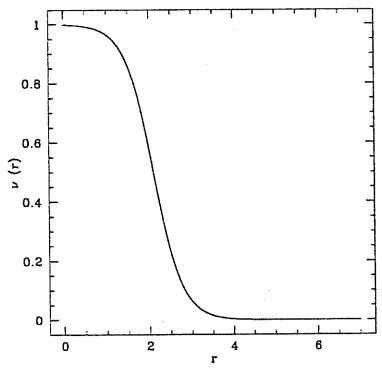

Figure 4.2: The function $\nu(r)$ for $\mu = 3.0$ and $r_c = 2.1$

that enables to fix ρ in the wave function according to the local value of the density. This can be done by calculating around each position $\mathbf{r}_i$ of the particles the density ρ with an operator $\hat{\rho}_i$, the Local Density Operator (LDO), defined by:

$$\hat{\rho}_i = \frac{1}{A}\sum_{l=1}^{N}\nu(r_{il}), \tag{4.2}$$

were the function ν is:

$$\nu(r) = \frac{1}{1+\exp[\mu(r-r_c)]}, \tag{4.3}$$

and A is a normalization constant given by

$$A = 4\pi\int r^2\nu(r)dr. \tag{4.4}$$

The operator $\hat{\rho}_i$ measures the local density in a limited region around the particle i. The quantity r_c represents the width of this region, while μ gives the steepness of the function at the edge. The function ν is plotted in fig. 4.2. In this way, the parameters are expressed as functions of the *local density operator*, namely:

$$\{\alpha\} \longrightarrow \{\alpha(\{\hat{\rho}_i\})\}, \tag{4.5}$$

From a formal point of view, a SWF with the above substitution (LD-SWF) is parametrized in such a way that its "variational" parameters are no more density dependent. Moreover in an inhomogeneous system LD–SWF can describe regions whose density presents variations on a scale of some r_c as efficiently as the optimized SWF, whereas in the interfacial region it provides a mechanism to adjust the density profile in a self consistent way.

The first realization of this idea has been done using the original form of the SWF $M(R) + M^{m_s}(S)$, that is taking a shadow–shadow correlation of the McMillan form, for which appears reasonable the linear ρ–dependence for the parameter b_s as suggested in eq. (4.1). The LD-SWF contains in general more variational parameters than the respective SWF. This additional parameters are the coefficients of the functional forms which fit the ρ dependencies, such as μ and r_c appearing in eq.(4.3). One should in principle perform a global minimization involving all the variational parameters. However, as discussed previously, the parameter whose density dependence is more important to characterize the phase of the system is b_s and the whole equation of state can be satisfactorily described fixing all the parameters but b_s . This assumption is reasonable, considering that the sensitivity of the estimated energy with respect to the other parameters with larger density dependence (as C) is not very high.

In the pair correlation term it is reasonable to consider as the value of the local density the average of the densities experienced by each particle:

$$\left(\frac{b_s}{r_{ij}}\right)^{m_s} \longrightarrow \left[\frac{b_0 + b_1\left(\frac{\hat{\rho}_i+\hat{\rho}_j}{2}\right)}{r_{ij}}\right]^{m_s} . \tag{4.6}$$

We will indicate this wave function as $M(R) + M(\hat{\rho}, S)_{m_s}$.

Alternatively the $M(R) + M(\hat{\rho}, S)_{m_s}$ parametrization may be viewed as the inclusion of higher order correlations among shadows. It is remarkable that such many–body correlations are essential in dealing with the liquid–solid interface.

4.2 Optimization procedure

We describe here the optimization procedure followed to find the functional form of LD–SWF. As previously discussed, b_s is the crucial parameter for the determination of the phase of the system. We have therefore followed the strategy to keep all the parameters fixed except b_s, in the minimization of the energy.

4.2.1 Optimization of b_s

Calculations for $E(b_s)$ has been carried out for the following densities:

- $\rho\sigma^3 = 0.365$ (equilibrium density);
- $\rho\sigma^3 = 0.438$ (freezing density from DMC);
- $\rho\sigma^3 = 0.550$ (a density well after the melting point).

Three different values for the parameter C, that is $C = 4\sigma^{-2}$ (optimal in the liquid), $C = 4.8\sigma^{-2}$ (optimal at melting) and $C = 5.7\sigma^{-2}$ (optimal at $\rho\sigma^3 = 0.550$) where considered. The values of the remaining variational parameters were kept fixed at the following values which better reproduce the $M(R) + M^{m_s}(S)$ equation of state over all the density range:

$$b_p = 1.12\sigma, \quad m_s = 9, \quad \mu = 3\sigma^{-1}, \quad r_c = 2.1\sigma.$$

The parameter b_p has a value that is slightly lower than the optimal one at the equilibrium density, but it describes the system better at intermediate densities. The exponent m_s is reasonably good both for liquid and solid. The values of μ and r_c have been fixed so that the average of the local densities reproduce the value of the average density ρ in an homogeneous system. This point will be discussed more widely in section 4.3. Simple

C	$b_{sh.opt}$	$\Delta b_{sh.opt}$	E_{var}	ΔE_{var}
4.0	1.21	0.11	-6.17	0.04
4.8	1.13	0.09	-6.13	0.05
5.7	1.05	0.06	-6.19	0.05

Table 4.1: Optimal values of b_{sh} , errors and correspondent energies in K obtained fitting MC results for $\epsilon(b_s)$ at several values of C and at density $\rho\sigma^3 = 0.365$

scanning on b_s have been performed, namely separate simulations have been carried out for each value of b_s. The runs at this stage consisted of 10000 MCS plus 2500 for equilibration, Statistical errors were computed from variance. Autocorrelations in this case do not exceed 10 MCS. The simulations started with a perfect fcc configuration with 108 particles.

4.2.2 Liquid phase

In the liquid phase the function $\epsilon(b_s)$ presents a minimum that has been accurately determined by fitting the results with a cubic polynomial. Results of the fit and relative values for the optimal energies are reported on table 4.1 The case for $C = 4$ is plotted in fig.4.3. It can be noticed that the energy per particle shows a jump approximately in correspondence of the value $b_s = 1.5$. For $b_s > 1.5$ no more melting is observed in the system. This fact points out very well the importance of the parameter b_s in determining the phase of the system. The presence of a critical value for the parameter, above which the system prefers the solid phase, has to be connected with the similar behaviour of classical ensembles interacting via purely repulsive potentials. If the core of the repulsion is increased above a critical value the crystalline packed phase is thermodinamically preferred to the disordered one. In chapter 6 this point will be better clarified also in connection with the critical properties of a system described by SWF.

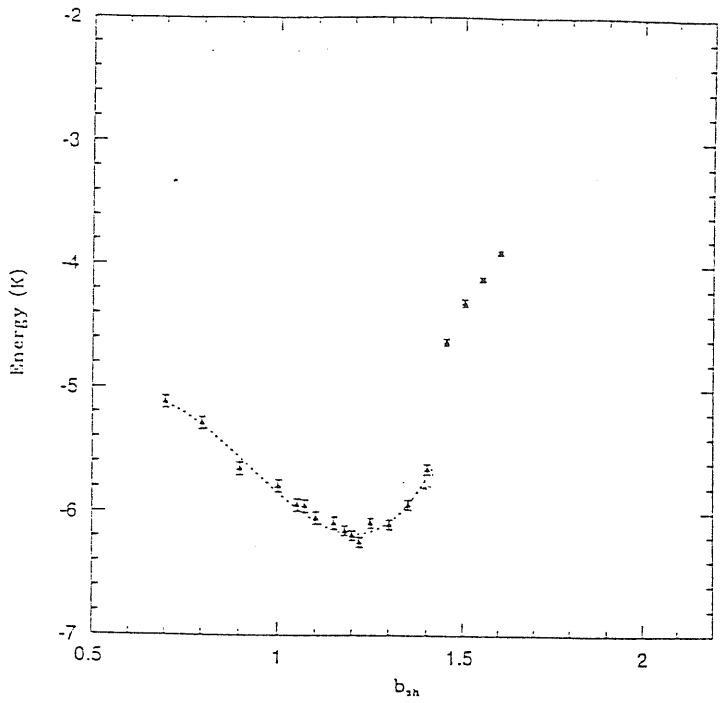

Figure 4.3: Energy as function of b_{sh} at density $\rho\sigma^3 = 0.365$ with other parameters fixed ($C = 4$)

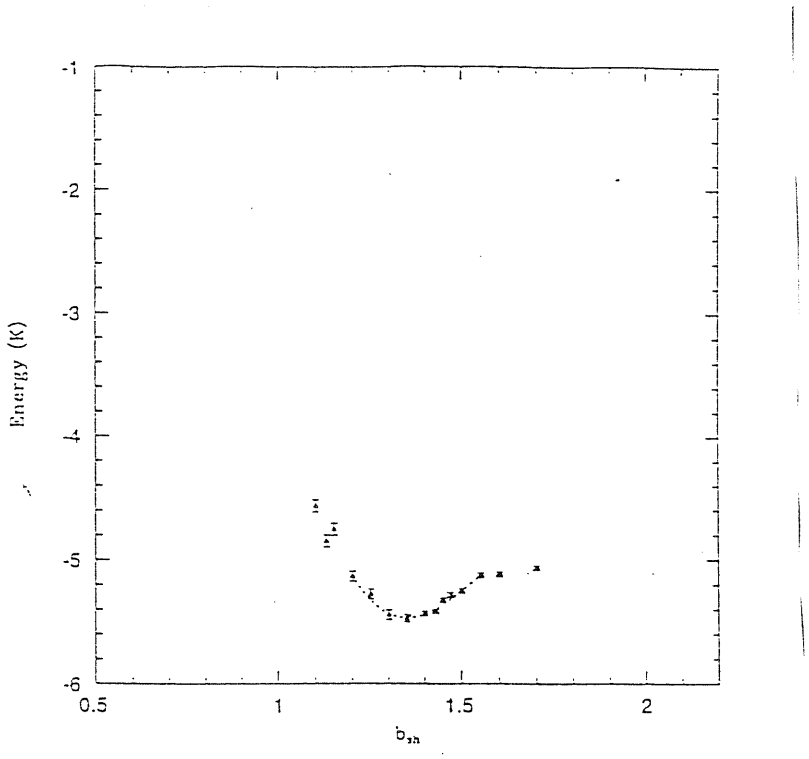

Figure 4.4: Energy as function of b_{sh} at density $\rho\sigma^3 = 0.438$ with other parameters fixed ($C = 4$)

4.2.3 Freezing density

At freezing density the situation is very similar to that of the liquid (see figure 4.4). The position of the minimum in this case is very close to the critical value of b_s, although the system is definitely in the liquid phase.[1] (see fig. 4.4). The results are also reported in table 4.2.

[1]The study of solid–liquid interface has shown that for LD-SWF the effective freezing density lies at a larger value, namely $\rho\sigma^3 = 0.449$

C	$b_{sh.opt}$	$\Delta b_{sh.opt}$	E_{var}	ΔE_{var}
4.0	1.35	0.08	-5.46	0.05
4.8	1.28	0.06	-5.51	0.04
5.7	1.18	0.07	-5.33	0.03

Table 4.2: Same as table 4.1, but at density $\rho\sigma^3 = 0.438$

4.2.4 Solid phase

In the solid phase the situation appears slightly different. Here the jumps in the energy per particle obtained for values of b_s below and above the critical one are larger, with lower values being associated with the solid phase. There is also a more pronounced dependence on C. Fig. 4.5 and fig. 4.6 shows the results for $C = 4$ and $C = 5.7$ respectively. In the first case no minimum for $\epsilon(b_s)$ appears, while for $C = 5.7$ a minimum can be observed just above the critical value of b_s. For $b_s \to \infty$ the energy tends to a constant value, consistently with the fact that this case corresponds to the Jastrow+Nosanow case. In fact, if b_s is too large the shadows are nearly blocked in their initial configuration,

4.2.5 Linear Interpolation

The results given above are compatible with a linear dependence of the parameter b_s as a function of the density, as illustrated in figure 4.7. The results for the coefficients are given in table 4.3. For $C = 4$ the sensitivity of the energy per particle on b_s in the solid phase lower than for $C = 4.8$ or $C = 5.7$. For this reason the value $C = 4$ has been chosen.

The linear fit matches well the values obtained in this first optimization, as can be seen in fig. 4.7.

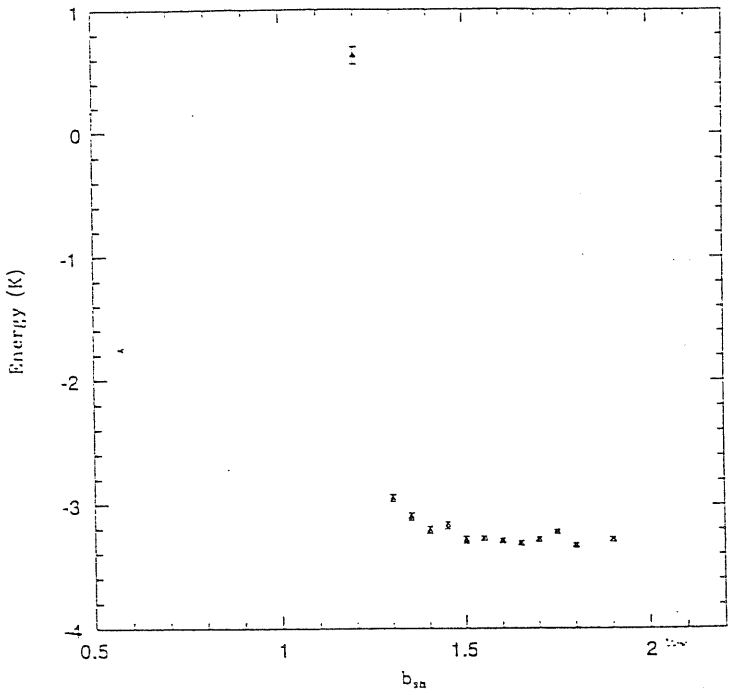

Figure 4.5: Energy as function of b_{sh} at density $\rho\sigma^3 = 0.550$ with other parameters fixed ($C = 4$)

$C\sigma^2$	b_0/σ	$b_1\sigma^{-4}$
4.0	0.51	1.91
4.8	0.39	2.02
5.7	0.53	1.46

Table 4.3: Coefficients of the linear fit of $b_s(\rho)$ for the LD–SWF for three different values of the parameter C

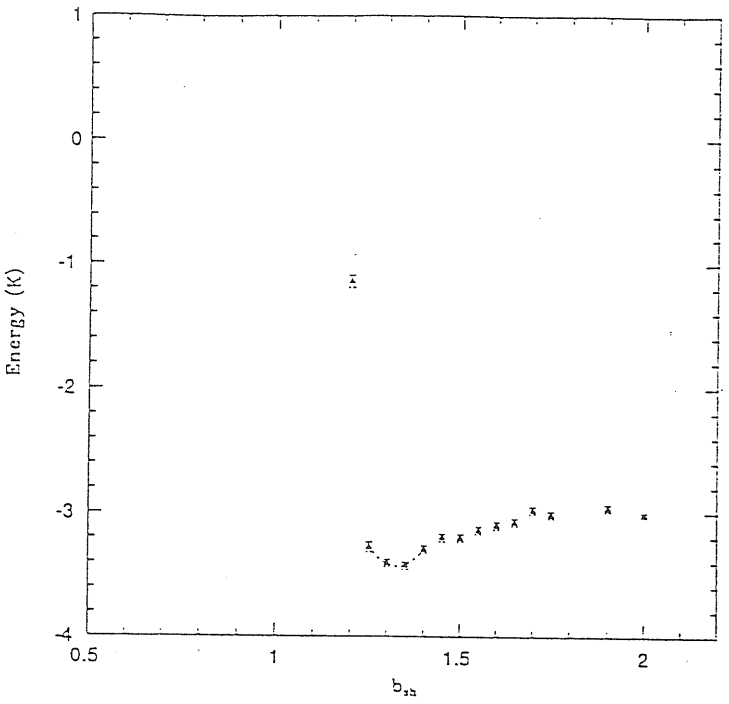

Figure 4.6: Energy as function of b_{sh} at density $\rho\sigma^3 = 0.550$ with other parameters fixed ($C = 5.7$)

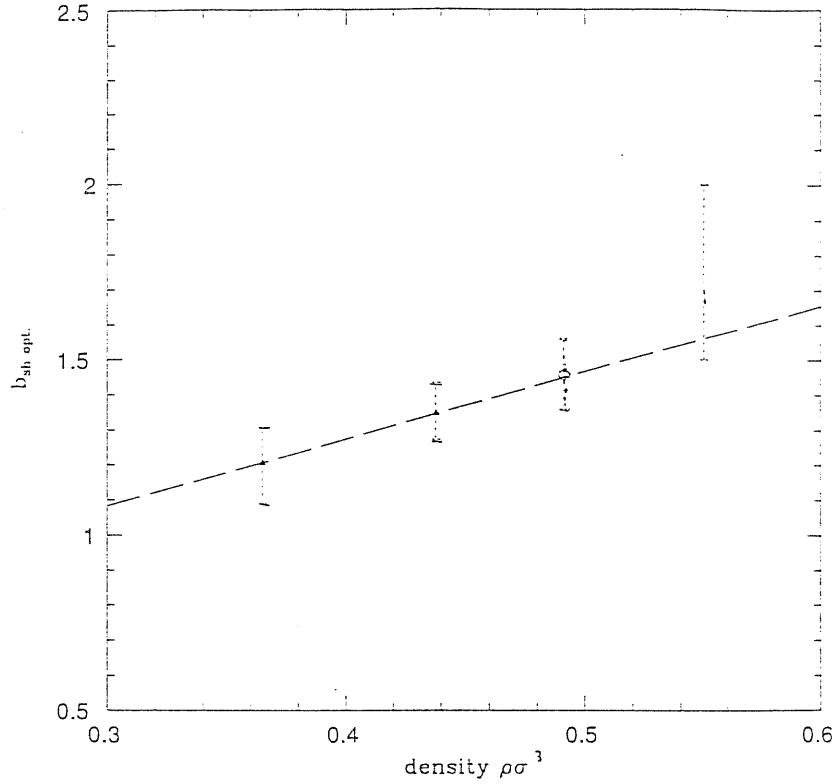

Figure 4.7: Linear interpolation of the optimal values of $b_s(\rho)$ for $C\sigma^2 = 4$

r_c	$E \pm \Delta E$	$\langle \hat{\rho}_i \rangle$	$\sigma^2(\hat{\rho}_i)$
1.80	-5.87±0.05	0.3738 ±0.0006	0.0787
2.10	-6.23±0.05	0.3671 ±0.0003	0.0379
2.60	-6.17±0.05	0.3566 ±0.0003	0.0208
3.40	-6.22±0.05	0.3637 ±0.0003	0.0172

Table 4.4: Variational energies obtained with different values of cutoff r_c at $\rho\sigma^3 = 0.365$, values of $\langle \hat{\rho}_i \rangle$ and variances relative to $\hat{\rho}_i$

4.3 Consistency of the local density operator

The local density operator $\hat{\rho}$ introduced in eq. (4.2) measures the density of shadows in a restricted region around a given one. In order to have correct results the parameters μ and r_c must be chosen in such a way that the run time average of the values of $\hat{\rho}$ gives the average density of the system. This guarantees that the average value of the parameter b_s is the optimum one at the specific density considered. In an homogeneous sample this procedure is equivalent to consider the wave function which gives the minimum of the energy. If $\langle \hat{\rho} \rangle \neq \rho$ then $\langle b_s \rangle \neq b_s^{opt}$, and the energy is higher than the variational minimum. The value of μ,which in principle should be as large as possible to guarantee the maximum of locality, has been fixed to $3\sigma^{-1}$ after some numerical exploration, the reason being that higher values make the operator too sensible to the local fluctuations, yielding too large fluctuations. Also the value of r_c should be as small as possible. A reasonable choice is to fix its value so to include in the evaluation of the local density the first shell of neighbours. In table 4.4 we report the results of some simulation with different values of r_c at the equilibrium density. It can be seen that the best values in energy coincide with the best estimates of the average densities, obtained when r_c falls

	$\rho_0\sigma^3$	$E_0(K)$	$Bi(K)$	$C(K)$
solid	0.385 ± 0.09	-5.80 ± 0.3	0.26 ± 22	29.1 ± 22.4
liquid	0.376 ± 0.007	-6.42 ± 0.07	22.4 ± 6.6	57.1 ± 29.4

Table 4.5: Coefficients of the fit of the two branches of the equation of state with the functional form of eq. (4.7).

in the minima of the pair distribution function $g(r)$. In conclusion, the dependence of the results on the parameters μ and r_c is not crucial, provided that the range of ρ_i falls between two successive shells of neighbours.

4.3.1 Equation of state

In figure 4.8 we report the equation of state obtained with LD-SWF. The behaviour resembles the gross features of the equation of state yielded by $M(R) + M^{m_s}(S)$, although the values obtained for the energy are slightly different, in particular at the melting and freezing densities. We calculated the energy also at some density values within the coexistence region, where the homogeneous phases are metastable. This can be obtained using small samples $N = 108$ particles, for which the realization of a stable phase coexistence is not possible. The two branches of the equation of state were fitted with the following formula[4]:

$$\frac{E}{N} = E_o + B\left(\frac{\rho - \rho_0}{\rho_0}\right) + C\left(\frac{\rho - \rho_0}{\rho_0}\right)^3 \tag{4.7}$$

The resulting coefficients are reported on table 4.5.

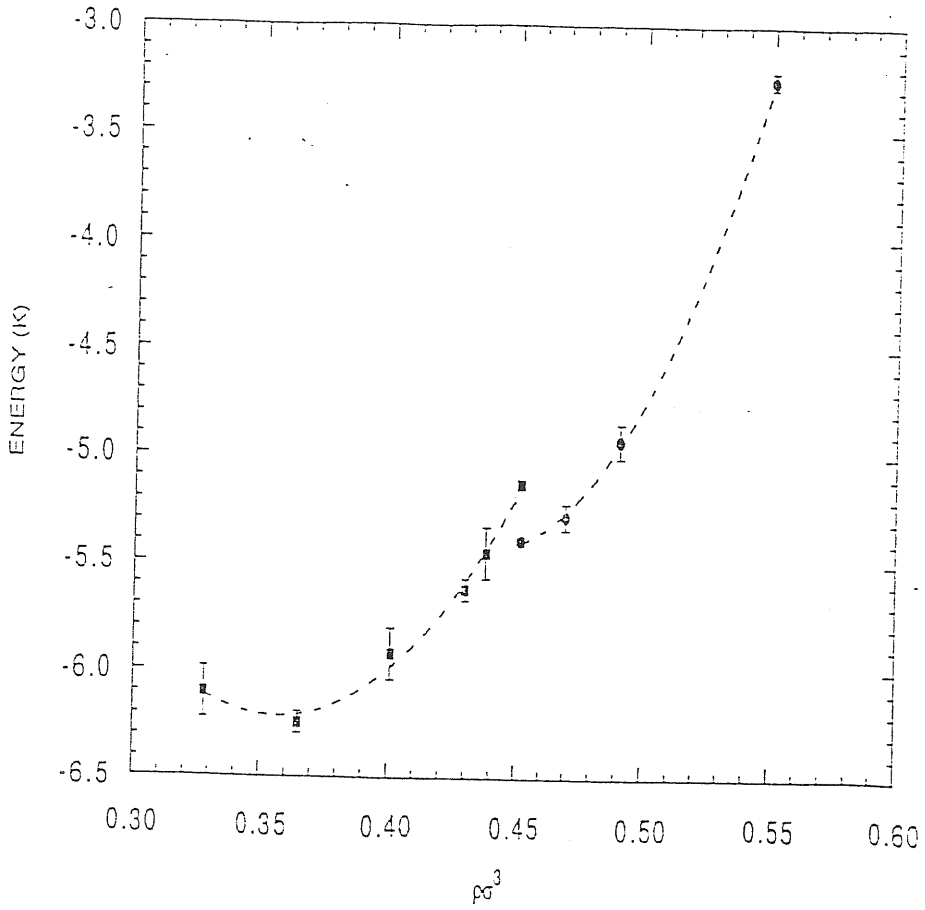

Figure 4.8: Equation of state of ^{4}He calculated with LD-SWF with the parametrization given in text. Dashed line is drawn as guide for the eye.

5 A crystallization experiment in ^{4}He

In chapter three it has been pointed out that one of the important features of the Shadow wave function is to provide a solid phase without any need of a Nosanow factor imposing *a priori* equilibrium positions. It is a recurrent problem in classical thermodynamics to know the microscopic behaviour of the particles during the fluid–solid phase transition. Several molecular dynamics and Monte Carlo simulations have been performed, in which, starting from a disordered configuration, the formation of crystalline seeds or even a complete solidification of overcooled fluids has been observed[60, 61]. Such kind of numerical simulations are were still lacking for quantum systems. Shadow Wave Functions are good candidates to try such an experiment in ^{4}He. Other variational wave functions would not be able to provide any information, because they need of a different functional form passing from the liquid to the solid. Whether SWF may give spontaneously a solid phase or not is an important question, because usually the simulations of the solid phase of ^{4}He start already from a crystalline configuration, and therefore a real homogeneous nucleation of crystals is not ensured when using SWF. Considering that the mechanism of the crystallization is based on the quasi–classical behaviour of the auxiliary degrees of freedom, and that crystallization has been observed in classical systems, one might expect

a symmetry breaking also in the shadow wave function.

5.1 The simulation

We have found spontaneous crystallization in a quantum system using SWF, in a sample of fluid ^{4}He compressed over the melting density. Simulations have been performed with LD–SWF. We are mostly concerned with this form of the wave function, because we employed it in the analysis of the solid–liquid interface.

5.1.1 Initial configurations

The simulations regards two different samples, one containing $N = 108$ ^{4}He atoms and the other with $N = 500$ atoms. The initial configuration has been obtained performing a simulation of the length of about 50000 MCS at equilibrium density ($\rho\sigma^3 = 0.365$) . All the coordinates both of particles and shadows, were then rescaled in order to fit a cubic box at a density slightly above the melting point, that is $\rho\sigma^3 = 0.500$. Periodic boundary conditions have been imposed in all directions. The use of two different sizes of the simulation boxes is due to the fact that it is believed that periodic boundary conditions may influence the formation of crystalline seeds unless the number of atoms employed is large enough (typically > 500). Moreover the effects due to the interfacial excess energy are reduced in a larger sample, because the size of the crystalline seeds that may grow in it is larger. Also statistical fluctuations increase in larger systems helping in this way the nucleation of the phase with lower symmetry. The main runs performed are four:

- 108 particles box, with SWF, starting from a fcc lattice (reference case)
- 108 particles box, with LD-SWF, starting from liquid

- 500 particles box, with LD-SWF, starting from liquid (two independent runs)

the first run has been chosen as reference, in order to compare the results for energy and also for distribution functions. The second run was done in order to look for crystallization in a small box. The last two runs have been analyzed in more detail. Two runs with a different walk have been performed in order to check whether solidification does depends on the particular walk chosen. The runs are all of the order of 2×10^5 MCS. The parameter of the LD–SWF have been chosen as follows:

$$b_p = 1.12\sigma \quad C = 4\sigma^{-2} \quad m_s = 9$$

$$b_0 = 0.51\sigma \quad b_1 = 1.91\sigma^4$$

We also performed a simulation with 108 atoms and SWF with $b_s = 1.465$, as a comparison with LD–SWF.

5.1.2 Methods for searching crystalline configurations.

An accurate analysis of the evolution of the sample is necessary in order to find out a solid structure in a sample in which the initial configuration is disordered. The major problem is that the crystalline seeds may choose random orientation within the simulation box, and this precludes any possibility of performing a run–time monitoring of the situation. It is necessary in this case to proceed *a posteriori* to analyze the configurations. The most important quantities that can give significant indications are the pair correlation function $g(r)$ and its Fourier transform, the structure factor $S(k)$. These functions are calculated as spherical averages, and do not depend on the particular orientation of the solid. Another useful procedure is the direct visualization of the configurations, that can give immediate indications about the particular structure chosen by the system. The use of other estimators that give results dependent on the choice of particular vectors of the

lattice, such as the crystalline order parameter has not been found appropriate in this kind of experiment.

5.2 Results

In all the samples that we have considered a solidification occurred, although with slightly different characteristics. This definitely confirms the capability of the LD–SWF to choose spontaneously a state of lower symmetry whenever the density is above the melting value. Nevertheless the results show that the grown solid is not oriented as expected. The growth properties do not depend either on the size of the simulation box or on the particular parametrization chosen. The variational energies found for the spontaneously grown crystal do not coincide with the results of the simulation already started from a crystalline configuration at the given density. In fact, the lattice constants that can be measured by the pair correlation functions are compatible with a crystal whose density is indeed *higher* than the initial one. Such effect is due to the fact that the crystallization is clearly favoured along a particular direction, corresponding to the {111} of the f.c.c. lattice and to the {100} of the h.c.p. lattice, rather than the {100} of f.c.c.

5.2.1 Pair correlation functions and structure factors

Fig. 5.1 shows the pair correlation functions for particles and shadows resulting from the simulations with $N = 108$ particles.

It can be seen the crystallization simulations do not coincide with the reference simulation, especially for the shadows. In the reference case $g_{ss}(r)$ for the shadows shows all the peaks proper of an fcc lattice. The real particles are much less localized, and the distribution function does not present the structures typically observed in classical solids.

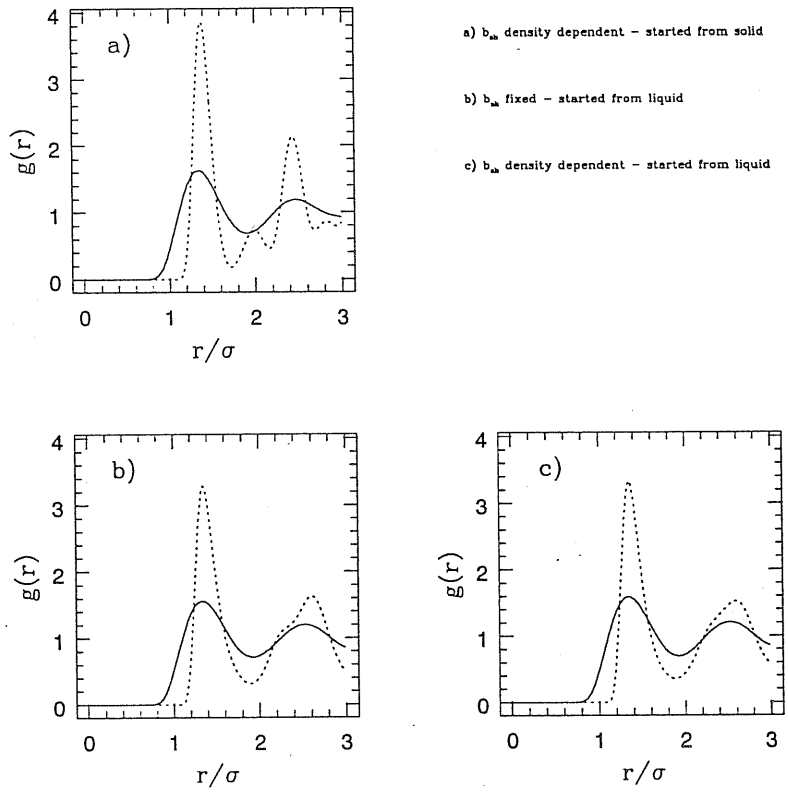

Figure 5.1: Pair correlation function for particles (solid lines) and shadows (dashed lines):

a) SWF, started from an f.c.c. lattice

b) SWF, started from fluid

c) LD–SWF, started from fluid

The simulations started from the liquid configurations give a $g_{ss}(r)$ that presents a nearest neighbours peak that is about 15% lower than in the reference case. Nevertheless its height is still typical of a crystalline phase. The structure of the subsequent peak is not very well determined, although it is possible to observe a clear shoulder at distance 2.3σ that is the sign of the presence of a structure in the configurations. The pair correlation functions of the particles do not differ in shape very much in both cases. LD–SWF and SWF give roughly the same results.

In figure 5.2 we show $g(r)$ and $g_{ss}(r)$ at the very beginning of the run, when the system is still fluid, and at the end, in the case of the density independent correlation. Evolution in the sense of an ordering appears very clearly.

The pair correlation functions obtained in two of the runs with 500 particles lead to different results. In one case the features of the two main peaks closely resemble the results obtained with 108 particles (see fig. 5.3), with is the second peak blurred out and without the presence of neighbour peaks. In the second case (see fig. 5.4) $g(r)$ presents the gross features of the a perfect f.c.c. crystal.

5.2.2 Configurations

The direct visualization of the configuration generated in the random walk is very important in order to understand more deeply the structural features of the crystal grown in the simulation box. From the correlation functions it can be seen that the ordering properties are made more evident when we look at the shadow degrees of freedom rather than to the real particles. The results are similar for all the runs considered. From a visualization of the configurations it is also possible to follow the pseudo–evolution of the sample, observing the progressive growth of the crystalline seeds. There are several ways to study the configurations. The most suggestive consists in using some 3–D visualization

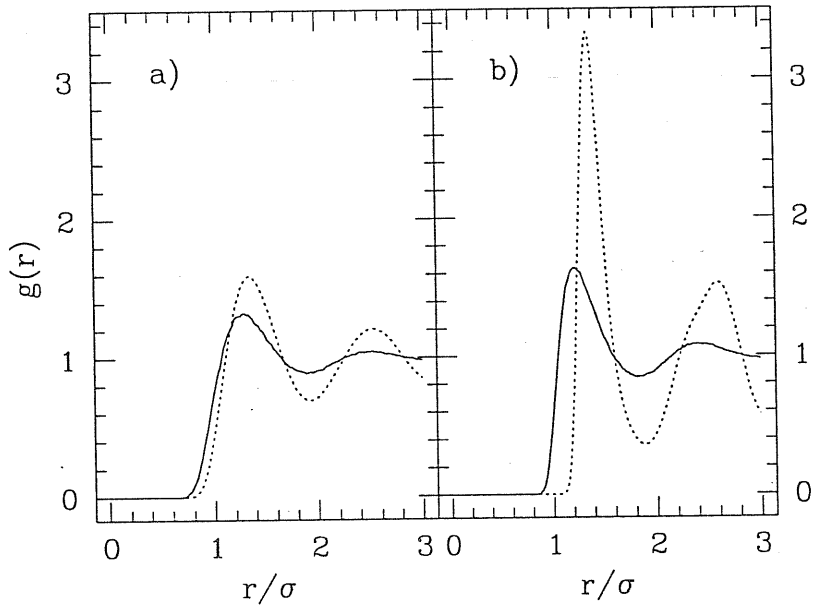

Figure 5.2: Pair correlation function for a) particles and b) shadows at the beginning of the run (solid line) and after 200000 MCS (dashed line), for N=108 particles.

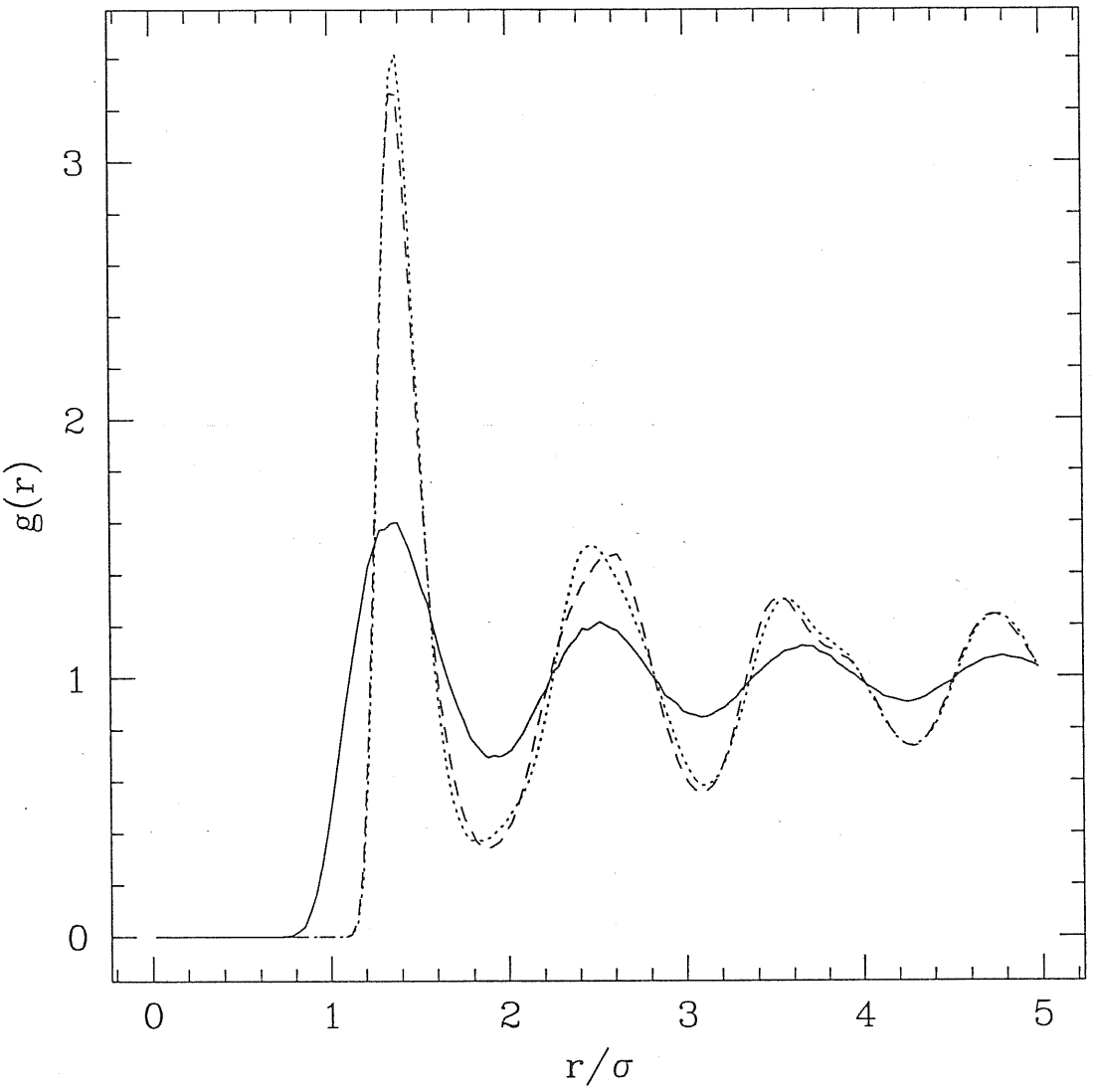

Figure 5.3: Pair correlation function for $N = 500$ particles in a LD–SWF simulation. Solid line: helium atoms; dashed line: shadows after 80000 MCS; dotted line: shadows after 200000 MCS.

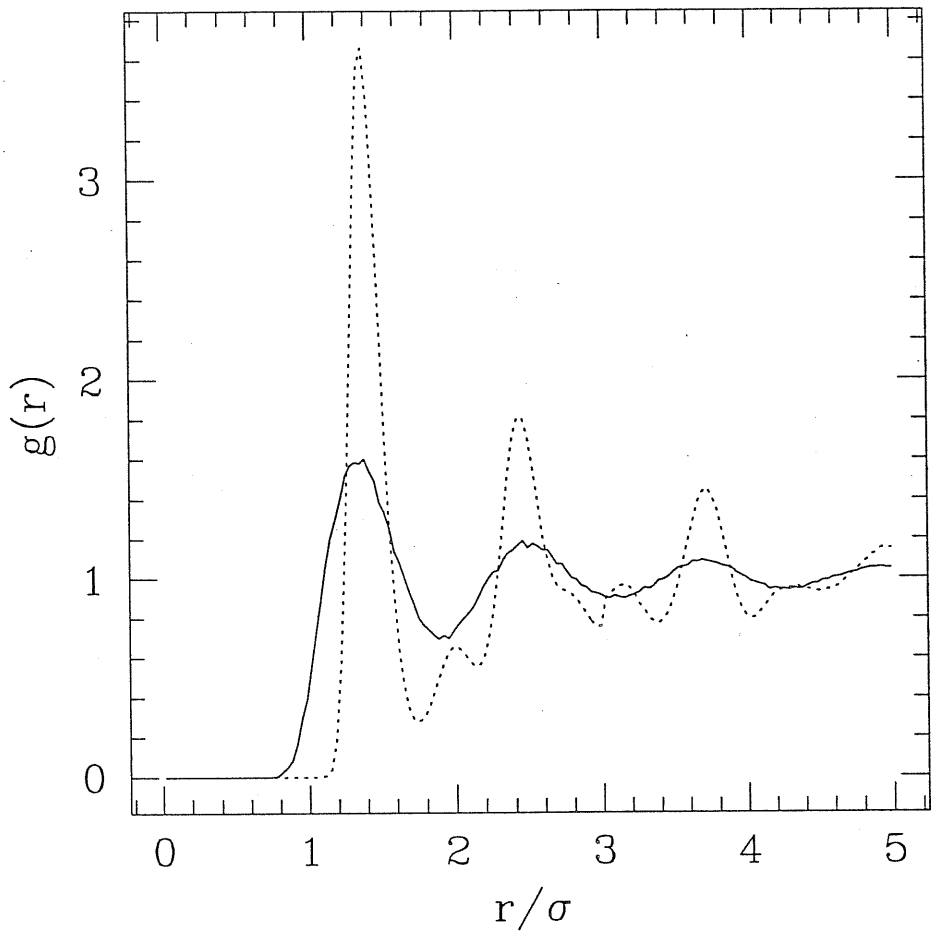

Figure 5.4: Pair correlation function for $N = 500$ particles in a LD–SWF simulation. Solid line: helium atoms; dashed line: shadows. This run differs from that of fig. 5.3 in the generated random walk.

package realizing a movie with the successive configurations. The results reported below are all referred to the simulations with 500 particles. Another way is to plot projections of the coordinates on a chosen plane (commonly one of the faces of the simulation box). In fig. 5.5 we can see the projections of the coordinates in the $x - z$ and in the $x - y$ planes after about 80000 MCS.

The sample in this case is still not completely crystallized. This is particularly clear in the $x - z$ projection, where we can distinguish three different regions, one on the top with planes oriented with an angle of $\pi/4$ with respect to the axes, one in the middle where the shadows are already localized, but the structure is not well defined yet, and one in the bottom, where the orientation of the planes looks to be parallel to the z axis. Also in the $x - y$ projection it can be noticed that the orientation of the layers is not well defined, even if we can distinguish portions where the planes are ordered. This indicates that in the box the crystal growth does not begin from a unique seed, but rather from several seeds, differently oriented. Thus we can think to the motion of the particles as splitted in two different motions: one, with larger frequency, around the mean value of the position at the time t, and a second one, slower, tending to adjust the positions of the atom in the appropriate crystalline configuration. This more complex situation is reflected in the acceptance rate of the trial moves for the shadows, that was gradually lowering, for the same step width, from 30% to 20%.

Going on with the simulation we observe that one of the seeds prevails on the others. In figures 5.6 to 5.8 we report the projections on the faces of the simulation box of configurations generated after about 200000 MCS. It can be seen that the situation is different from that of the previous figures. In particular the $y - z$ projection presents a well defined layering, with 9 planes not parallel to the $x - y$ plane. The spacing between the layers is larger than the expected one. In fig. 5.9 we show the same projection after a rotation

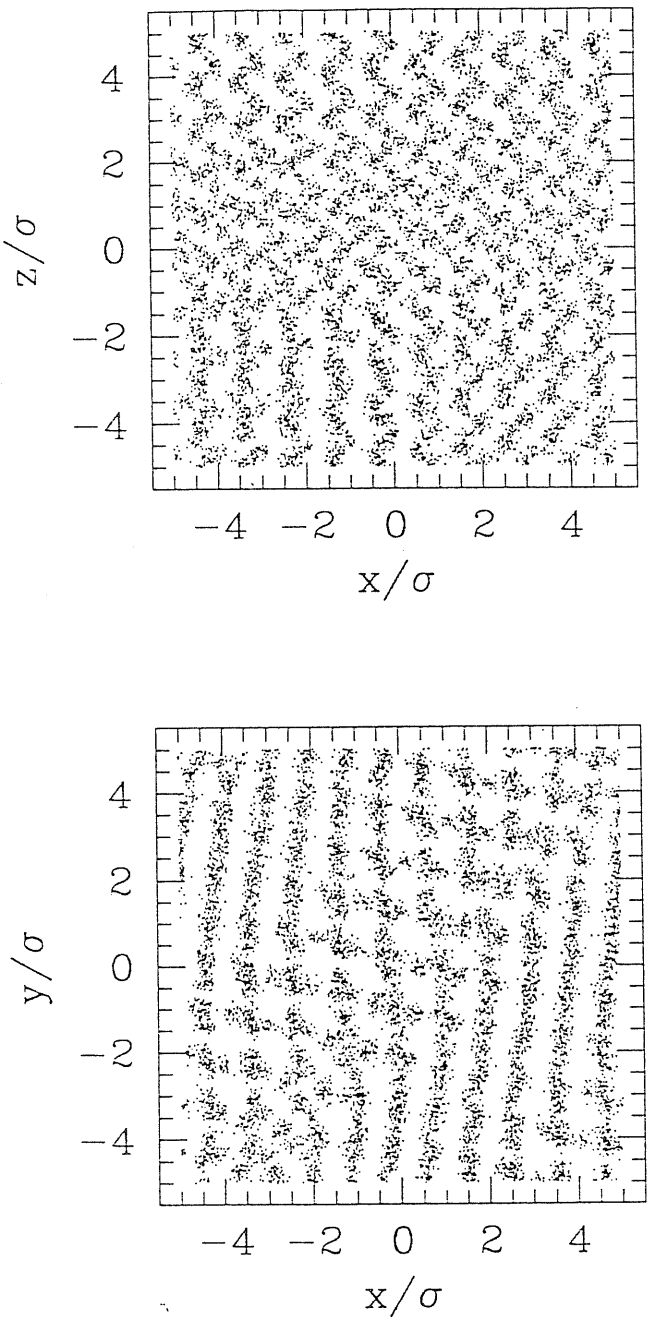

Figure 5.5: Projection of 40 configuration taken from 1000 after $\equiv$ 80000 MCS. Top: $x - z$ projection; bottom: $x - y$ projection

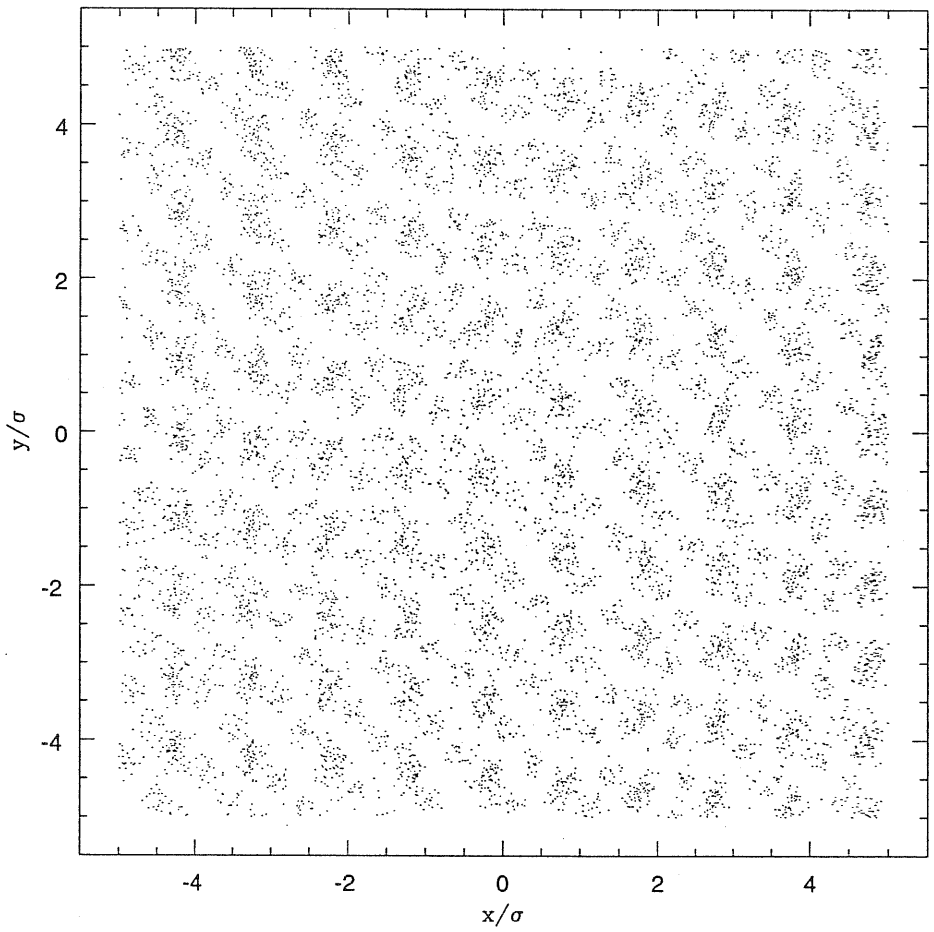

Figure 5.6: $x - y$ projection of the shadow configurations after 200000 MCS

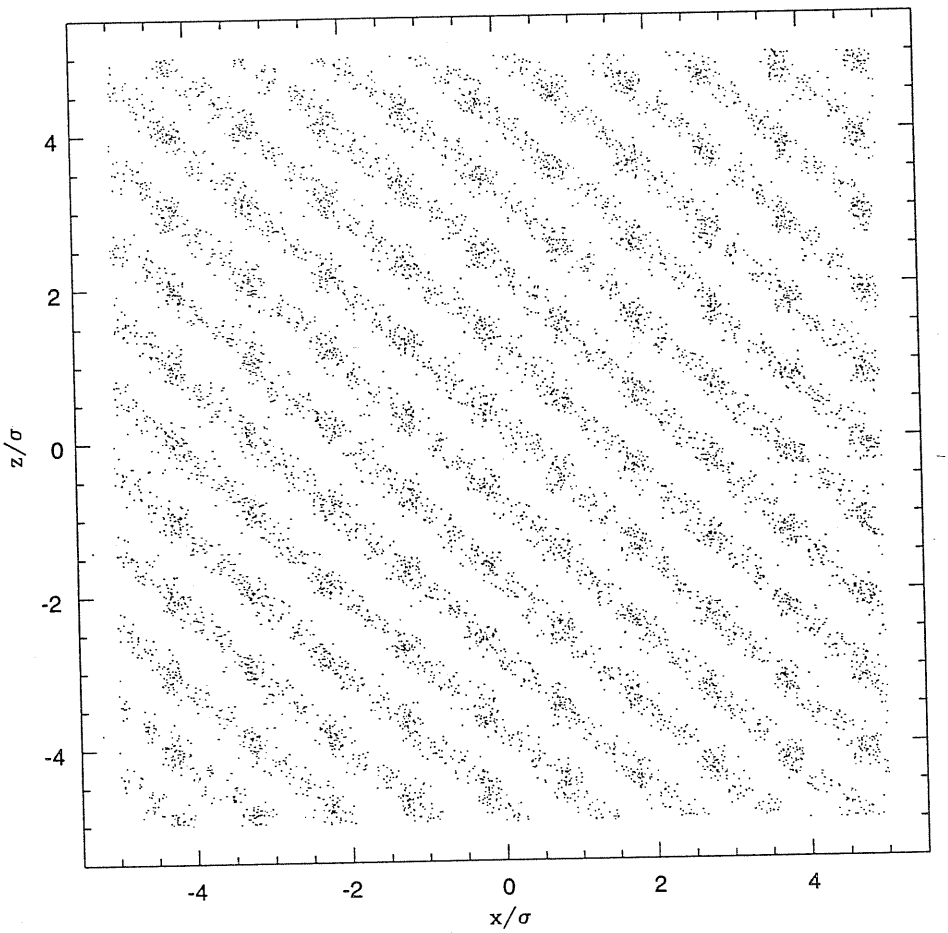

Figure 5.7: $x - z$ projection of the shadow configurations after 200000 MCS

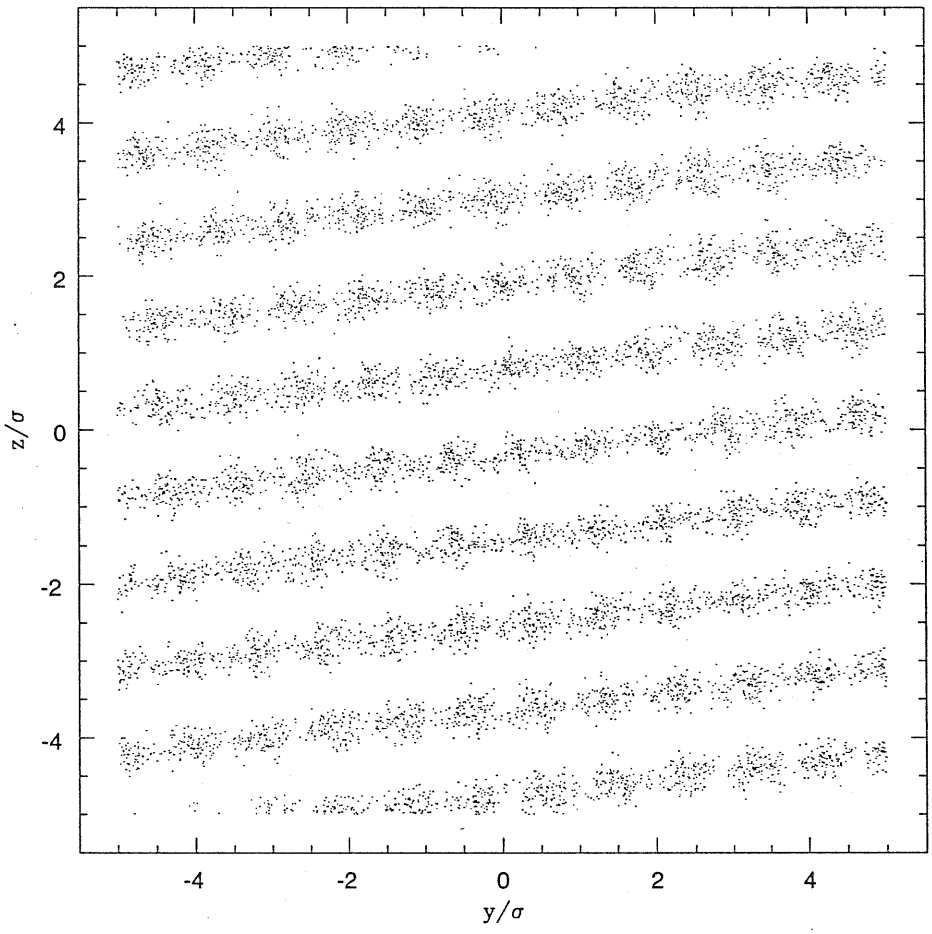

Figure 5.8: $y - z$ projection of the shadow configurations after 200000 MCS

of the configuration around the x axis of an angle $\pi/16$. In fig. 5.10 the projection on the $x-y$ plane is displayed after the rotation. From the figures it becomes evident the formation of a close–packing ordering: the winning seed is that growing along the {111} direction of a f.c.c. lattice, or equivalently along the {100} direction of an h.c.p. lattice. From the angle and the distance we can estimate the lattice constant of the solid. The interlayer spacing is:

$$\delta = \frac{10\sigma}{9}\cos\left(\frac{\pi}{16}\right) = 1.1329\sigma, \tag{5.1}$$

and the lattice constant is given by:

$$a = \delta\sqrt{3} = 1.9622\sigma, \tag{5.2}$$

that is smaller than the value initially chosen for the density $0.5\sigma^{-3}$. The growth crystal has therefore an effective higher density. Its value is given by

$$\rho = \frac{4}{a^3} = 0.529\sigma^{-3}. \tag{5.3}$$

This value can be checked also from the positions of the peaks in the pair distribution functions, that we have seen to be shifted with respect to the reference case. The values obtained are consistent with the estimates given above.

The pair correlation functions in figures 5.4 and 5.3 show that the final packing in the two runs performed with $N = 500$ particles is different. In one case there is a pure f.c.c. structure, layered along the close– packing direction. For the second case we have plotted the configurations of a single $x-y$ plane. The structure is evidently distorted. for each single plane (see fig. 5.11).

Looking at the succession of the planes it is possible to distinguish regions where the ordering is that of the f.c.c. lattice, and others where the h.c.p. is prevailing. We can measure again the lattice constant from the distances between the shadows in the

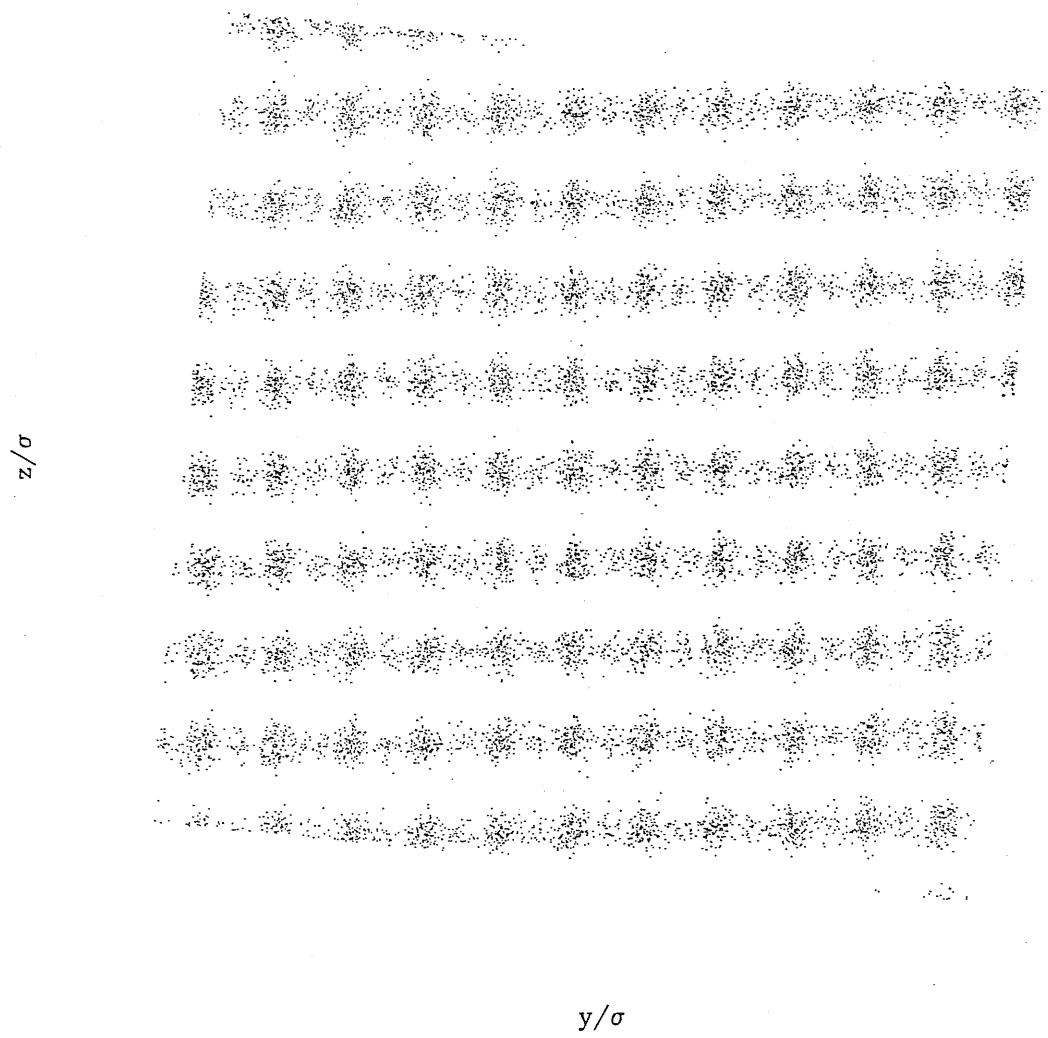

Figure 5.9: $y - z$ projection of the shadow configurations after 200000 MCS and after a rotation of $\pi/16$ around the x axis

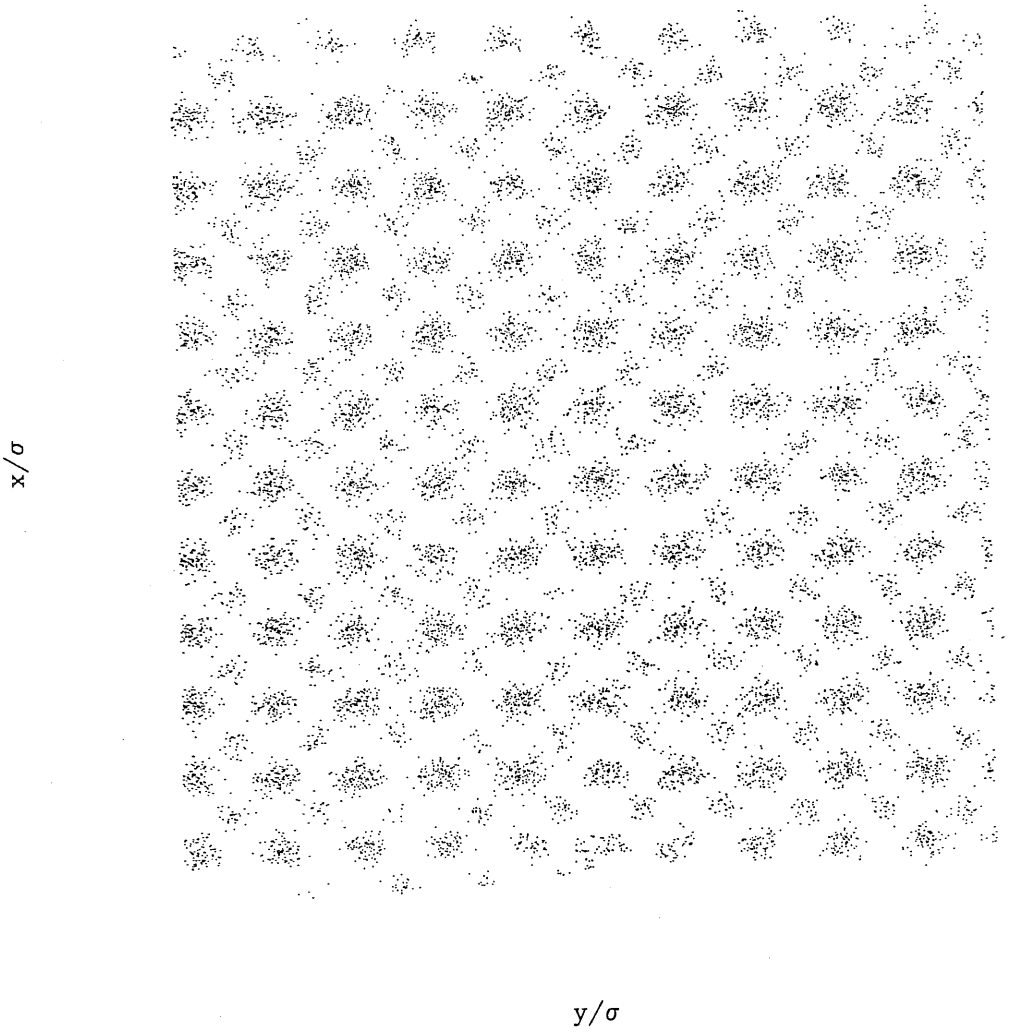

Figure 5.10: $x - y$ projection of the shadow configurations after 200000 MCS and after a rotation of $\pi/16$ around the x axis

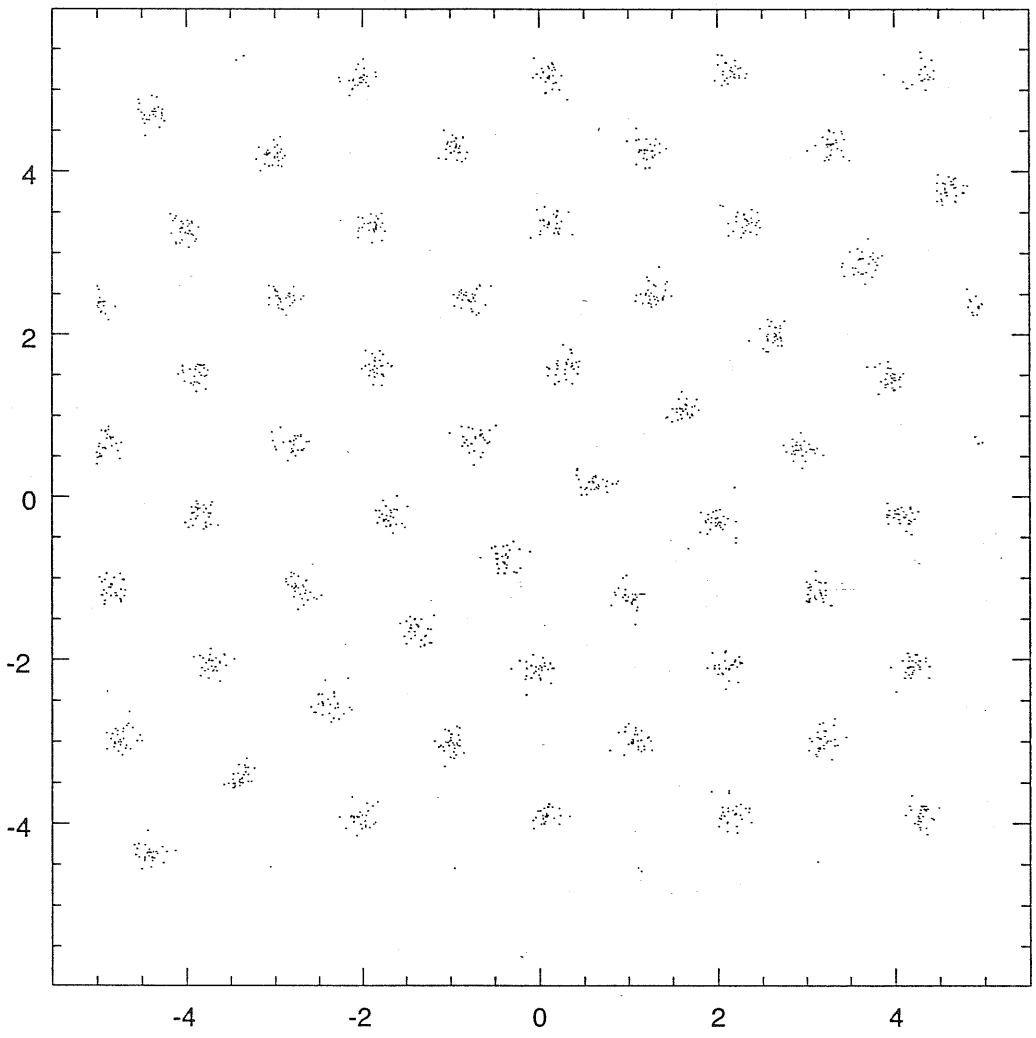

Figure 5.11: Shadow configurations on a single {111} plane.

N	Ψ	Initial conf.	$\epsilon(K)$	$E_{kin}(K)/N$	$E_{pot}(K)/N$	MCS
108	SWF	solid	-4.82 ± 0.01	26.47 ± 0.03	-31.30 ± 0.03	5×10^4
108	SWF	fluid	-4.26 ± 0.01	26.43 ± 0.03	-29.37 ± 0.02	2×10^5
108	LD-SWF	fluid	-4.09 ± 0.01	25.27 ± 0.03	-30.71 ± 0.02	2×10^5
500	LD-SWF	fluid	-4.23 ± 0.01	26.30 ± 0.03	-30.54 ± 0.02	2×10^5
500	LD-SWF	fluid	-4.33 ± 0.01	26.32 ± 0.03	-30.65 ± 0.01	3×10^5

Table 5.1: Variational energies, potential and kinetic energies per particle in the crystallization runs.

planes. An average of the nearest neighbours distances gives a lattice constant $a = 1.96$, compatible with that obtained from the spacing between the planes. An useful check of this results can be done calculating the pair correlation function in the $x - y$ plane:

$$g_{xy}(r) = \frac{1}{N\rho} \sum_{i \neq j} \langle \delta(\sqrt{(x_i - x_j - x)^2 + (y_i - y_j - y)^2} | \rangle .$$

The result is reported in fig. 5.12. The positions of the peaks reflect the expected ordering. Nevertheless we can observe that the peak at the distance the second neighbours is blurred out. In particular we can observe a spurious peak at distance $r = 2.1\sigma$. This comes from the distorted triangles observed in fig. 5.11 in the upper left and lower right corners.

5.2.3 Variational energies

In table 5.1 we report the variational energies obtained in our runs, together with potential and kinetic energies. The main feature that can be observed is that in all the cases considered there is a difference of $\sim 0.5 - 0.6K$ between the energy of the reference case and the other results. In the previous section we observed that the structure of the crystal corresponds to a lattice constant associated with a density of $\rho\sigma^3 = 0.53$. From the fit of

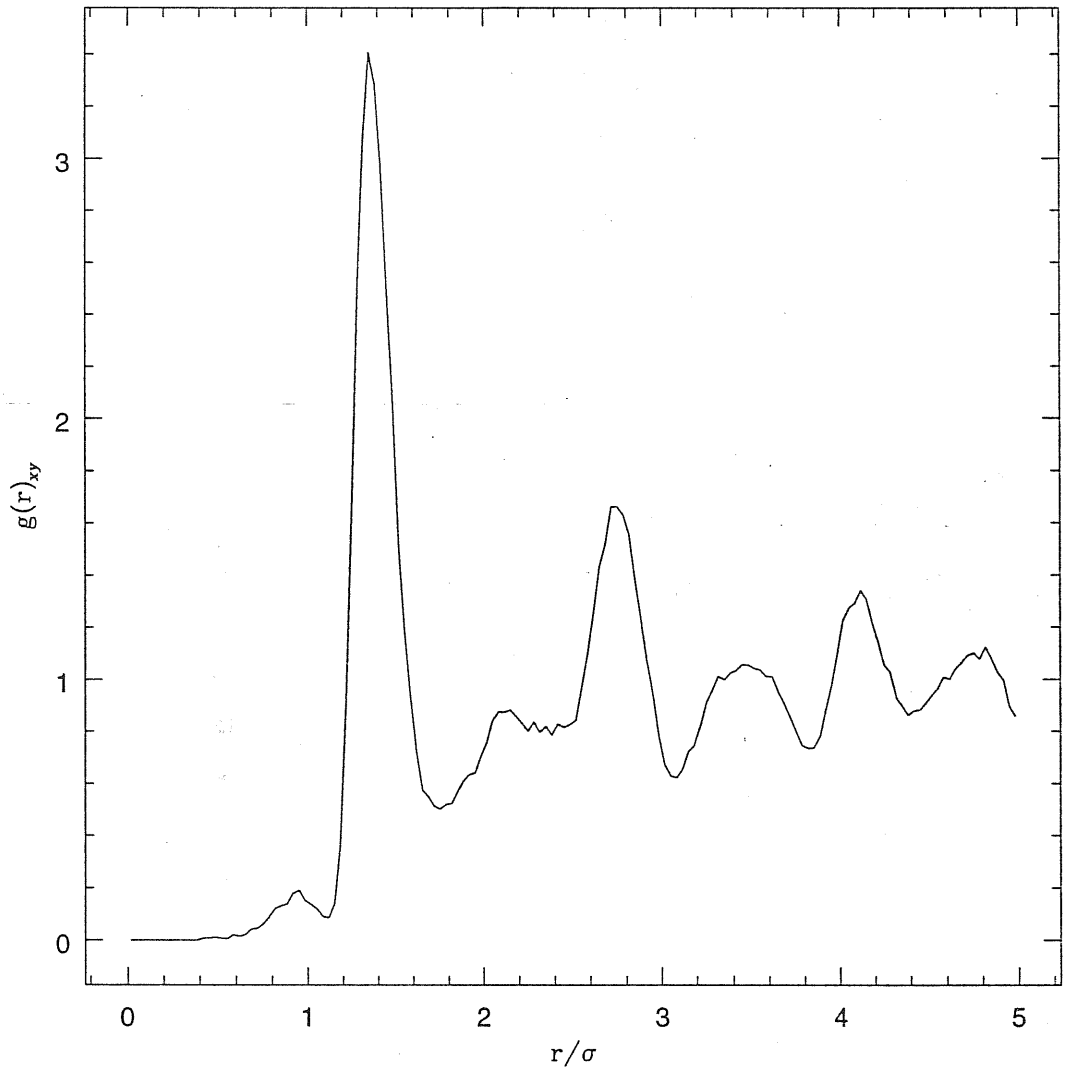

Figure 5.12: $g_{xy}(r)$ for shadows after 200000 MCS in a $N = 500$ simulation box

the equation of state of the LD-SWF the energy corresponding to such density is $-4.15K$, consistently with the results obtained. It is interesting also to observe the evolution of the variational energy along the run. In fig. 5.13 we plotted the results for in one of our simulations. It can be observed that the variational energy starts from a quite lower value, then tends to increase. In this phase of the simulation in the box interfaces between the solid and the liquid are present. The excess energy introduced is reflected in the rising of the energy per particle. After this barrier is overcome, the variational energy begins to lower again, reaching soon a nearly constant value. This is a further indication that the situation reached by the system is an actual equilibrium state.

5.3 Comments

This crystallization experiment gives two main results. First of all it is definitely confirmed that the Shadow Wave Function can provide a spontaneous symmetry breaking from the liquid to the solid phase. The stable crystalline phase is not an artifact of the initial conditions, and also the solidification does not depend on the presence of an already existent seed. Secondly there is a strong indication that the growing process is favoured along the $\{111\}$ direction, even if this leads to a state that is incommensurate to the simulation box. More quantitative studies on this important feature are under consideration at present.

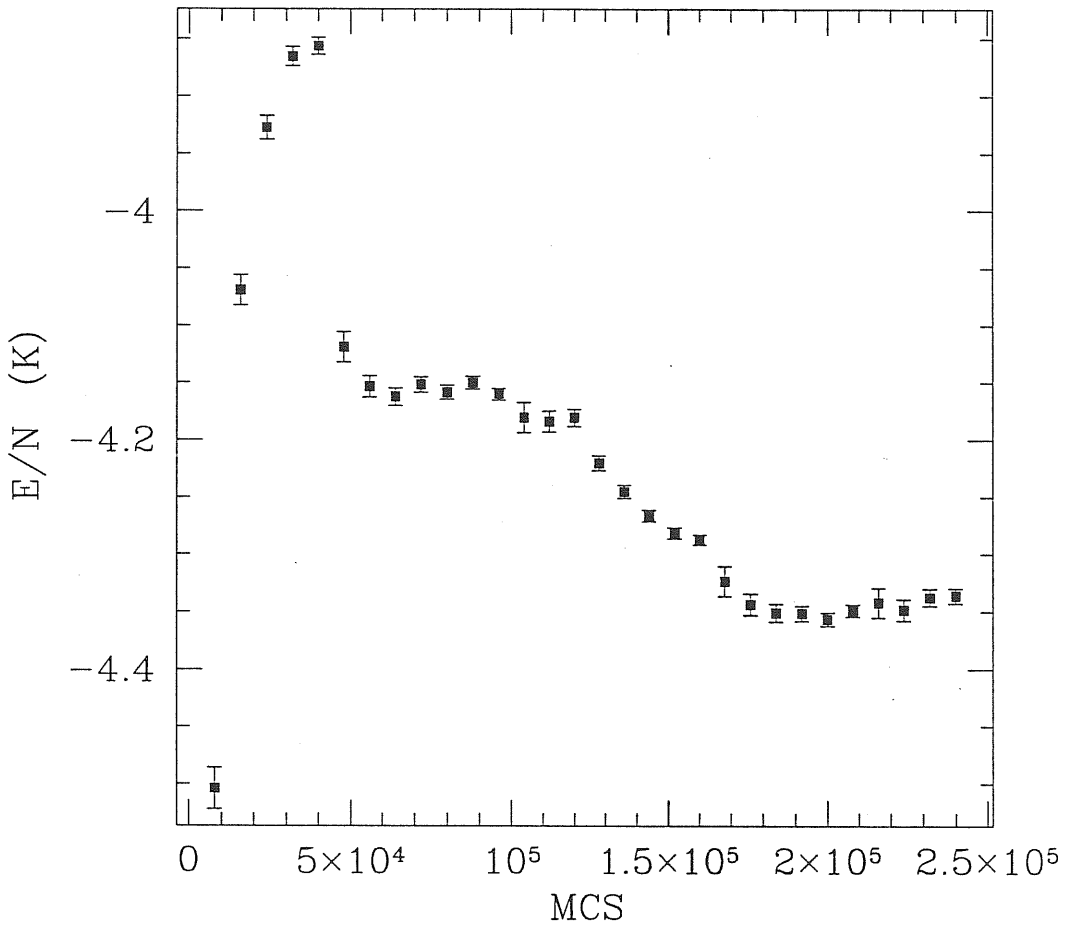

Figure 5.13: Variational energy per particle as a function of the number of MCS performed in a $N = 500$ particles box.

6 Solid–Liquid coexistence and interface in ^{4}He

In the previous chapters we described how it is possible to build up a variational theory that is capable of describing with a unique trial wave function the whole equation of state of ^{4}He within the Shadow Wave Function formalism. We have also verified that SWF nucleates spontaneously a crystal in a metastable fluid, confirming that at high densities the solid phase is indeed stable. We are therefore ready for our most important step, the description of an inhomogeneous system, that is the branch of the equation of state in which we have solid– liquid phase coexistence. We will report here on the calculations performed employing a McMillan density dependent form as shadow–shadow correlation pseudopotential.

6.1 The solid–fluid coexistence

We want to summarize rapidly some general properties of the solid–liquid coexistence[62]. The coexistence of phases 1 and 2 occurs when the following conditions are realized:

$$T_1 = T_2 \quad P_1 = P_2 \quad \mu_1 = \mu_2 \tag{6.1}$$

where P is the pressure and μ the chemical potential. Let us consider a system of N_1 particles in the phase 1 with specific volume v_1 and N_2 particles in the phase 2 with specific volume v_2, at fixed temperature T and under the constraint that $N_1 + N_2 = N$. The total Helmoltz free energy $F = U - TS$ is given by

$$F = N_1 F_1(N_1, V_1) + N_2 F_2(N_2, V_2). \tag{6.2}$$

An additional constraint (equivalent to the Maxwell construction) is the so called " lever rule ", that requires also the conservation of the specific volume:

$$\frac{N_1}{N} v_1 + \frac{N_2}{N} v_2 = v \tag{6.3}$$

The constrained minimization of F in eq. (6.2) with respect to $N_1, N2, v_1$ and v_2 gives back the conditions of eq. (6.1), showing that describing the phase coexistence as a mixture of two components, in a proportion such to minimize the free energy, is consistent with physical conditions. In the limit $v \to v_1$ all the system is on the phase 1 and the value of F is that corresponding to that point. When v increases F is given by the Maxwell construction, that is by the tangent common to the two branches of F(N,V) relative to phases 1 and 2. This construction can be rigorously justified in the frame of statistical mechanics, and represents a simple way to find out coexistence regions, once that the Helmoltz free energy is known. In the case of solid–liquid coexistence v_l^{-1} is referred as *freezing density* and v_s^{-1} as *melting density.*

The Maxwell construction has been widely applied in classical calculations for many different systems, such as hard and soft spheres[48] or Lennard–Jones systems[49]. We can find in the literature many simulations of solid–fluid coexistence, both with Monte Carlo[30] and Molecular Dynamics[31] techniques.

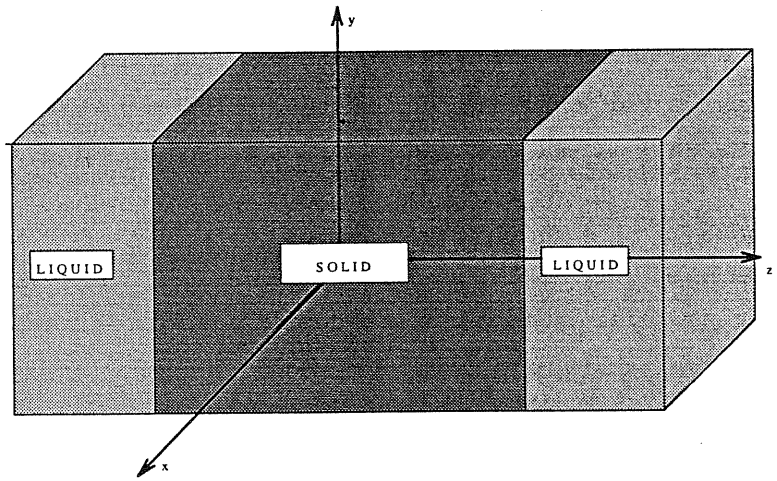

Figure 6.1: Simulation box for the interface

6.2 Simulation procedures and estimators

6.2.1 Simulation box

The simulation of a phase coexistence requires a number of particles which is much larger than that usually adopted in simulation of homogeneous systems. In order to avoid finite size effects, it is necessary to have a quite large number of particles in the bulk phases. Moreover the interface has an intrinsic width, that in the case of solid–liquid coexistence in helium is expected to be $5 - 7$ Å wide, about five times the interlayer spacing. The area of the surface should not be too small to avoid the strong influence of the periodic boundary conditions[61]. MD simulations for classical systems have been done with 6×10^5 particles[31]. In the quantum case such numbers are computationally unaccessible. In our simulations N ranges from $N = 1800$ up to $N = 4400$. A picture of the initial configuration is shown in fig. 6.1.

It consists of M layers of solid, built up along the $\{100\}$ or along the $\{111\}$ direction.

In the first case the $x-y$ section of the box is a square of side $4a$ where a is the side of the conventional elementary cubic cell for fcc. In the second case the section is rectangular, with x side equal to $12.72a$ and y side equal to $14.70a$. Aside we put a volume of liquid (that at the beginning is set up as random configuration), in accordance with the desired average density and the initial density of the liquid. The box is closed with periodic boundary conditions in all directions. The effective geometry is therefore that of a torus in which a part of solid and a part of liquid are present.

6.2.2 Computational procedures

Technical aspects

The large numbers of particles involved in the calculation requires the use of sophisticated techniques for the implementation of the Metropolis algorithm. In particular we used the linked lists (LL) method[63], in order to have a linear growth of the CPU time with the number of particles. The details of this technique are sketched in Appendix B. LL exploits the short range of the correlations to save computer time. If the size of the simulation box is smaller than the range of the correlations and potentials considered, whenever a particle is moved, only a fraction of the atoms is involved in the computation of changes in $|\Psi|^2$, therefore the time that is really needed become proportional to N and not to N^2. In our case the correlations are not very short ranged. Nevertheless the use of truncated forms of the inverse power correlations in boxes containing $N = 108$ particles gives already excellent results, justifying the adoption of such procedure.

Equilibration and development of the simulation

In the simulation of a phase coexistence, correlation times in the MC calculations tend to become very large[64]. This implies that the length of the simulations must be increased.

The major problem arises from the relaxation of the initial configuration towards the equilibrium state. Because the melting and the freezing densities are not known a priori, we might start form a situation that is quite far away from the final one. A typical simulation has been organized as follows:

- Starting from the initial configuration few tens of MCS are needed to eliminate the peculiar numbers due to the random configuration set of the liquid

- A first phase of equilibration is done, during which it is necessary to accumulate the estimators for relatively short periods (typically 10000 MCS) in order to follow the relaxation of the profiles.

- After the stabilization of profiles the real accumulation of statistics may start. The typical time of relaxation is around 50000 MCS, but it depends strongly on how far the initial conditions are from equilibrium.

6.2.3 Estimators for interfacial diagnostic

The particular nature of the system under investigation requires various kind of estimators. which are suggested by earlier classical simulations[30, 31]. They are all organized in the form of profiles, obtained dividing the box in slides that are orthogonal to the direction along which the density varies, which is the z axis. The estimators are then evaluated in each slide. This procedure is very important in order to get informations about the local properties of the system.

Crystalline Order Parameters

A crystalline order parameter is defined by:

$$O_l^{\mathbf{G}} = |\langle \frac{1}{N_l} \sum_{i=1}^{N_l} e^{i\mathbf{G}\cdot\mathbf{r}_i} \rangle|^2 \tag{6.4}$$

where $\mathbf{G}$ is a vector in the reciprocal lattice of the initial crystalline structure, l is the layer index, and N_l is the number of particles present in the l-th layer, and $\langle\rangle$ indicates the average on the configurations generated in the random walk.

The crystalline order parameter is one when the particles sit exactly on the sites of the lattice, and zero on average in the case of a disordered phase. In real solids at finite temperature its value is much lower than one, due to the displacement of the atoms around the equilibrium positions.

For this estimator the layering is based on the spacing between the crystal planes orthogonal to the z direction. Therefore, in the case of the $\{100\}$ interface the width Δz of the layer is equal to $a/2$, where a is the elementary cubic cell side, while in the case of the $\{111\}$ interface the binwidth is $a\sqrt{3}/2$. The vectors $\mathbf{G}$ determine the direction along which the monitoring of the order is done. In the case of the interface the common procedure is to monitor separately the order in the lattice planes orthogonal to z direction (*transverse order parameter*), and the order along such direction (*longitudinal order parameter*), that is connected with the spacing of the layers. Of course different sets of $\mathbf{G}$ vectors are needed, whether we consider the $\{100\}$ or the $\{111\}$ interface. For the $\{100\}$ case a possible choice for the $\mathbf{G}$ is:

$$\mathbf{G}_x^{\perp} = \frac{4\pi}{a}(1,0,0) \quad \mathbf{G}_y^{\perp} = \frac{4\pi}{a}(0,1,0)$$

$$\mathbf{G}^{\parallel} = \frac{4\pi}{a}(0,0,1)$$

The transverse order parameter is obtained averaging $\mathbf{G}_x^{\perp}$ and $\mathbf{G}_y^{\perp}$, while the longitudinal

order parameter is given by $\mathbf{G}^{\parallel}$. For the $\{111\}$ case one can take the following vectors:

$$\mathbf{G}^{\perp} = \frac{2\sqrt{2}\pi}{a}(1, -\frac{1}{\sqrt{3}}, \sqrt{6})$$

$$\mathbf{G}^{\parallel} = \frac{2\sqrt{2}\pi}{a}(0, 0, \sqrt{\frac{3}{2}})$$

These order parameters are estimated both on the particle and on the shadows configurations.

Density profiles

The local density of the system is monitored using the density profiles. A density profile is defined as:

$$\rho(z) = \langle \frac{N(z)}{S\Delta z} \rangle, \tag{6.5}$$

where $N(z)$ is the number of particles with z coordinate lying between z and $z + \Delta z$, S is the area of the $x - y$ section of the simulation box, and Δz is the width of the bin. It is customary to accumulate density profiles based on different binnings. A coarser binning, based for instance on the spacing between the crystalline planes, as it is done for the order parameter, provides a density profile that is smooth in the solid, and allows to view the decay of the density in the interfacial region. A density profile based on a finer binning, allows for a closer view of the single planes in the solid, that therefore appear as sharp peaks, while in the liquid it has a nearly constant value. In this case a binwidth of about 0.08σ has been adopted. Also these estimators are accumulated both for particles and shadows.

Energy profiles

Another class of profiles is based on the evaluation of the energy per particle profile. Due to the form of the hamiltonian, we can adopt a convenient representation in which the

local energy $\hat{H}\Psi/\Psi$ is splitted in the contributions relative to each single particle:

$$\frac{\hat{H}\Psi}{\Psi} = \sum_{i=1}^{N} E_i, \tag{6.6}$$

where:

$$E_i = -\frac{\hbar}{2m}\frac{\nabla_i^2\Psi}{\Psi} + \frac{1}{2}\sum_{j\neq i} v(r_{ij}), \tag{6.7}$$

where v is the potential energy. The energy per particle profile is defined as:

$$\epsilon_l = \langle \frac{1}{N_l}\sum_{i=1}^{N_l} E_i \rangle, \tag{6.8}$$

where l is the bin index, and N_l are the particles contained in it. Note that the expression of the energy in a specific layer does not involve only the particles present in that layer, but includes the contributions due to the interaction with all the particles. In the same way it is possible to define the profile of the potential energy per particle, and of the kinetic energy per particle, which are quantities of major physical interest. Strictly connected to the evaluation of the local energies are the calculations of the pressure and of the diagonal part of the stress tensor. The pressure is the derivative of the energy with respect to the specific volume:

$$\mathcal{P} = -\frac{\partial E}{\partial v} = \frac{1}{\rho^2}\frac{\partial E(\rho)}{\partial \rho}.$$

Derivatives with respect to changes of volume in given directions give the components of the pressure tensor $\mathcal{P}_{\alpha\beta}$. The stress can be easily evaluated from the diagonal components:

$$S = \mathcal{P}_{zz} - \frac{1}{2}[\mathcal{P}_{xx} + \mathcal{P}_{yy}]$$

An estimate of these quantities can be obtained scaling the coordinates of both particles and shadows and evaluating in the rescaled configuration the energy profiles, in order to

calculate the numeric derivative of the energy profile with respect to the volume. For instance, the profile of the zz component of the pressure tensor is given by:

$$\mathcal{P}^l_{zz} = \frac{\epsilon^+_l - \epsilon^-_l}{\Delta v},$$

where ϵ^+_l is the energy profile calculated in the system when the z coordinates are expanded to $z(1+\alpha)$, and analogously ϵ^-_l is calculated with the z coordinates transformed in $z(1-\alpha)$. $\Delta v = 2\alpha A \Delta z / N_l$, where A is the area of the xy section of the simulation box, Δz is the with of the bin, and N_l is the number of particles in each bin, gives the variation of the specific volume. Similarly it is possible to calculate $\mathcal{P}^l_{xx}$ and $\mathcal{P}^l_{yy}$, and consequently the stress profile.

6.3 Results

6.3.1 Simulations performed

The first problem we have faced with was that the effective coexistence region does not coincide with that determined by the Maxwell construction on the equation of state, for which the coexistence region lies between $\rho\sigma^3 = 0.420$ and $\rho\sigma^3 = 0.490$. Choosing densities around $\rho\sigma^3 = 0.450$ a complete crystallization of the sample is found. A stable phase coexistence has been found for values of the density between $\rho\sigma^3_f = 0.449$ and $\rho\sigma^3_m = 0.456$. Within this range we performed simulations at four different densities:

- $\rho\sigma^3 = 0.4505$;
- $\rho\sigma^3 = 0.452$;
- $\rho\sigma^3 = 0.454$;
- $\rho\sigma^3 = 0.4557$.

$\rho\sigma^3$	MCS	# of solid layers along z	% solid	% liquid	N	orientation
0.4505	2×10^5	30	50%	50%	1876	{100}
0.4520	1×10^5	30	50%	50%	4272	{111}
0.4520	2.5×10^5	30	50%	50%	18642	{100}
0.4540	7×10^4	30	50%	50%	1902	{100}
0.4557	2×10^5	20	33%	66%	1896	{100}

Table 6.1: Summary of the MCS and of the initial configurations for the main runs performed in the coexistence region. N is the number of atoms in the sample. The number of variables is 9N.

In table 6.1 we report the initial configurations of the main runs.

6.3.2 Energies and equation of state

In chapter 4 we proved that when simulating an homogeneous phase, the LD-SWF provides results which are not significantly different from those of SWF. We can now complete the equation of state with the points that we have found in the coexistence region. In table 6.2 we report the total energies, potential and kinetic energies for each of the densities considered. In all cases $\rho\sigma^3 = 0.452$ there is no significative difference for the {100} and the {111} orientations.

One can see in fig. 6.2, that the energy in the coexistence region is a decreasing function of the density. This is a direct consequence of the $M(R) + M^9(S)$ model considered for the SWF. Interpolating the equation of state obtained with such wave function at the effective freezing and melting densities ($\rho_f = 0.449\sigma^{-3}$ and $\rho_m = 0.456\sigma^{-3}$ respectively), one obtains:

$$E(\rho_f) = -5.16K \quad E(\rho_m) = -5.43K.$$

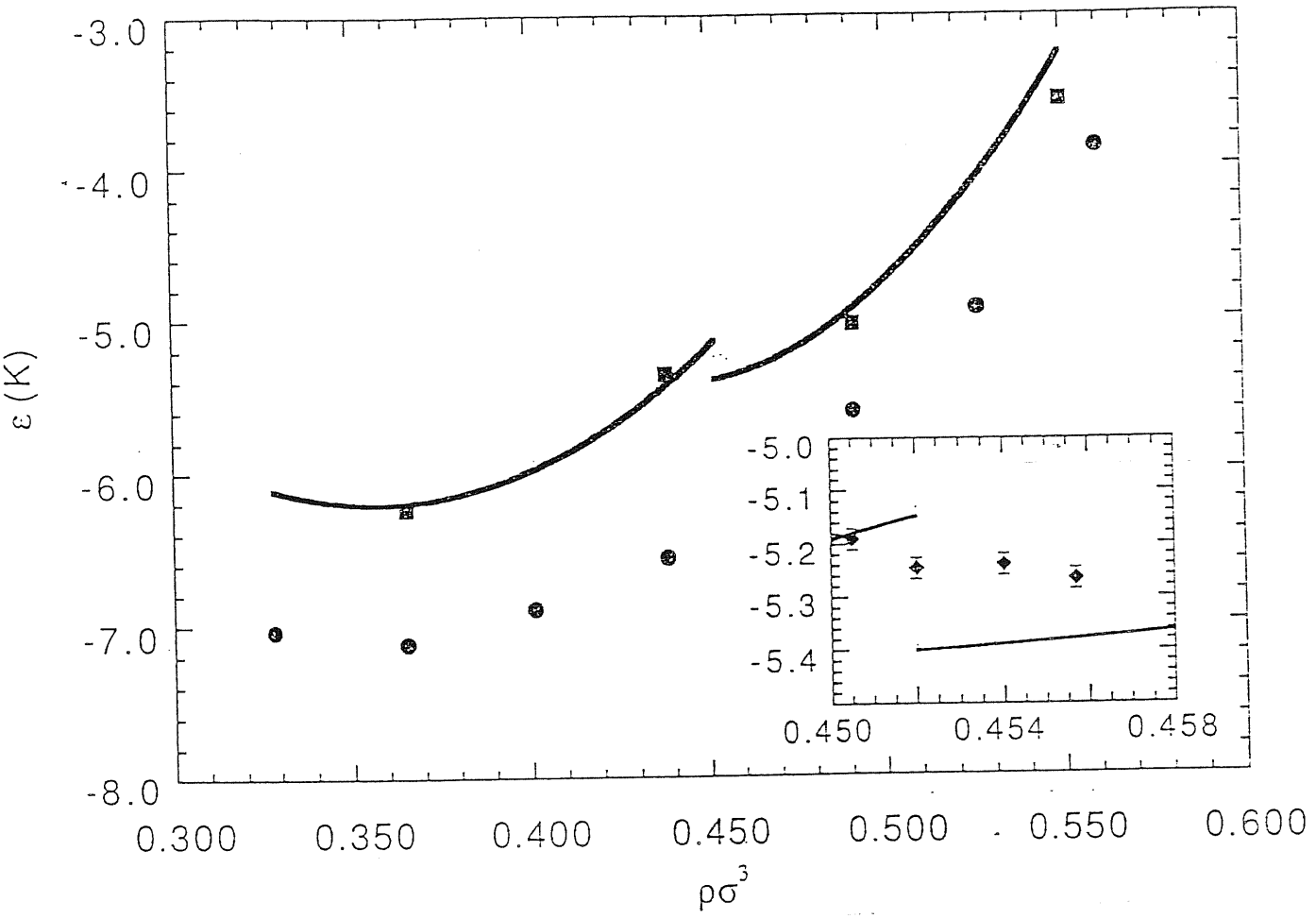

Figure 6.2: Equation of state of ^4He obtained with LD-SWF. The coexistence region is reported in the insert, and the points represent the results of table 6.2.

$\rho\sigma^3$	$\epsilon \pm \Delta\epsilon$	$V \pm \Delta V$	$T_{PB} \pm \Delta T_{PB}$
0.4505	-5.19 ± 0.02	-26.60 ± 0.04	21.41 ± 0.04
0.4520	-5.22 ± 0.02	-27.24 ± 0.04	22.03 ± 0.04
0.4520	-5.214 ± 0.005*	-27.25 ± 0.01	22.03 ± 0.01
0.4540	-5.23 ± 0.05	-27.26 ± 0.07	22.01 ± 0.07
0.4557	-5.26 ± 0.02	-26.60 ± 0.04	22.77 ± 0.04

Table 6.2: Total energy per particle (in Kelvin), potential and kinetic energy per particle in the coexistence region.

**relative to the* $\{111\}$ *orientation with 4272 particles*

6.3.3 Profiles analysis

Most of the informations regarding the physics at the solid– liquid interface may be deduced analyzing the informations given by the various profiles that are produced during the runs. We illustrate in the following the results concerning the runs at density $\rho\sigma^3 = 0.452$, comparing them with the results at the other densities considered.

Order parameters

Typical order parameter profile are shown in fig. 6.3. The order parameters for the particles and for the shadows coincide in the liquid, while assume different values in the solid phase. Shadows are much more localized than the particles. As a consequence, higher values for the order parameter are found for the shadows than for the particle. The order parameter for the shadows assume values which are typical of classical solids. The region in which the values decays to zero signals the presence of layers in which the disorder takes place of the crystalline structure, and can be defined as the interface. The

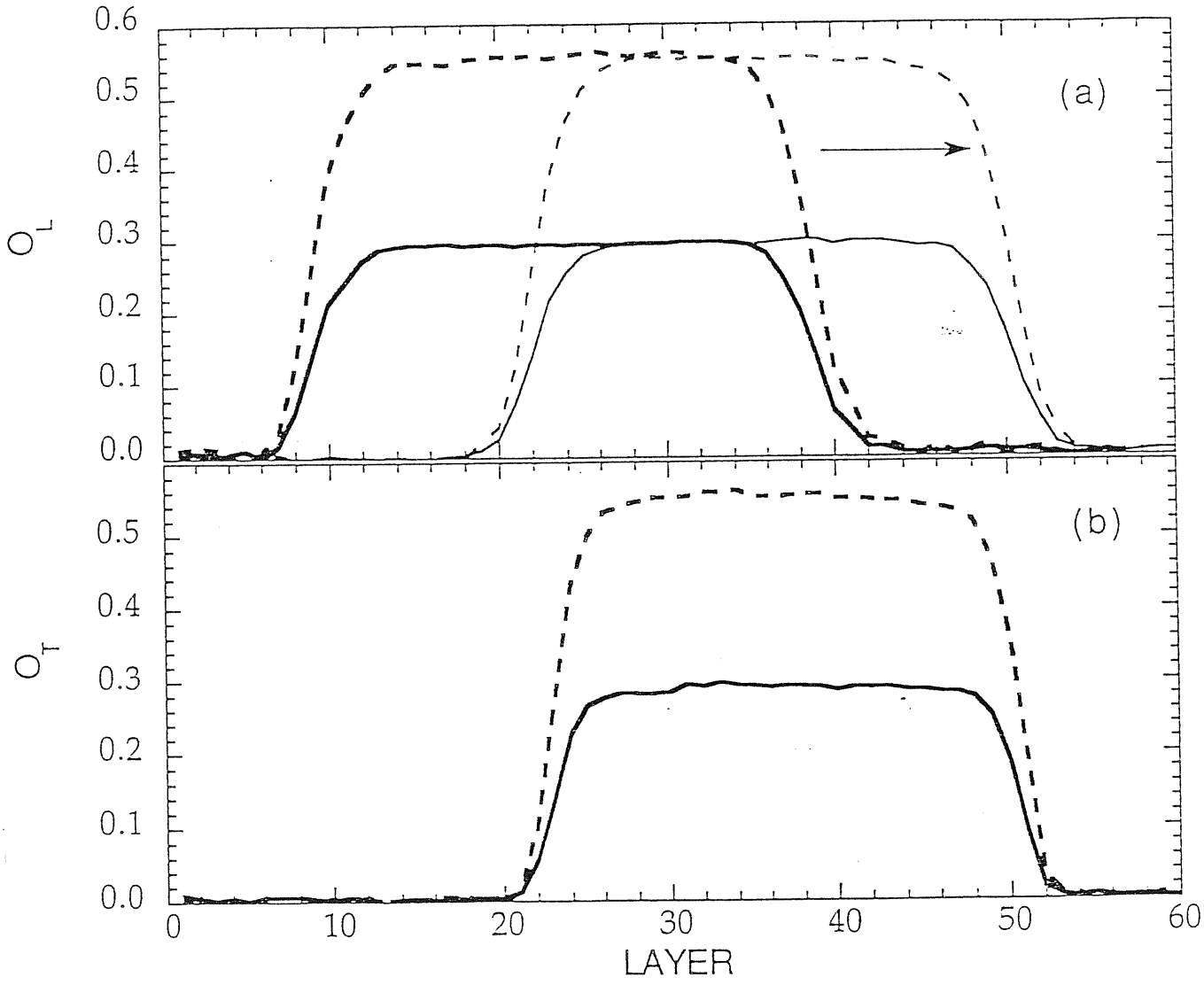

Figure 6.3: Longitudinal (a) and transverse (b) order parameter profile for the {100} interface at density $\rho\sigma^3 = 0.452$. Solid line: particles, dashed line: shadows. In (a) the two sets of curves refer to different block averages in the simulation.

transverse order parameter results to be steeper than the longitudinal one. This is due to the fact that the first liquid layers are no more ordered in the transverse direction, while a modulation of the distance in the direction of the density variation may persist. In fig. 6.4 the longitudinal and the transverse order parameter for the {111} interface are shown. The profiles have the same behaviour in the proximity of the interface.

In figure 6.3-(a) two different sets of profiles are plotted. They refer to different block averages in the simulation, distanced of about 40000 MCS. The figure displays clearly that the solid experiences a wide motion throughout the box. This phenomenon is peculiar of our simulations, and it has never been noticed before in classical simulations. and it is not due to spurious motions of the center of mass, that are corrected in the simulation. Examining the configurations it is possible to observe that *the layers in the middle of the box contain always the same particles, that do not drift from the original positions.* This means that the interface is moving through a process of melting and reconstruction of the layers. This resembles the mechanism proposed by Andreev[65] to explain the dynamics of the melting–freezing waves in ^{4}He. [1] The driving force for this motion could be originated by the fact that the initial conditions are far from the equilibrium. The fact that in the {111} interface, where we started with densities closer to the values found in the simulations the motion is very depressed supports this interpretation. Additional care must be taken in calculating the width of the interface because its motion tends to blur out the profiles. This can be avoided taking partial averages on reduced samples. In fig. 6.5 it is shown the order parameter as it appeared if averaged over all the configurations generated in the random walk. The interfacial region is completely blurred out, and the determination of the quantity of solid resent becomes impossible.

[1] Melting–freezing waves have been widely observed experimentally [66], and are strictly connected with the roughening properties of the crystalline surface [67].

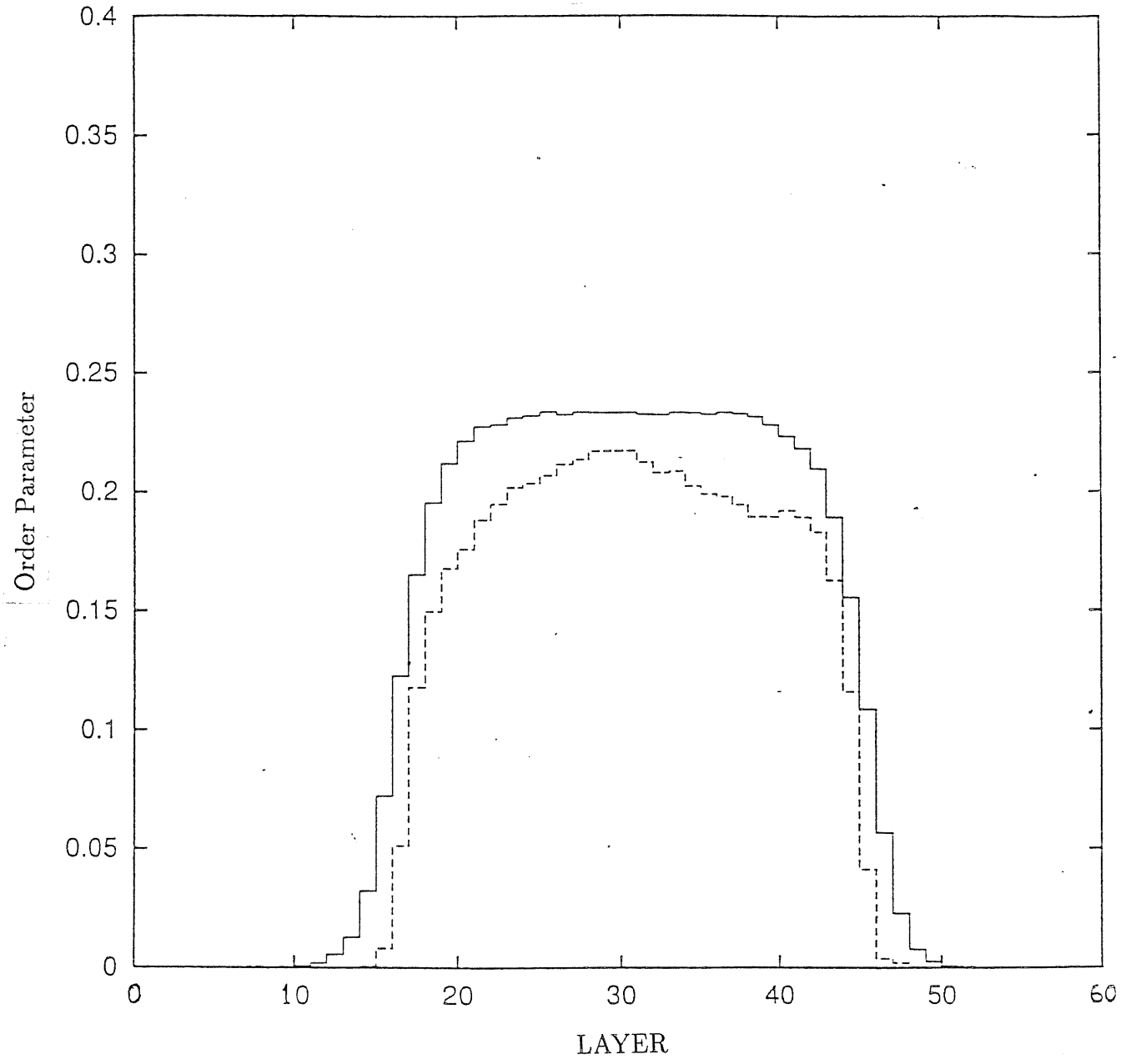

Figure 6.4: Longitudinal (solid line) and transverse (dotted line) order parameter profiles for particles in the {111} interface at density $\rho\sigma^3 = 0.452$

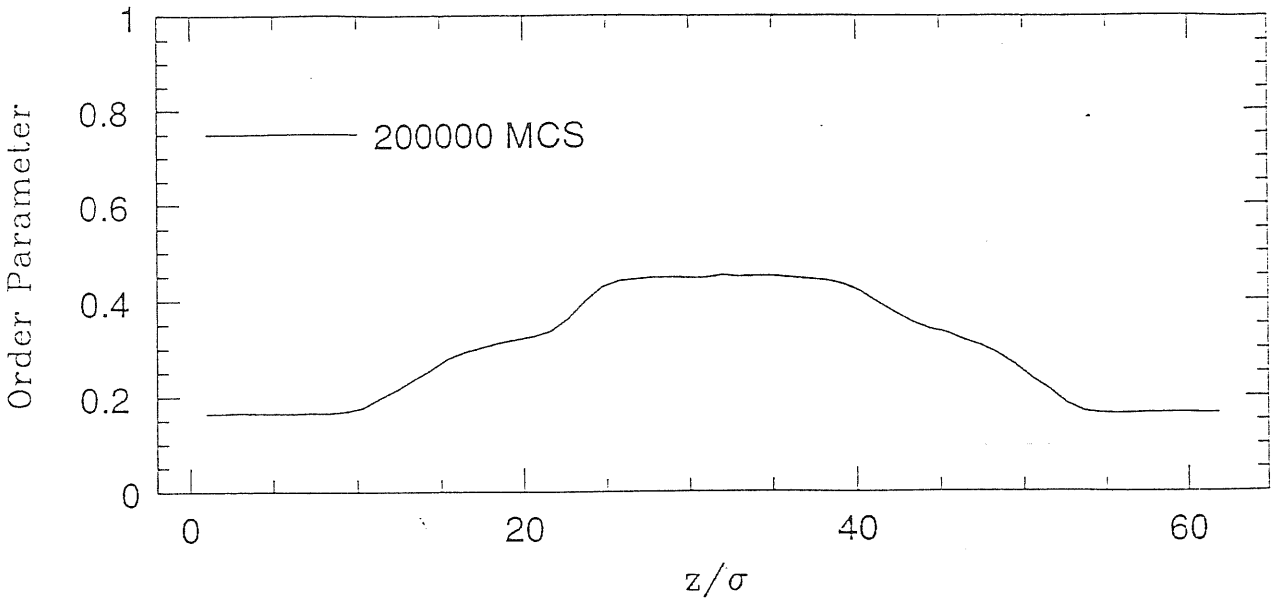

Figure 6.5: Average of the order parameter profiles over 200000 MCS. The interfacial profile is blurred out by the motion of the solid

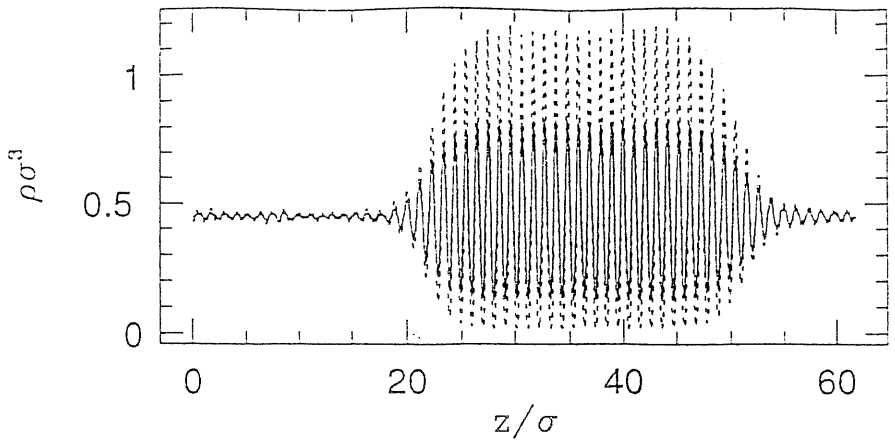

Figure 6.6: Fine scale density profile for the {100} interface at density $\rho\sigma^3 = 0.452$. Full line: particles, dashed line: shadows.

An alternative strategy to reduce the noise due to the motion of the interface consists in correcting the positions with respect to the center of mass of the solid defined as:

$$z_{CM}^{solid} = \frac{\sum_l \frac{1}{N_l} \sum_{i=1}^{N_l} z_i O_l^{\perp}}{\sum_l O_l^{\perp}}$$

z_{CM} should be determined in a self consistent way, starting from an estimate of the order parameter profile.

Density profiles

The fine scale density profile shows very well the different structure of the liquid and of the solid (see fig 6.6). Deep inside the liquid it assumes a fairly constant value, with fluctuations within the variance of the estimator that decrease with the number of MCS performed. This indicates the absence of strong modulations along the z axis. Here the behaviour is the same both for the particles and for the shadows. In the bulk solid a series

of peaks may be observed, each corresponding to a layer in the solid. The shape of these peaks is roughly gaussian, and their width is connected to the average displacement of the particles around the crystalline sites. Here the shadows and the particles give different profiles. The peaks for the shadows are quite narrow, and the height is comparable to that obtained in simulation of classical system[30, 31]. The profile for the particles is different, and shows broader peaks overlapping at the basis, indicating that there is a finite probability for atoms of one layer to visit the nearest layers. This is not connected to the exchange probability that results to be nearly zero also in this case. The width of the peaks depends in part on the variational parameter C that controls the relative displacement of particles and shadows. We adopt a value for C that is lower than the optimal one for the solid phase ($C = 5.7$), and this contributes to enlarge the peaks of the real particles. In the interfacial region the peaks present in the solid decay progressively toward the constant value, according to what is indicated by the order parameter. The decay of the amplitude of the oscillations in the liquid is quite slow, indicating that the disordered phase is strongly modulated approaching the solid. The layer based density profile (fig 6.7) is a quantity that in the solid is very sensitive to the changes in the lattice spacing, because the interference between the periodicity of the binning and the periodicity of the crystal gives rise to wide spurious oscillations. In the figure we report the profiles in the case of the {100} interface. The bulk densities are not affected on the orientation. Where the disordered phase begins a lowering of the density appears of the order of $0.05\sigma^{-3}$, that is the 1% of the freezing density and is of the same order of the gap between the freezing and the melting densities. This feature does not depend neither on the interface considered nor on the particular characteristics of the simulation as the initial conditions or the movement of the solid. Such behaviour is observed also in classical simulations[68], and means that the liquid tends not to wet its solid surface.

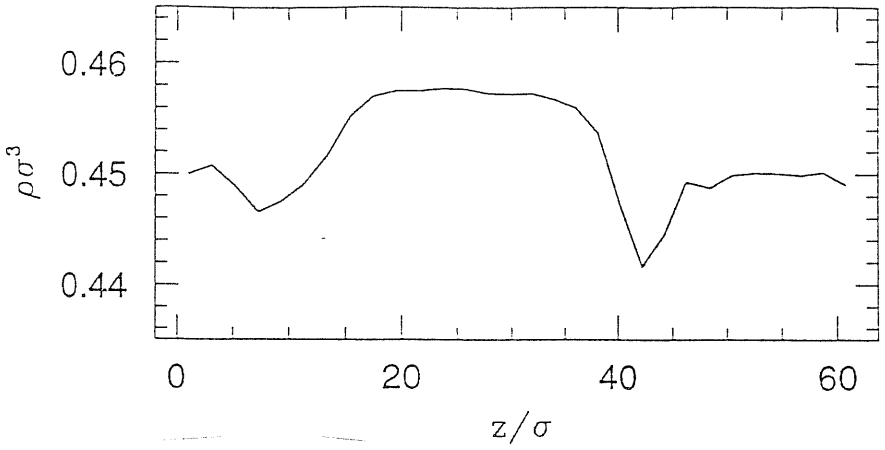

Figure 6.7: Per layer density profile, for particles, for a {100} interface at density $\rho\sigma^3 = 0.452$. Each bin has width equal to the distance between successive crystalline planes.

This minimum in the density profile was claimed to be at the origin of localization of ^{3}He impurities at the solid–liquid interface of ^{4}He[69]. From the analysis of the density profiles we can extract with good precision the values of the critical densities. Estimation of the freezing density is straightforward, and can be obtained both from the fine scale and the coarser scale profiles. In the fluid the density fluctuations in a given point tend to average quite rapidly with a large enough number of MCS, and the value obtained is fairly constant in all the bins. More difficult is to estimate the melting density. We adopted two methods, both based on the fine scale density profile. One consists in measuring directly the distance among two consecutive peaks in the solid, obtaining in such a way an estimate of the lattice constant. Alternatively we calculate the Fourier transform of the profile, in which appears clearly the peak correspondent to the periodicity in the solid (see fig. 6.8). The results, compared with the extension of the coexistence region expected from the Maxwell construction, the results of GFMC and the experiment, are reported in table 6.3.

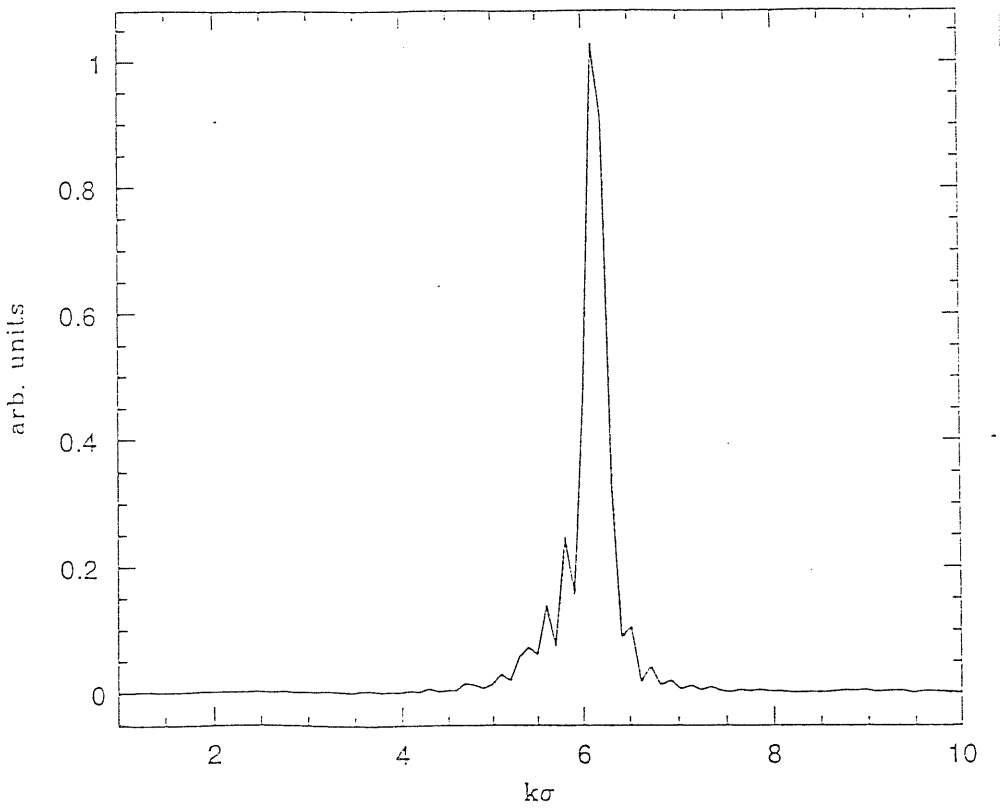

Figure 6.8: Fourier transform of the fine scale density profile in fig 6.6. The peak corresponds to the periodicity of the solid

	$\rho_f\sigma^3$	$\rho_m\sigma^3$
LD-SWF (interface)	0.449	0.456
LD-SWF (Maxwell constr.)	0.407	0.467
GFMC (Maxwell constr.)	0.438	0.491
Experiment	0.438	0.465

Table 6.3: Melting and freezing densities of ^{4}He from LD-SWF calculations, Green Function Monte Carlo equation of state, and experiment.

Energy and pressure profiles

In figure 6.9 the total energy profile energy profile is shown for the {100} case. The energy of the bulk solid is lower than the energy of the bulk liquid (according to the discussion of the previous section), and their values are $E_s = -5.32 \pm 0.07K$ and $E_l = -5.20 \pm 0.07K$, in accordance with the results expected from the equation of state.

A feature that can be observed in the energy profile is the peak appearing in correspondence of the interface, that has to be connected with the interfacial energy, although it does not represent an efficient way of computing it, due to the statistical error that for such profiles is about 7 times larger than that on the average value of the energy per particle. The maximum of the excess energy, that is located inside the interfacial region, is of $0.1K$ per particle.

The profiles of quantum pressure and stress pose an apparent paradox. As it can be seen in fig. 6.10, the values of the pressure in the solid and in the liquid are quite different, that is 1.9 $K/\sigma^3 = 15.5$ atm in the solid, and 7.3 $K/\sigma^3 = 59.6$ atm in the liquid.

Actually, this values are consistent with the values that can be obtained from the equation of state provided by the LD–SWF ($\mathcal{P} = \frac{1}{\rho^2}\frac{\partial\epsilon(\rho)}{\partial\rho}$). To the difference in the

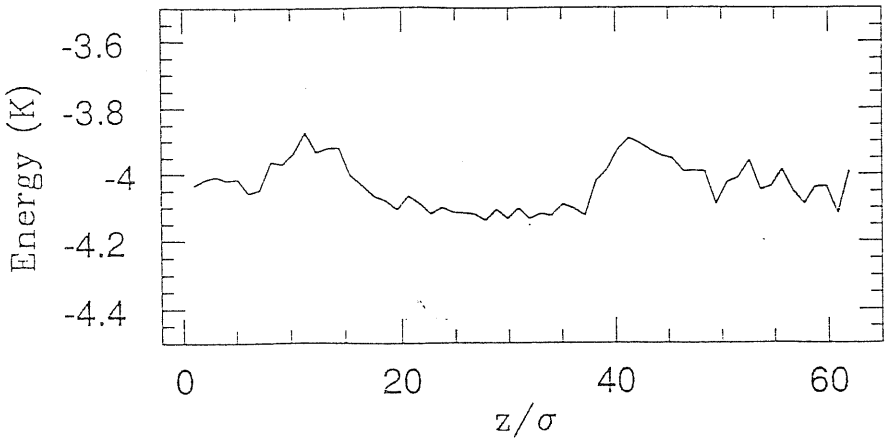

Figure 6.9: Per particle energy profile in {100} interface at density $\rho\sigma^3 = 0.452$. The values in the figure do not include the tail correction, that is $\sim 1K$

pressures, do not correspond the presence of stress in the sample. We can rule out that as it can be seen by the stress profile (fig. 6.11), which clearly excludes such occurrence. The difference in pressure is then connected to the width of the coexistence interval, and is consistent with the melting and freezing densities obtained in the simulation.

Comparison of the results at different densities

The profiles obtained at densities other than $\rho\sigma^3 = 0.452$ do not present features which are significantly different from those discussed above. An important check that has to be done is how much the lever rule of equation (6.3) is fitted. In figure 6.12 we show as an example, the fine scale density profile at density $\rho\sigma^3 = 0.4505$. The number of solid layers remained in the box is much lower, although at the beginning there was half solid and half liquid. The opposite effect has been observed in the simulation at density $\rho\sigma^3 = 0.4575$, where the sample solidified quite completely starting from a situation in which only one third of solid was present. The lever rule results to be satisfied within few percent.

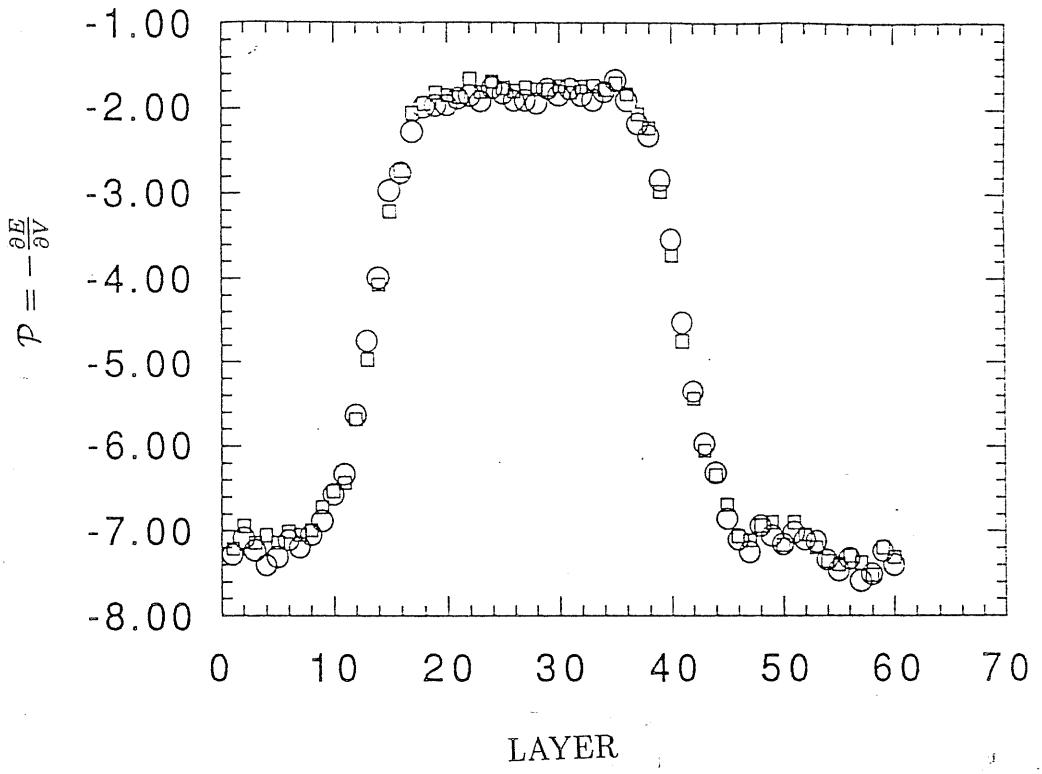

Figure 6.10: Profile of $-\mathcal{P} = \frac{\partial \mathcal{E}}{\partial \mathcal{V}}$ for the {100} interface at density $\rho\sigma^3 = 0.452$

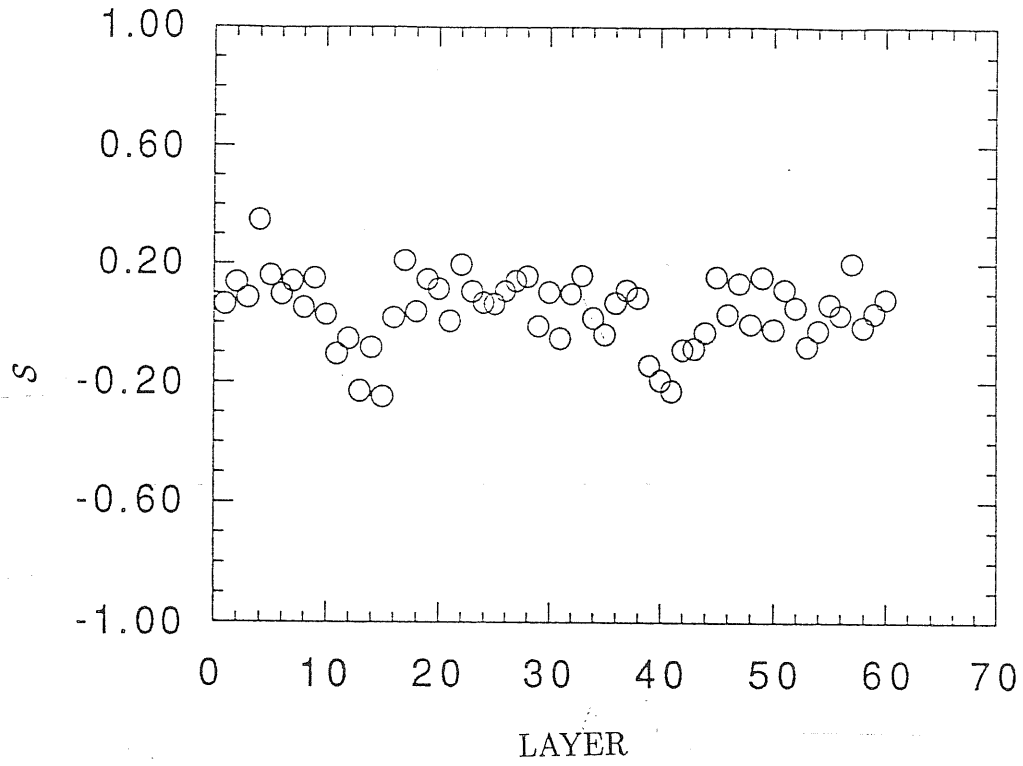

Figure 6.11: Stress profile for the {100} interface at density $\rho\sigma^3 = 0.452$

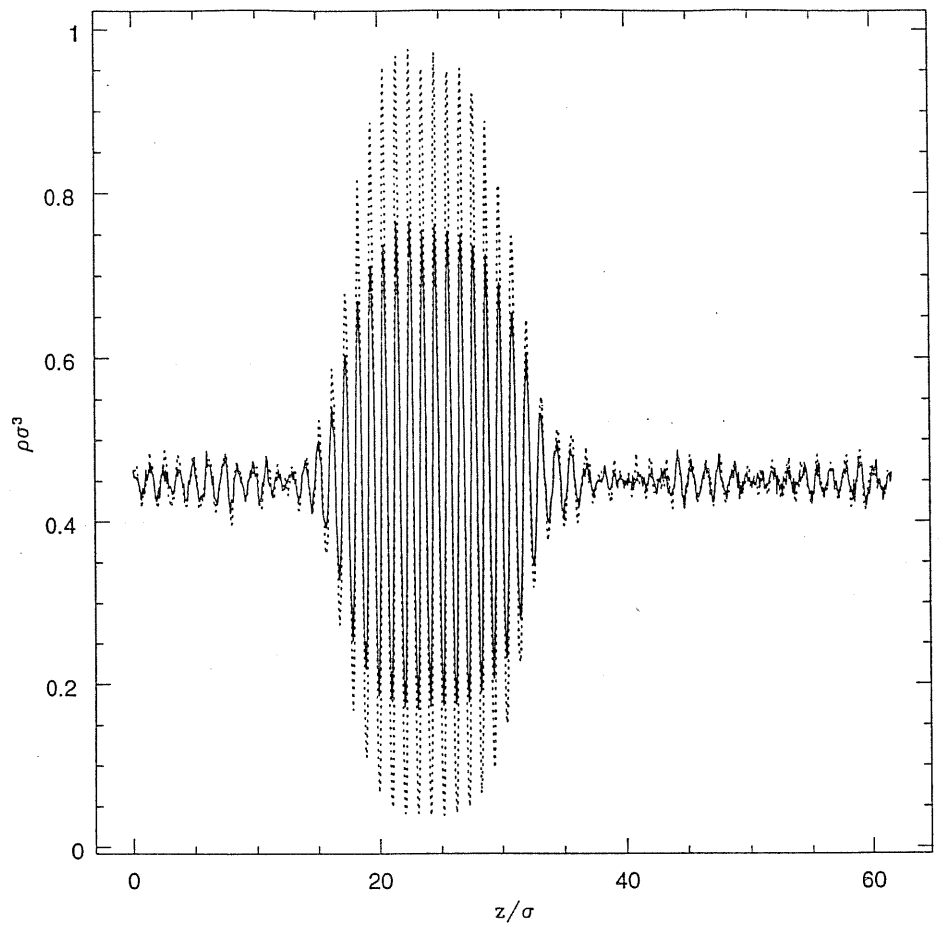

Figure 6.12: Fine scale density profile at density $\rho\sigma^3 = 0.4505$. Solid line: helium atoms; dashed line: shadows.

Configurations analysis

In fig. 6.13 the configuration plot of the particles in the interfacial region is shown. The layers considered are ten. This plot is relative to 24 configurations extracted from 16000 generated, and is a projection onto the $y - z$ plane. Here the passage from an ordered phase (on the right) to a disordered one is very clear. The interfacial region as seen in this picture consists on 4–5 layers, in which the localization of the particles tends gradually to be destroyed. The lines here connect consecutive positions of each particle. In the interfacial region the particles look to be free to move away from the crystalline sites, although they spend still some time around fixed positions, as signalled by the more and more blurred planes that can be observed. In fig. 6.14 we show a crystalline plane in the interface compared with one still inside the solid. There are still atoms occupying definite sites for some time and atoms diffusing more widely. Moreover some sites are not permanently occupied by the same atom, indicating that in the interfacial region exchange of particles is much more likely than in the solid, where all the atoms are well bounded around their equilibrium positions. The mobility of the atoms can be measured by the average square displacement from the initial positions $\delta r^2 = \langle (r - r_0)^2 \rangle$ (see fig. 6.15). In the solid this value is about $0.6\sigma^2$, meaning that the particles are displaced from the lattice sites no more than one half of the nearest neighbours distance. Going through the interface the value increases quite rapidly. It saturates well inside the liquid, where the average displacement is of $\sim 4\sigma$. This means that the first layers of liquid are still sensitive to the presence of the solid, and the mobility is somewhat depressed.

6.3.4 Interfacial energy

One of the major results of this calculation is the first theoretical estimate of the solid–fluid interfacial energy in ^{4}He. Consider an expansion of the equation of state in terms of

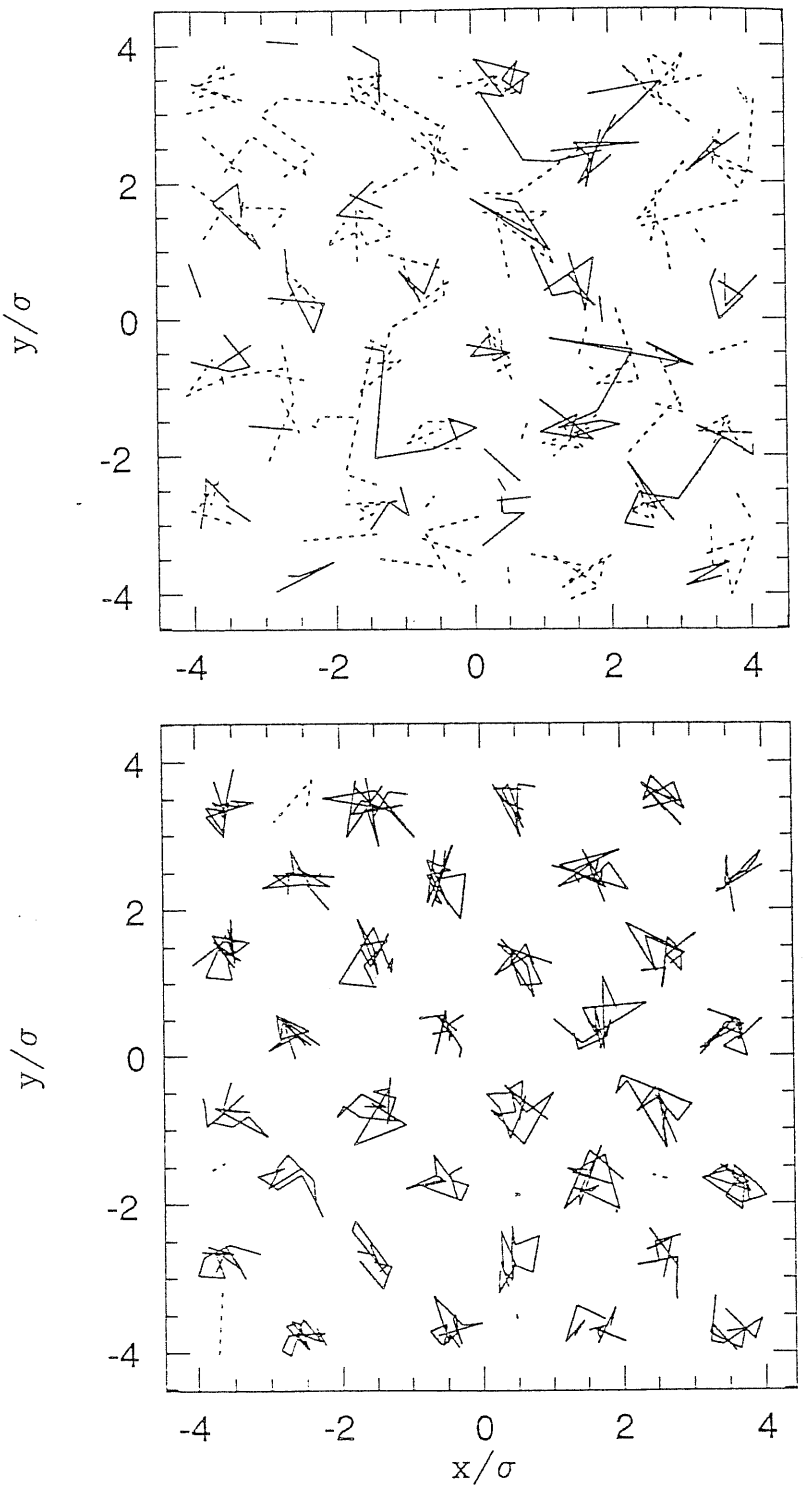

Figure 6.13: Configuration plot projected in the $y-z$ plane in the interfacial region

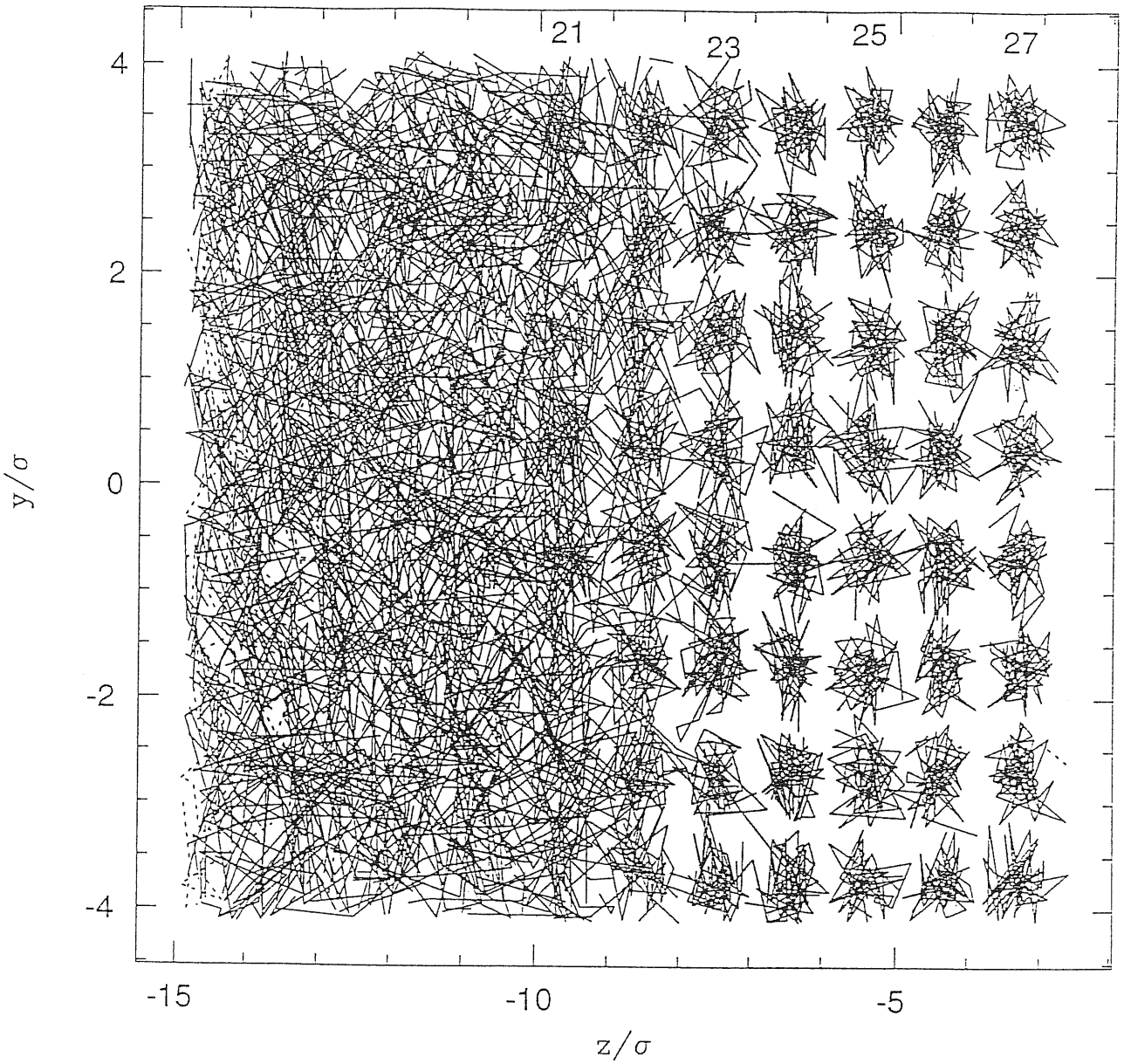

Figure 6.14: Configuration plots of particles for two layers in the interfacial region

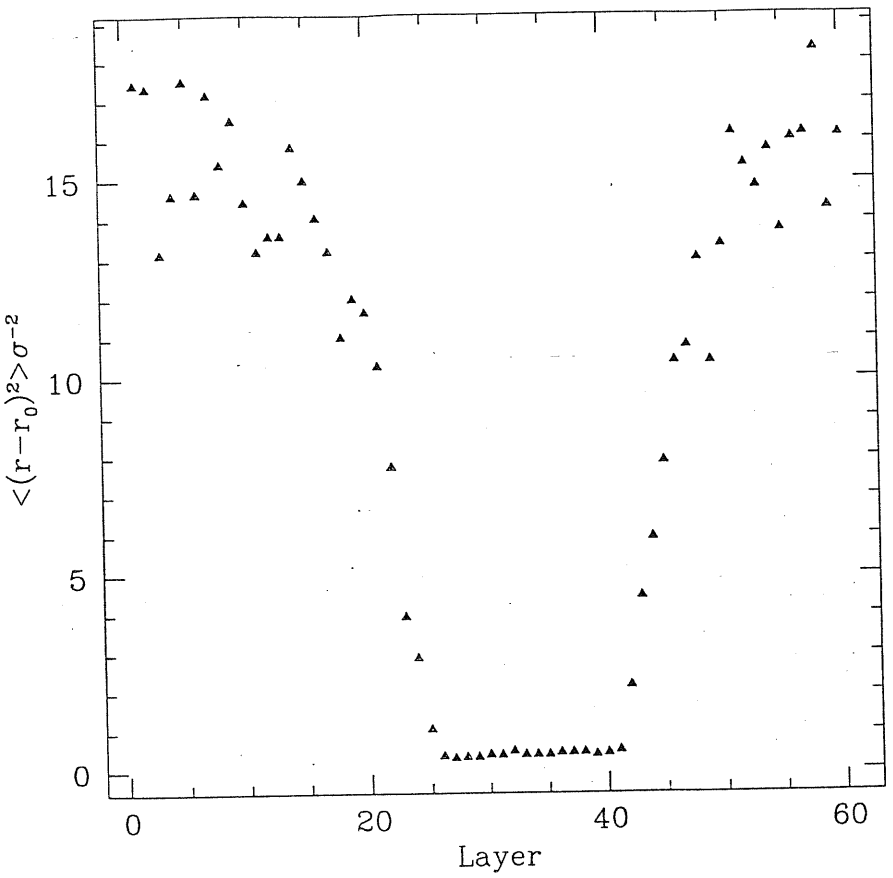

Figure 6.15: Profile of average square mobility of particles in the {100} interface at density $\rho\sigma^3 = 0.452$

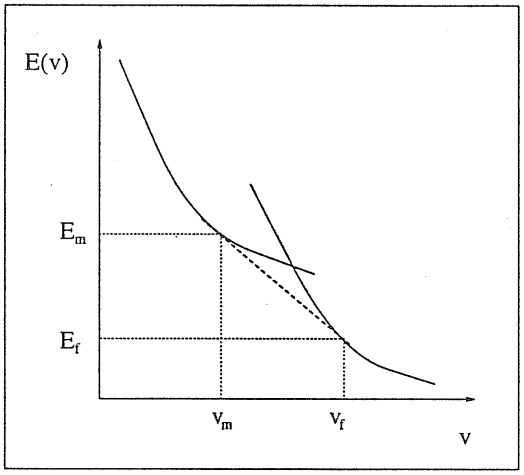

Figure 6.16:

specific volume $v = V/N$, around the freezing point for the liquid branch and around the melting point for the solid branch:

$$E_l = E_f - p(v - v_f) + \tfrac{1}{2}\alpha_f(v - v_f)^2$$
$$E_s = E_m - p(v - v_m) + \tfrac{1}{2}\alpha_m(v - v_m)^2 \tag{6.9}$$

with $E_f < E_m$ and $\alpha_f > \alpha_m$ see fig. 6.16

If the simulation box containing N particles, N_S of which in the solid phase and N_L particles in the liquid phase, the bulk contributions to the total energy per particle can be written as:

$$\frac{E_B}{N} = \frac{N_S}{N}\left[E_m - p(v - v_m) + \frac{1}{2}\alpha_m(v - v_m)^2\right] + \frac{N_L}{N}\left[E_f - p(v - v_f) + \frac{1}{2}\alpha_f(v - v_f)^2\right]. \tag{6.10}$$

The energy measured differs from E_B/N and we define interfacial energy the difference among the calculated value and E_B/N. It is convenient to express this contribution in terms of interfacial energy per surface unit ϵ_{surf}. Therefore the total energy can be written

as:

$$\frac{E_{tot}}{N} = \frac{E_B}{N} + \frac{2S}{N}\epsilon_{surf}, \tag{6.11}$$

where S is the area of the $x - y$ section of our simulation box. and the factor 2 is due to the presence of two interfaces in it. In order to take into account possible finite size effects we parametrized ϵ_{surf} in the following way:

$$\epsilon_{surf} = \epsilon_0 - \beta[\Delta v - (v' - v'')], \tag{6.12}$$

where v' and v'' are the freezing and melting specific volumes found in the simulation, namely:

$$v' = 2.227 \pm 0.005,$$

$$v'' = 2.193 \pm 0.009.$$

We fitted the values of the energy per particle at the four densities considered with the expression in eq. (6.11). The results are given in table 6.4, where are displayed all the values obtained considering the uncertainty Δv on v' and v''.

From the fitted values it comes out clearly that β is compatible with 0, so we can rule out strong finite size effects. The largest source of uncertainty is due to the errorbars on the values of the freezing and the melting densities. The final value for ϵ_0 is then given by

$$\epsilon_0 = 1.17 \pm 0.48 \ \frac{K}{\sigma^2} = 0.18 \pm 0.07 \ \frac{K}{\text{Å}^2},$$

that is very close to the extrapolated experimental value [70].

6.4 Correlation pseudopotentials and coexistence range

In the previous sections we pointed out a couple of apparent inconsistencies in the results, mainly concerning the region of phase coexistence:

ϵ_0	$v' - \Delta v'$	v'	$v' + \Delta v'$
$v'' - \Delta v''$	0.82 ± 0.14	0.99 ± 0.14	1.12 ± 0.14
v''	1.00 ± 0.14	1.16 ± 0.14	1.28 ± 0.14
$v'' + \Delta v''$	1.33 ± 0.14	1.44 ± 0.14	1.51 ± 0.14

β	$v' - \Delta v'$	v'	$v' + \Delta v'$
$v'' - \Delta v''$	-1.51 ± 0.50	-0.89 ± 0.51	-0.39 ± 0.52
v''	-0.84 ± 0.48	-0.27 ± 0.49	0.14 ± 0.50
$v'' + \Delta v''$	0.30 ± 0.47	0.67 ± 0.48	0.93 ± 0.49

Table 6.4: Fitted values of ϵ_0 and β in eq. (6.11).

- the coexistence region is very narrow with respect to what expected from the Maxwell construction;
- there is a wide difference in pressure among the two phases without an evident stress in the solid. Nevertheless the system is mechanically stable.

A possible cause of the first point might be the occurrence of strong finite size effects. We can rule out this hypothesis, because simulations with boxes of different length (with 120 and 40 layers respectively) and with different area of the section of the simulation box ($5 \times 5 \times 5$ cells) stabilize immediately at the same melting and freezing densities, in spite of the fact that the gap between the initial densities of the solid and of the liquid was made larger.

The incorrect behaviour, of the equation of state, and consequently of the pressure and of the stress, lies in the fact that our wave function differs from the exact eigenfunction more on the coexistence region than in the homogeneous phases. The variational principle

does not guarantee good results for the coexistence properties. Actually one can try to use the properties at the coexistence to get a better trial wave function closer to the eigenfunction. The simulation is governed by the probability distribution determined by $|\Psi|^2$. Let us consider for instance a Monte Carlo simulation in ^{4}He with a variational wave function of the pure Jastrow form with a McMillan correlation pseudopotential. The Metropolis algorithm does not distinguish among this case by an ensemble of soft spheres interacting via a potential $V(r_{ij}) = (b/r_{ij})^5$, where the canonical probability distribution is

$$\pi(R) = \prod_{i<j} e^{-\beta\left(\frac{b}{r_{ij}}\right)^5}, \tag{6.13}$$

with $\beta = 1$. As a consequence the various estimators, *with the exception of* E behave during the simulation as in an ensemble of soft spheres interacting with the McMillan potential. A similar feature occurs in our case. As written in appendix A, the probability distribution governing the random walk in a SWF simulation is:

$$\pi(R, S^L, S_R) = \prod_{i<j} \left[e^{-\left(\frac{b_p}{r_{ij}}\right)^5 - C(r_i - s_i^L)^2 - C(r_i - s_i^R)^2 - \left(\frac{b_s}{s_{ij}^L}\right)^9 - \left(\frac{b_s}{s_{ij}^R}\right)^9} \right]. \tag{6.14}$$

Consider the "partition function" for a fictious classical system described by π:

$$Z = \int \pi(R, S^L, S^R) dR dS^L dS^R. \tag{6.15}$$

Let:

$$f_{ij} = e^{-\left(\frac{b_p}{r_{ij}}\right)^5 - \left(\frac{b_s}{s_{ij}^L}\right)^9 - \left(\frac{b_s}{s_{ij}^R}\right)^9} - 1, \tag{6.16}$$

$$f_0^{i\alpha} = e^{-C(r_i - s_i^\alpha)^2}.$$

We have then

$$Z = \int dR dS^L dS^R \prod_i f_0^{i_L} f_0^{i_R} \prod_{i<j} (f_{ij} + 1). \tag{6.17}$$

The first order cluster expansion, considering the gaussians as mean field (see ref. [26]), gives the approximate expression:

$$Z \sim V^N \left(\frac{\pi}{C}\right)^{3N} \left[1 + \frac{N(N/1)}{2V^2} \left(\frac{\pi}{C}\right)^6 \int f_0^{1_L} f_0^{1_R} f_0^{2_L} f_0^{2_R} f_{12} dr_1 dr_2 ds_1^L ds_1^R ds_2^L ds_2^R\right], \tag{6.18}$$

where V is the volume of the system and N is the number of particles.

The integral in (6.18) can be evaluated using again a cluster expansion. Defining the following symbols:

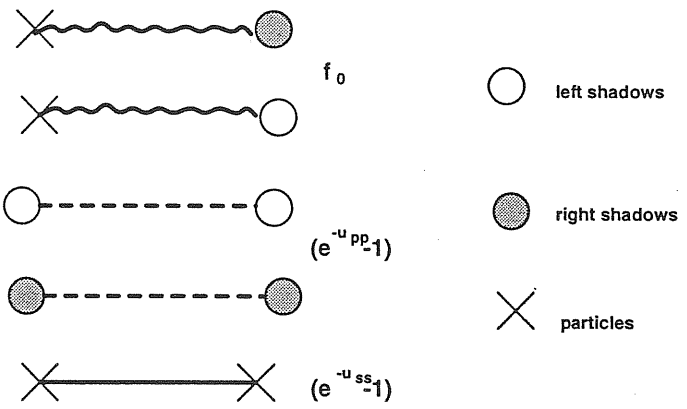

the integral is the sum of the following contributions:

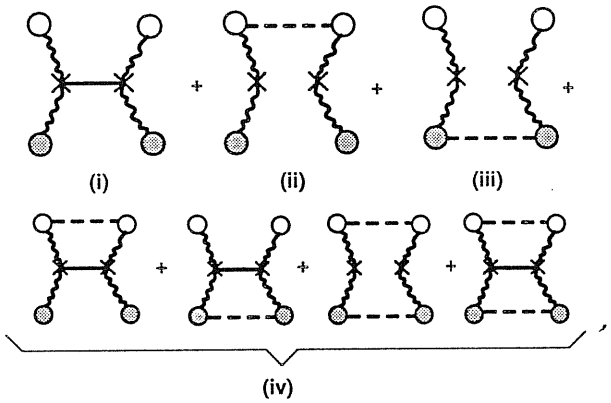

The diagrams (ii) and (iii) are completely equivalent, while the diagrams labelled with (iv) are negligible because of order $\frac{1}{(2\pi)^6}$ with respect to (i–iii). Further development of the calculations leads to the following result for the approximate partition function

$$Z \sim V^N \left(\frac{\pi}{C}\right)^{3N} \left[1 + 4\pi N\rho \left(\frac{1}{5}\Gamma\left(-\frac{3}{5}\right) b_p^3 + \frac{2}{9}\Gamma\left(-\frac{1}{3}\right) b_s^3\right)\right]. \tag{6.19}$$

The expression (6.19) implies that once C is fixed, the partition function depends only on a reduced density γ whose expression is:

$$\gamma = \rho \left[\frac{1}{5}\Gamma\left(-\frac{3}{5}\right) b_p^3 + \frac{2}{9}\Gamma\left(-\frac{1}{3}\right) b_s^3\right] \tag{6.20}$$

With such expression we can check if the width of the interfacial region depends only on the particular functional form chosen for the correlation pseudopotentials. Remembering that in LD-SWF $b_s \to b_0 + b_1\rho$, and keeping th value $b_p = 1.12\sigma$, and substituting to the Γ functions their numerical values, we can transform eq. (6.20) in:

$$\gamma = \rho[0.90(b_0 + b_1\rho)^3 + 1.04] \tag{6.21}$$

The hypotesis that the free energy depends only by γ has the consequence that the coexistence interval, is known for any value of the parameters appearing in eq. (6.21), if it is

known at least for one set of parameters. The simulations with $b_0 = 0.51$ and $b_1 = 1.91$ give $\rho_f = 0.449 \pm 0.001$ and $\rho_m = 0.456 \pm 0.002$, and consequently the values for the reduced densities corresponding to the extrema of the coexistence interval are:

$$\gamma_f = 1.503 \pm 0.015, \tag{6.22}$$

$$\gamma_m = 1.558 \pm 0.032. \tag{6.23}$$

If we want to reproduce roughly the experimental range of coexistence ($\rho'_f\sigma^3 = 0.435$, $\rho'_m\sigma^3 = 0.460$), we must solve for b_0 and b_1 the system of equations:

$$\gamma_f = \rho'_f[0.90(b_0 + b_1\rho'_f)^3 + 1.04]$$

$$\gamma_m = \rho'_m[0.90(b_0 + b_1\rho'_m)^3 + 1.04]$$

The calculations give $b_0 = 1.68\sigma$ and $b_1 = -0.67\sigma^4$. A simulation of 25000 MCS plus 20000 of equilibration at average density $\rho\sigma^3 = 0.445$ gives 12 layers of stable solid, and the freezing and melting densities are $\rho_f = 0.439 \pm 0.002$ and $\rho_m = 0.464 \pm 0.002$, consistent with the values expected and to which the parameters have been fitted. Obviously with such a change of b_0 and b_1 the value of the total energy in the bulk liquid and solid become higher, but now they are in the order expected ($\epsilon_{sol} > \epsilon_{liq}$), although their values are very close one to the other ($\epsilon_{sol} = -5.28K$ and $\epsilon_{liq} = -5.35K$).

A very important point is that the value of the interfacial energy obtained with this new values of the parameters b_0 and b_1, does not vary much respect to what found before ($0.10 \pm 0.08K/\text{Å}$). This means that the interfacial energy is not very sensitive to the parametrization chosen, and depends mainly on the presence of a mismatch between an ordered and a disordered phase.

6.5 Perspectives

The study of the solid–liquid interface by means of the LD– SWF already gave excellent results. The use of the improved wave function makes sensible more detailed studies of the interfacial structures. A very interesting calculation that can be performed regards the computation of the change in the condensate fraction across the interfacial region. More detail can be also still given about the geometrical properties of the solid layers in contact with the liquid, in order to understand better how the density changes in proximity of the solid and if the packed structure of the crystal is maintained.

Other problems will be attacked with the use of LD–SWF. We will mention three possible fields of application in the helium physics. First of all this wave function can be used to face on a microscopic point of view some problems of surface physics that otherwise can be studied only by means of mean field calculations. It is possible to calculate, starting from the estimation of the interfacial energy, the roughness properties of the interfaces at various orientations, or the step energy in a tilted interface, that has been recently measured. Secondly there are several question to be answered in the behaviour of impurities (^{3}He or other) in the two phases system. For instance, it is known experimentally that such impurities are always located at the interface. It is not yet clear if this is due to a static effect, in the sense that there is a surface bound state for the impurity, or to a dynamic effect, connected to the difference among the crystal growth velocity and the diffusion velocity of the impurities in the liquid. A simple calculation based for instance on the Lekner approximation could already give some indication about this problem. Eventually one can also study more challenging inhomogeneous systems, such the helium films deposited on a graphite substrate, and that seem to present a couple of layers of solids, each one with a different structure, and then a liquid. Some study in this direction has already been performed by Ceperley and Pollock[58] with Path Integral

Monte Carlo techniques, but the very small number of atoms that can be managed at the moment, does not allow for giving a satisfactory theoretical analysis of this effect.

7 Shadow wave Function for Normal ^{3}He

In this chapter we present an extension of the SWF, originally proposed for Bose systems, to treat strongly interacting Fermi systems, such as liquid and solid ^{3}He. In recent years, several ab initio calculations based on variational theory have been performed. They are based either on Fermi HyperNetted Chain (FHNC)[45, 71] theory or on VMC[72, 42] methods. Obviously one would like to carry out GFMC or DMC calculations on ^{3}He, like for ^{4}He. However this has not been possible yet, due to the sign problem, typical of Fermi systems, and GFMC[72] and DMC[47] calculations has been carried out under the constraints of fixing the nodes of the wave function[73]. These need to be determined by a previous variational calculation.

The main perspective in extending the SWF ansatz to the case of Fermi systems is to open the possibility of ab–initio calculations for solid ^{3}He as a possible component.

The typical trial wave function for a Fermi system is made up of a bosonic correlation operator, as the one discussed for ^{4}He acting on a mean field wave function φ, which is antisymmetric under the exchange of the particles[74]. Therefore one can think of including the shadow degrees of freedom in the bosonic part of the wave function, or in the antisymmetric part, or in both. Since we are mainly interested in giving a realistic

ansatz for solid ^{3}He we developed here only the case in which th shadow degrees of freedom enters the Bose part of the wave function. We will also present preliminary results obtained both in the liquid and in the solid phase, and performed with Monte Carlo methods.

7.1 VMC calculations for normal ^{3}He

Monte Carlo techniques have been widely applied in the study of the ground state properties of ^{3}He . The approaches do not differ substantially from that used for ^{4}He. The major complication comes from the antisymmetry of the trial wave function. In the case of normal ^{3}He this is realized by taking the mean field part of the wave function φ of the following form[42]:

$$\varphi \mathbf{r}_1 \cdots \mathbf{r}_N = D_\uparrow(\mathbf{r}_1 \cdots \mathbf{r}_{N/2}) D_\downarrow(\mathbf{r}_{N/2+1} \cdots \mathbf{r}_N), \tag{7.1}$$

where $D_\sigma(\mathbf{r}_1 \cdots \mathbf{r}_N)$ is the Fermi gas wave function of N fermions with spin σ. The correlation factor $F(\mathbf{r}_1 \cdots \mathbf{r}_N)$ is the same as for ^{4}He. However in Fermi systems the backflow not only provides triplet correlations, but also momentum dependent correlations. These are usually taken into account modifying the plane waves in the determinants D_σ, namely considering the following single particle orbitals:

$$\varphi^{\mathbf{k}}_{\mathbf{r}_i} = \exp(i\mathbf{k}\cdot\mathbf{r}_i) - \exp\left[i\mathbf{k}\cdot\left(\mathbf{r}_i + \lambda_B \sum_{i\neq j} \eta(r_{ij})\mathbf{r}_{ij}\right)\right]. \tag{7.2}$$

Table 7.1 reports the results of some variational calculations carried out at density $\rho\sigma^3 = 0.277$[42], compared with Fixed Node Diffusion Monte Carlo, (FN-DMC)[47] and the experimental value at the equilibrium density $\rho\sigma^3 = 0.273$[1]

[1]The small discrepancy in the values of the density at which the simulations were performed, are due to more recent accurate experimental determination of the equilibrium density (see e.g. ref. [75] and

Ψ_T	$E \pm \Delta E$
Jastrow–Slater	-1.08 ± 0.03
JS + Triplet	-1.61 ± 0.03
JS + Backflow	-1.55 ± 0.04
JS + Trip. + Back.	-1.91 ± 0.04
	$-2.0947 \pm 0.0056^*$
DMC (Fixed node)	$-2.2991 \pm 0.0069^*$
Experiment	-2.47 ± 0.01

Table 7.1: Variational energies for different trial wave functions from ref. [42]. Numbers marked with * are from ref. [47].

As in the case of ^{4}He the use of backflow correlations give a lower upper bound for the energy. The discrepancy with DMC results is still $\sim$ 10%, indicating that n–body correlations with $N > 3$ are not negligible.

Much less satisfactory is the situation in the solid phase, where most of the calculations have been performed in terms of mass three bosons, based on the fact that in a crystalline structure the exchange effects are small. Ceperley et al.[74] considered an antisymmetric wave function for the solid, in which a Slater determinant of gaussians centered on lattice sites is used.

7.2 Slater–Shadow Wave Function

Our generalization of the SWF for a fermionic system follows the way indicated in the variational calculations previously discussed, and includes the shadow degrees of freedom

references therein).

in the bosonic part only, namely:

$$\Psi_T(R) = \varphi e^{-\frac{1}{2}\sum_{i<j} u_{pp}(r_{ij})} \int dS \prod_i e^{-C|\mathbf{r}_i - \mathbf{s}_i|^2} e^{\sum_{i<j} u_{ss}(s_{ij})} \tag{7.3}$$

In our calculations we included backflow correlation via eq. (7.2) The correlation pseudopotential among the particles, u_{pp}, has been taken of the McMillan form, and for shadow–shadow correlation,u_{ss} we have used the rescaled Aziz pseudopotential $u_{ss}(s) = \delta V(\alpha s)$ (see chapter 3 for definitions). Recalling the PIMC framework[53] we can interpret this wave function as describing the centers of mass of the delocalized quantum particles as "quasi classical" objects, for which the exchange force is not effective, while the quantum effects are accounted for the real particles.

From a computational point of view the introduction of the Slater determinant multiplying the shadow type correlation factor does not change substantially the numerical procedures , except for the changes usually needed when passing from bosons to fermions. In particular there are now some restrictions on the number of particles to be employed. One can use only an odd number of particles for each spin component. This is due to the requirement of having a zero total momentum in system, because in building the Fermi sea one starts to fill the $k = 0$ state and successively pairs of states with momentum $\pm k$. Moreover in order to have a wave function with spherical symmetry it is necessary to fill a complete shell of k vectors in the k-space. This is obtained for $n = 1, 9, 19, 27, 33, 54...$, while the total number of particles is restricted to $N = 2n$, therefore $N = 2, 18, 38, 54, ...$ This has to be combined with the compatibility with a b.c.c. lattice (experimentally found to be the stable phase of solid ^{3}He)[75]. The presence of backflow correlations implies the computation of the determinant at each elementary move, so that becomes convenient to perform a collective gradient–biased move at least for the particles. The evaluation of the kinetic energy estimators is also modified by the presence of the Slater determinant,

in the sense that we have to add to the particle–particle pseudopotential the contributions coming from $-\log(D_\downarrow D_\uparrow)$. This does not influence in any way the shadow contributions. As for the ^{4}He case we have two distinct estimators, the Jackson Feenberg and the Pandharipande Bethe kinetic energies, whose equality signals the reached equilibrium.

7.3 Liquid phase

In order to optimize the variational parameters in the liquid phase we proceeded with a scanning over a region of the parameters space close to the point that optimizes the SWF in the bosonic case. In particular we can fix some criteria basing on past simulations and on physical considerations.

We explored a whole multidimensional grid of parameters. The simulations were performed with 54 particles in a cubic box with periodic boundary conditions. The density was fixed to $\rho\sigma^3 = 0.273$. Table 7.2 reports the values for the variational energy, kinetic and potential energy for some of the values of the parameters considered, close to the "optimal" ones. Preliminary results obtained for runs with 114 particles confirm the estimates reported in the table. One should notice that the particle–particle correlation has a narrower core than in the bosons, in agreement with simulations with Jastrow–Slater which give an optimal value for b of 1.13σ (to be compared with 1.20σ of ^{4}He). The parameter C, is also reduced, consistently with the mass difference between ^{3}He and ^{4}He.

The results obtained with our SSWF are of the same quality as those of SWF in ^{4}He. This is very encouraging in view of extending the study of liquid–solid coexistence to ^{3}He.

$b_p(\sigma)$	$C(\sigma^{-2})$	$\delta(K^{-1})$	α	$E(K)$	$E_{pot}(K)$	$E_{kin}(K)$
1.08	3.5	0.1	0.85	-1.70 ± 0.03	-13.88 ± 0.04	12.18 ± 0.04
1.08	3.5	0.105	0.88	-1.66 ± 0.03	-13.72 ± 0.03	12.06 ± 0.04
1.08	3.5	0.095	0.88	-1.82 ± 0.03	-13.70 ± 0.03	11.88 ± 0.04
1.08	4.0	0.1	0.88	-1.80 ± 0.03	-14.04 ± 0.03	12.24 ± 0.04
1.10	3.5	0.095	0.88	-1.75 ± 0.03	-14.16 ± 0.03	12.41 ± 0.04

Table 7.2: Results for some runs with SSWF in ^{3}He. The number of particles employed is $N = 54$. Each run consists of about 70000 MCS

7.4 Solid phase

Solid ^{3}He is one of the most interesting quantum solids. to be studied. SSWF may provide a powerful tool for systematic description of its properties, taking into account the antisymmetry of the wave function, and without including a priori symmetry breaking conditions. It is known that the stable crystalline phase of ^{3}He above the melting pressure has a body center cubic (b.c.c.) structure. Conventional correlations, (purely repulsive but also attractive if the pressure is not very high)[76] are not able to stabilize such a structure. Moreover it has been impossible up to now to build a Slater wave function with the correct crystalline symmetry, without taking localized (e.g. gaussians) single particle functions. Our wave function overcomes this problems. We could obtain a stable b.c.c. crystalline structure with SSWF due to the fact that particle–particle correlations are affected in a significant way by the presence of the determinant which introduces a repulsion which increases the effective pressure in the system.

So far we have performed simulations at just one density ($\rho\sigma^3 = 0.440$), with $N = 54$ particles and *starting* already with a b.c.c. structure. In order to prove the stability of

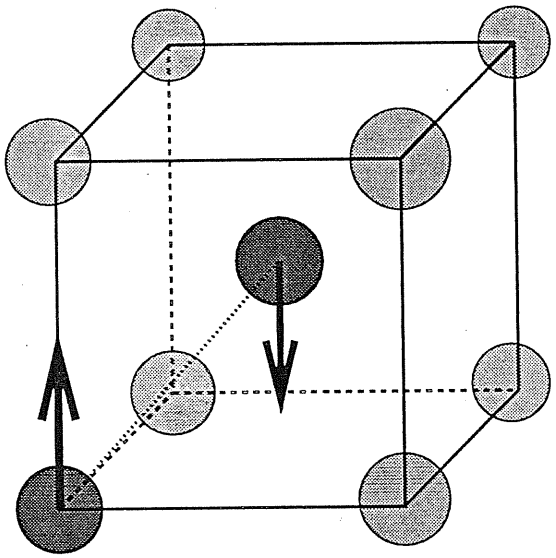

Figure 7.1: Elementary conventional cubic cell in the case of AFM bcc crystal. Darker particles constitute the basis of the lattice.

the b.c.c structure a crystallization experiment, as that described in chapter 5 for ^{4}He, is needed. In order to have also indications on the sensitivity of the wave function to the spin ordering we are considering two different starting configurations: one antiferromagnetic (AFM) and one ferromagnetic (FM). We recall that backflow correlations distinguish between singlet and triplet spin pairs, and therefore simulates spin–dependent correlations[45]. The results obtained so far refer to the AFM case.

7.4.1 The AFM case

In the antiferromagnetic case each elementary conventional cubic cell accommodates two particles with different spins (see fig 7.1).

Such a configuration is known to be the ground state of 3D spin models with pure nearest neighbours interactions. We expect it to be energetically favoured with respect to

$b(\sigma)$	$C(\sigma^{-2})$	$\delta(K^{-1})$	α	$E_0(K)$	ord. par. (particles)	ord. par. (shadows)
1.09	3.5	0.09	0.083	2.486 ± 0.038	0.161	0.201
1.09	3.5	0.09	0.081	1.470 ± 0.023	0.506	0.726
1.09	3.5	0.09	0.078	1.640 ± 0.023	0.520	0.812
1.07	3.5	0.09	0.081	1.356 ± 0.024	0.492	0.725
1.09	3.5	0.07	0.083	1.772 ± 0.025	0.470	0.674

Table 7.3: Variational energies in solid ^{3}He at density $\rho\sigma^3 = 0.440$. In the last two columns the crystalline order parameter for particles and for shadows is given.

a ferromagnetic configuration. [1]

For this configuration we explored the parameters space. The crystalline order has been tested using the crystalline order parameter defined in chapter 6. The vectors employed here belong to a star of vectors in the reciprocal lattice (a f.c.c.), that all the vectors connecting one site with the nearest neighbours. In table 7.3 we report the results obtained for values of the parameters close to the optimal ones.

As can be seen the parameter α (equivalent in some sense to the b_s of the SWF) plays again a crucial role in stabilizing the solid. There exist a critical value below which the crystal melts. The energetic behaviour is similar to that of solid ^{4}He: a rapid drop in the energy is observed passing from the fluid to the solid. There is a minimum near the critical value of α, thereafter a new rise, eventually towards the Nosanow value. Order parameters at the minimum indicate again that shadows are more localized than particles.

[1] Experimentally the ground state of unpolarized solid ^{3}He is found to be paramagnetic at higher temperatures; at lower temperatures it consist in a succession of ordered planes with a sequence like up–up–down–down–up–up... and so on. [75]It would be sensible to test such configurations when a true spin–spin correlation were introduced. Within our approximation we can reasonably consider AFM b.c.c. as a good enough approximation for the ground state

The mechanism of crystallization is presumably of the same kind of that in ^{4}He, although here the real particles play a more significant role in determining the final geometry. The order parameter reported in table 7.3 has the form:

$$O_p = \langle \sum_{\mathbf{G}} \sum_{i=1}^{N} |e^{i\mathbf{k}\cdot\mathbf{r}_i}| \rangle \tag{7.4}$$

Where $\mathbf{G}$ are vectors belonging to a star of crystalline planes in the b.c.c. crystal. The sum over the moduli has been used in order to avoid the effect of the spurious motion of the center of mass of the simulation box. In the liquid phase such order parameter gives a value $\sim 1/\sqrt{N}$, while in a perfect crystal it assumes a value of 1, as the order parameter discussed in chapter 6. The effect of the antisymmetrization of the wave function in ^{3} was discussed by Ceperley et al.[74] for the first time in 1977. In that case the trial wave function consisted of a determinant of gaussians localized on a b.c.c. lattice, multiplied by a Jastrow factor. The result was compared with analogous calculations of Hansen and Levesque[77], performed on mass 3 bosons. The energy per particle found in that case is $1.07 \pm 0.03K$, with 864 particles, while for the antisymmetric wave function one gets $1.57 \pm 0.08K$ with 54 particles. These results were obtained at a density lower than that employed for SSWF calculationsi, that is $\rho\sigma^3 = 0.427$. The energy upperbound found with SSWF is not so far form these numbers, demonstrating that also in the solid phase this trial wave function can give reasonable results.

7.5 Perspectives

The SSWF applied to fermionic systems open many perspectives, and not limited to the study of ^{3}He. The first application can be the study of the solid–liquid interface, that appears to be computationally more demanding with respect to the analogous calculation in ^{4}He. Nevertheless the use of parallelization techniques should allow for gaining in speed

enough to reduce the computation in a reasonable time. Another important application can be a systematic theoretical study of the solid phase in ^{3}He, that is still completely lacking.

In this chapter we introduced the SSWF only for normal Fermi liquids. Starting from recently presented VMC calculations on superfluid ^{3}He, it should be possible to introduce SWF also in superfluid systems.

Finally other interesting applications of SSWF could be the study of Wigner crystallization in the electron gas, or that of strange neutron matter.

Appendix A
Computational procedures in Variational Monte Carlo SWF calculations

In this appendix, we want to sketch out rapidly the computational procedure used to implement SWF calculations with Variational Monte Carlo (VMC) techniques. VMC allows for computing average values of local operators $O(R)$ on a given trial wave function Ψ_T depending on a set $\{\alpha\}$ of variational parameters. When using SWF, the average value of the operator O is calculated integratxiinge over three different sets of degrees of freedom:

$$\langle \Psi(R) O(R) \Psi(R) \rangle =$$

$$\int dR \psi_r(R) \int dS^L \theta(R, S^L) \psi_s(S^L) O(R) \psi_r(R) \int ds^R \theta(R, S^R) \psi_s(S^R).$$

The superscripts L and R mean "left" and "right" (denoting the w.f. multiplying O from left and right). The Monte Carlo integration can be performed using the standard Metropolis procedure. The probability distribution to be sampled involves both particles

and shadows and can be written as:

$$\pi(R, S^L, S^R) = \psi_r^2(R)\theta(R, S^L)\psi_s(S^L)\theta(R, S^R)\psi_s(S^R) \tag{A.1}$$

where $\psi_r(R)$,$\psi_s(S)$ and $\theta(R, S)$ are defined in eqs. (3.2)–(3.4).

Sampling

The sampling is performed moving in sequence the particles, the left shadows and the right shadows. The random displacement is performed in a cubic box of side Δ_r for particles and Δ_s for shadows. Each move is then checked for acceptance following the prescription of the detailed balance, that is calculating the ratio:

$$\xi = \frac{\pi_{new}(R, S^L, S^R)}{\pi_{old}(R, S^L, S^R)}$$

and then accepting the move with probability:

$$\min(\xi, 1).$$

The fraction of moves accepted is kept around the 30%. In order to have the same acceptance for particles and shadows the steps must be different. Δ_s must be lower than Δ_p, Confirming the fact that shadows diffuse more slowly.

Modification of energy estimators introducing SWF

The configurations generated during the Metroplis random walk are processed in order to get informations about the system. We want to describe quickly the main estimators employed in order to see the modifications needed when shadows are added. First of all we have some change in the estimators of the kinetic energy, due to the contributions coming from the particle–shadow interaction term. We remind that in a VMC calculation the

energy is estimated averaging the local energy $\hat{H}\Psi/\Psi$. The direct evaluation leads to the so called *Pandharipande -Bethe* kinetic energies, that we report in a form symmetrized with respect to the contribution from the left and right shadows:

$$\begin{aligned}\hat{T}_{PB} &= \frac{\hbar^2}{4m}\Bigg[-\sum_i\sum_{j\neq i}\vec{\nabla}_i^2 u_{pp} \\ &+ \frac{1}{2}\left(\sum_{j\neq i}\vec{\nabla}_i u_{pp}\right)^2 + \left(\sum_{j\neq i}\vec{\nabla}_i u_{pp}\right)\cdot(\vec{\nabla}_i u_{pl}) \\ &+ \left(\sum_{j\neq i}\vec{\nabla}_i u_{pp}\right)\cdot(\vec{\nabla}_i u_{pr}) - \vec{\nabla}_i^2 u_{pl} - \vec{\nabla}_i^2 u_{pr} \\ &+ \left(\vec{\nabla}_i u_{pl}\right)^2 + \left(\vec{\nabla}_i u_{pr}\right)^2\Bigg]\end{aligned} \tag{A.2}$$

Applying the Jackson–Feenberg identity one gets the *Jackson–Feenberg* form of the kinetic energy:

$$\begin{aligned}\hat{T}_{JF} &= \frac{\hbar^2}{4m}\Bigg[\sum_i -\frac{1}{2}\sum_{j\neq i}\vec{\nabla}_i^2 u_{pp} \\ &- \frac{1}{2}\vec{\nabla}_i^2 u_{pl} - \frac{1}{2}\vec{\nabla}_i^2 u_{pr} + \frac{1}{2}\left(\vec{\nabla}_i u_{pl}\right)^2 + \frac{1}{2}\left(\vec{\nabla}_i u_{pr}\right)^2 \\ &- \left(\vec{\nabla}_i u_{pl}\right)\cdot\left(\vec{\nabla}_i u_{pr}\right)\Bigg]\end{aligned} \tag{A.3}$$

Comparison between PB and JF kinetic energies gives informations about the equilibration of the system. In fact this two estimators must lead at the same mean value. Usually T_{JF} has a smaller variance than T_{PB}, but if we consider the *total energy*:

$$< E >=< T > + < V >,$$

it comes out that the use of PB expression gives a smaller variance. The computation of both the estimators is very useful. Notice that the shadow–shadow correlation pseudopo-

tential does not enter any of these expressions of the kinetic energy, implying that the calculation of the total energy does not depend on the particular choice of u_{ss}.

Appendix B
Methods for MC calculations in large systems

In this appendix we describe briefly the modifications needed in the algorithm in order to deal with simulation boxes containing a large number of atoms N. In this situation the heaviest part of the computation is given by the evaluation of changes in the probability distribution (A.1), that must be computed for each of the $3N$ elementary moves. The CPU time needed for this part grows as N^2. When N is small (about 100) it is possible to store in memoty the contributions to the two body quantities relative to each pair of particles, reducing of a factor 2 the time for each loop over the pairs, and reducing the number of interpolations of the pseudopotential tables. The time needed with such optimizations for a sweep over all the particles and the shadows in a $N = 108$ box is of the order of 3×10^{-1} seconds on an IBM rs/6000- 580. The code occupies in this way a large amount of memory, (about 4Mbyte) that increases again with N^2. For $N = 1800$ (that is the typical number of real particles in the case of the interface) we would get a RAM occupation of about 1Gbyte and a CPU time per sweep of 83 seconds.

A very useful technique, that permits to reduce the CPU time needed in simulations of

large systems, is that of the linked–lists (LL). It consists in dividing the simulation box in subcells whose side is larger than r_{corr}^{max} where r_{corr}^{max} is the largest range of the correlations (or potentials) present in the problem. In ^{4}He only nearly short–ranged correlations are used. Simulations with $N = 108$ atoms give already satisfactory results both in the liquid and in the solid phase. In this case the correlations are truncated in correspondence of on half of the side of simulation box. When dealing with larger boxes, the accuracy in the calculations of pair terms is increased, but the results do not change significantly any more. It is then worth considering potentials truncated at some distance independent on the sides of the simulation box, limiting in this way the number of nonzero pair contributions involved in the calculations. The number of particles around a given one falling within the range of the potential is nearly a constant number M, that depends *only on the cutoff and not on the size of the simulation box.* For each particle considered, one has to calculate only M pair terms, instead of N, and the growth in CPU time becomes linear in N. The LL represent an efficient way of implementing the use of truncated correlations and potentials.

Let us consider for simplicity a 2D system. We can divide it as in fig. B.1. Before starting the simulations one sets up two arrays, one dimensioned with the number of particles (let us call it LIST) and one dimensioned with the number of cells (let us call it HEAD). In HEAD we want to put a representative of each cell, that is the label of a particle belonging to that cell, while LIST is built up in such a way that its i-th element contains the label j of another particle in the cell, or 0. For instance, if we consider the cell in fig. B.2 that contains the particles 5, 9, 12, 15, the correspondent elements of list will be as follows:

LIST(5)=9

LIST(9)=12

1	2	3	4	5
6	7	8	9	10
11	12	13	14	15
16	17	18	19	20
21	22	23	24	25

Figure B.1: A 2D simulation box divided in neighbours cells.

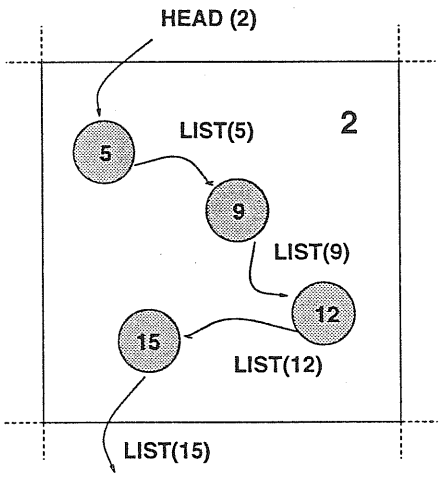

Figure B.2: Close-up of cell 2 in fig. 1

LIST(12)=15

LIST(15)=0

If the cell number is 2, HEAD(2) will contain 5.

If we want to move the particle number 9, we have first to look for the cell to which it belongs, on the basis of its coordinates. After that we start to calculate pair quantities with the particles present in that cell. We look for HEAD(2), and find 5. We calculate everything for pair 9–5. Then we look for LIST(5), that is 9 so we skip the pair. LIST(9) contains 12, and we calculate the pair 9–12 and so on. When we come to LIST(15) we find 0, and this signals that no more particles are present in the cell. After that we start to consider the nearest cells (1,6,7,8,3,21,22 in this case), looking for the representative of each and looping on the other particles present. No more particles are needed, because the nonzero contributions can come only from within these cells. A disadvantage of this method is that the overhead due to managing and refreshing the tables is quite large, making unuseful the application of LL to small systems. The application of the LL algorithm enables to sweep all the degrees of freedom in a $N = 1800$ box in 16 seconds on IBM rs/6000 -580, without storing the pair contributions, so that the memory requested is less than 2Mbyte. The LL implementation that we did is not completely optimized, and some time shall be gained with refinements of the algorithm, which involve also Verlet tables.

Eventually, LL constitutes a good basis for a possible parallelization of the code. The relative gain in time will probably allow for the simulation of interfaces of larger section, that are essential in order to study many interesting surface properties.

Acknowledgements

I want to thank first of all my supervisors Stefano Fantoni and Luciano Reatto, for their illuminating toughts and for their patience in driving me through the wonderful lands of many–body physics. Then I want to thank Erio Tosatti and all the Condensed Matter group in SISSA for all the useful discussions, the scientific support and the friendly atmosphere found here in Trieste. A particular mention is owed to Andrea Ferrante, that helped me in the developemet of this work.

I must acknowledge the major moral support coming from my wife Maria Teresa and from my wonderful children Chiara, Lucia and Giovanni, that accepted three years of separation, giving me the courage of facing all the troubles I have encountered here. I want finally remember here my mother, that was not given of enough time to joy with me at the end of this task.

Bibliography

[1] For a review on Helium see for instance W.E. Keller *Helium-3 and Helium-4*, Plenum Press, NY, 1969; D. Pines, P. Nozières, *The Theory of Quantum Liquids - II Superfluid Bose Liquids*, Addison–Wesley (1990).

[2] E. Feenberg, *Theory of Quantum Fluids*, Academic Press, NY (1969).

[3] R.A.Aziz, V.P.S. Nain, J.S. Carley, G.T. McConville: *J. Chem. Phys.* **70**, 4330 (1979).

[4] M. H. Kalos, M. A. Lee, P. A. Withlock, G. V. Chester: *Phys. Rev. B* **24**, 115 (1981).

[5] F. Gallet, S. Balibar and E. Rolley, *J. Physique* **48**, 369 (1987).

[6] O. A. Andreeva, K. O. Keshishev, A. B. Kogan and A. N. Marchenkov: *Europhys. Lett.* **19**, 683 (1992).

[7] S. Balibar, C. Guthmann and E. Rolley, *J. Physique* , (1993).

[8] E. Rolley, E. Chevalier, C. Guthmann and S. Balibar: *Phys. Rev. Lett.* **72**, 872 (1994).

[9] C. Ebner, D. O Edwards, *Phys. Rep.* **2C**, 77 (1970).

[10] H. J. Lauter, H. Goodfrin, V. L. P. Frank and P. Leiderer, *Phys. Rev. Lett.* **68**, 2484 (1992).

[11] M.T. Chen, J.M. Roester, J. M. Model, *J. Low Temp. Phys* **89**, 125 (1992).

[12] F. Mugele, u. Albrecht, P. Leiderer, *J. Low Temp. Phys* **96**, 177 (1994).

[13] H. J. Lauter, H. Goodfrin, V. L. P. Frank and P. Leiderer in *Excitations in 2D and 3D Quantum Fluids*, edited by A. F. G. Wyatt and H. S. Lauter (Plenum, NY, 1991).

[14] J. L. Epstein, E. Krotschek, *Phys. Rev. B* **37**, 1666 (1988) E. Krotschek, C. J. Tymczk, *Phys. Rev. B* **45**, 217 (1992).

[15] B. E. Clements, H. Forbert, E. Krotschek, M. Saarela, *J. Low Temp. Phys* **95**, 849 (1994).

[16] V. R. Pandharipande, S. C. Pieper and R. B. Wiringa, *Phys. Rev. B* **34**, 4571 (1986).

[17] A. Belic, F. Dalfovo, S. Fantoni and S. Stringari, *Phys. Rev. Lett.* , in press .

[18] J. L. Vallés and K. E. Schmidt, *Phys. Rev. B* **38**, 2879 (1988).

[19] K. A. Gernoth and M. L. Ristig, *Phys. Rev. B* **36**, 8369 (1987).

[20] K. A. Gernoth and J. W. Clark, *J. Low Temp. Phys* **96**, 153 (1994).

[21] For a review on main variants of Monte Carlo calculations see e.g. K. E. Schmidt, D. M. Ceperley, *Monte Carlo Techniques for Quantum Fluids, Solids and Droplets* in *The Monte Carlo Method in Condensed Matter Physics*, vol. 71 of *Topics in Applied Physics*, edited by K. Binder (Springer, Berlin, NY 1992), chap. 7.

[22] S. A. Chin and E. Krotscheck, *Phys. Rev. Lett.* **65**, 2658 (1990).

[23] A. Wagner, D. M. Ceperley, *J. Low Temp. Phys* **94**, 185 (1994).

[24] S. A. Vitiello, K. Runge, M. H. Kalos, *Phys. Rev. Lett.* **60**, 1970 (1988); S. A. Vitiello, K. J. Runge, G. V. Chester, M. H. Kalos, *Phys. Rev. B* **42**, 228 (1990).

[25] L. Reatto, G. L. Masserini, *Phys. Rev. B*
ve38, 4516 (1988).

[26] A. Ferrante, M. Bernasconi, X.Q.G. Wang, S. Fantoni and E. Tosatti:*HNC Theory for Shadow Wave Functions* in *Recent Progress in Many–Body Theories*, edited by C. E. Campbell and E. Krotscheck (Plenum, NY 1992).

[27] F. Pederiva, A. Ferrante, S. Fantoni, L. Reatto, *Physica* **B194–196**, 967 (1994).

[28] F. Pederiva, A. Ferrante, S. Fantoni, L. Reatto, *Phys. Rev. Lett.* **72**, 2589 (1994).

[29] F. Pederiva, A. Ferrante, S. Fantoni and L. Reatto, to be published .

[30] J. N. Cape, L. V. Woodcock, *J. Chem. Phys.* **73**, 2420 (1980) and references therein.

[31] R. J. Galejs, H. J. Ravech, G. Lie, *Phys. Rev. A* **39**, 2574 (1989).

[32] K. A. Gernoth, F. Pederiva, S. A. Vitiello, S. Fantoni and L. Reatto, to be published.

[33] L. Reatto, G. V. Chester, *Phys. Lett.* **22**, 276 (1966).

[34] L, H. Nosanow, *Phys. Rev. Lett.* **13**, 270 (1964).

[35] R. Jastrow, *Phys. Rev.* **98**, 1479 (1955).

[36] W. L. McMillan, *Phys. Rev.* **138A**, 442 (1965).

[37] C. C. Chang and C. E. Campbell, *Phys. Rev. B* **15**, 4238 (1977).

[38] K. Schmidt, M. H. Kalos, M. A. Lee, G. V. Chester, *Phys. Rev. Lett.* **45**, 573 (1980); **47**, 807 (1981).

[39] V.R. Pandharipande, *Phys. Rev. B* **18**, 218 (1978).

[40] Q. N. Usmani, S. Fantoni, V. R. Pandharipande, *Phys. Rev. B* **26**, 6123 (1982).

[41] R. P. Feynman, M. Cohen, *Phys. Rev.* **102** , 1189 (1956).

[42] K. E. Schmidt, M. A. Lee, M. H. Kalos, G. V. Chester, *Phys. Rev. Lett.* **47**, 807 (1981).

[43] L. Oddi, L. Reatto, *Nuovo Cimento D*, **11**, 1679 (1989).

[44] E. Manousakis, S. Fantoni, V. R. Pandharipande and Q. N. Usmani, *Phys. Rev. B* **28**, 3770 (1983).

[45] M. Viviani, A. Buendia, S. Fantoni and S. Rosati, *Phys. Rev. B* **38**, 4523 (1988).

[46] S. A. Vitiello, K. E. Schmidt, *Phys. Rev. B* **46**, 5442 (1992).

[47] S. Moroni, S. Fantoni and G. Senatore, to be published.

[48] W.G. Hoover, S. G. Gray, K. W. Johnson, *J. Chem. Phys.* **55**, 1128 (1971).

[49] J.P. Hansen, L. Verlet, *Phys. Rev.* **184**,151 (1969).

[50] B. J. Alder, T. E. Wainwright, *J. Chem. Phys.* **33**,1439 (1960).

[51] W. Wu , S. A. Vitiello, L. Reatto, M. H. Kalos, *Phys. Rev. Lett.* **67**, 1446 (1991).

[52] S. A. Vitiello, L. Reatto, G. V. Chester and M. H. Kalos, to be published.

[53] L. Reatto: *On shadow wave functions for Condensed phases of Helium* in *Recent Progress in Many-Body Theories*, edited by C. E. Campbell and E. Krotscheck (Plenum, NY 1992).

[54] T. MacFarland, S. A. Vitiello, L.Reatto, *J. Low Temp. Phys* **89**,433 (1992).

[55] L. Reatto and G. L. Masserini: private communication.

[56] T. MacFarland, S. A. Vitiello, L.Reatto, to be published.

[57] P. R. Roach, J. B. Ketterson, C. W. Woo, *Phys. Rev. A* **2**, 543 (1970) .

[58] D. M. Ceperley and E. L. Pollock, *Phys. Rev. Lett.* **65**, 2658 (1990).

[59] R, M. Panoff and P. A. Whitlock, *Momentum Distributions in Quantum Liquids from Green's Function Monte Carlo Calculations*, Proceedings of th Workshop on Momentum Distributions, Argonne, IL, 1988, Plenum Publishing Co.

[60] M. J. Mandell, J. P. McTague, A. Rahman, *J. Chem. Phys.* **64**, 3699 (1976).

[61] J. D. Honeycutt, H. C. Andersen, *Chem. Phys. Lett* **108**, 535 (1984); *J. Chem. Phys.* **90**, 1585 (1986), and references therein .

[62] K. Huang, *Statistical Mechanics*, J. Wiley & Sons, NY, 1963.

[63] M.P. Allen, D. J. Tildesley : *Computer Simulations of Liquids* (Oxford University press, Oxford 1987).

[64] S. Wansleben, D. P. Landau, *Phys. Rev. B* **43**, 6006 (1991).

[65] A. F. Andreev, in *Excitations in 2D and 3D Quantum Fluids*, edited by A. F. G. Wyatt and H. S. Lauter (Plenum, NY, 1991).

[66] K. O. Keshishev, A. Ya. Parshin, A. V. Babkin, *JETP Lett.* **49**, 56 (1979).

[67] P. Nozières and F. Gallet, *J. Physique* **48**, 353 (1987).

[68] A. Bonissent, B. Mutaftschiev in *Chemistry and Physics of Solid Surfaces*, edited by R. Vanselow and W. England (CRC, Boca Raton, FL 1982), vol. 3, p. 163.

[69] Y. Carmi, E. Polturak, S. G. Lipson, *Phys. Rev. Lett.* **62**, 1364 (1989).

[70] D. O. Edwards, M. S. Pettersen, H. Baddar, in *Excitations in 2D and 3D Quantum Fluids*, edited by A. F. G. Wyatt and H. S. Lauter (Plenum, NY, 1991).

[71] E. Krotschek, R. A. Smith, J. W. Clark and R. M. Panoff, *Phys. Rev. B* **24**, 6383 (1981).

[72] R. M. Panoff, J. Carlson, *Phys. Rev. Lett.* **62**, 1130 (1989).

[73] D. M. Ceperley, B. J. Alder, *Phys. Rev. Lett.* **45**, 566 (1980).

[74] D. M. Ceperley, G. V. Chester and M. H. Kalos: *Phys. Rev. B* **16**, 3081 (1977).

[75] H. R. Glyde, E. C. Svensson, *Meth. Exp. Phys.* **11**, 303 (1987).

[76] A. Rahman, G. Jacucci, *Nuovo Cimento* **4D**, 75 (1984).

[77] J. P. Hansen and D. Levesque, *Phys. Rev.* **165**, 293 (1968) .